CONVERGENCE OF HALO FINDERS ON SUBHALO PROPERTIES IN AQUARIUS SIMULATION

Ranganath Magadi

Supervised by Prof. Frazer Pearce

Thesis submitted to the University of Nottingham
for the degree of Master of Philosophy, September 2018

Contents

List of Figures

List of Tables

Abstract

Accuracy of halo-finding is increasingly important as many astrophysical applications are dependent on halofinders to identify structures and substructures. In this project I investigate the accuracy of halo finders in recovering subhalo properties such as mass, size, and other sources (methods) such as unbinding. The data for this project is sourced from a common post-processing analysis (common-analysis) project which sourced its data from a Milky Way sized halo in Aquarius simulation. I begin the project by showing the average mass scatter of 20% to exist in individual finder's own analysis (own-analysis) against the 10% scatter in the common-analysis. I then looked into sample subhaloes from the own-analysis and matched them with the common-analysis, in order demonstrate the mass scatter. I found missing substructures, center offsets and simulation artifacts which illustrated the possible cases for mass scatter. With VOBOZ finder, I showed that the mass scatter was due to different virial mass definitions. Similarly, with ADAPTAHOP and ROCKSTAR finders, I showed that the choice of including or excluding substructures lead to 10% scatter in the mass. Secondly, I compare the sizes of subhaloes across the finders. I demonstrated that multiple size definitions in AHF finder leads to two sets of sizes and therefore leads to scatter in the size. This would mean that, for all the finders with the exception of ROCKSTAR, sizes of subhaloes were not reliable as they were not derived from the mass. With ROCKSTAR, I demonstrated that the density remained same for all the subhaloes suggesting that size can be derived from mass. Users have to be cautious while reading sizes from halo catalogues, and should not be trusted to be derived from the mass. I would recommend the users to generate the sizes themselves from the mass. Finally, I explore the spurious (unbound) fractions across the finders. With HBT finder, I illustrated that the spurious (unbound) subhaloes were distributed on the outskirts, that peaked beyond 200kpc from the halo center. With the cumulative mass functions for the configuration space finders H3D, AHF and SUBFIND, I showed that the former finders performed better unbinding than the latter finders. While H3D showed 50% of its haloes as spurious, AHF showed 80% and SUBFIND recorded 90% of its subhaloes as spurious. All these above mentioned configuration-space finders showed unbound fraction above 50% suggesting that an unbinding procedure is essential for configuration-space finders.

With ROCKSTAR, a phase-space finder, I showed that only 5% of its subhaloes were spurious at a resolution of 20 particles indicating that the phase-space finders may be a preferred to configuration space finders. As configuration-space finders lack velocity information, they have high fraction of spurious subhaloes, and hence running unbinding procedures is strongly recommended unless the application (such as Tidal relics, Streams, X-ray properties) wants to include the spurious particles. Finders such as ADAPTOHOP, H3D and H6D do not have a built in unbinding routine and therefore applications using them have to be cautious. In summary, I demonstrated that the choice of unbinding and the choice of halo finder does affect the final mass and size. The results from this study hopes to provide the users a degree of caution and guide them in choosing the right halo finder that suits their application.

Acknowledgements

I would like to convey my sincere thanks all the people who helped or supported me during the course of my study at the University of Nottingham. Special thanks to my supervisor Prof. Frazer Pearce for his valuable time, comments and guidance. I would also like to thank the head of the school Prof. Michael Merrifield and the University of Nottingham for providing excellent facilities and generous support.

Published Work

This thesis is a piece of original research performed by myself, unless otherwise stated, with sections soon to be published.

Magadi et al (in preparation)...

Chapter 1

Introduction

Observational astronomy makes use of telescopes to observe the farthest regions of the universe. On the other hand, theoretical astronomy explores the universe by building analytical and computer models. The analytical methods have limitations in solving equations. In a simple case of three body problem, as the number of equations increase, the complexity of the problem increases and the solution becomes nearly impossible to solve analytically. Thanks to the rapid development of computers, these analytical problems can be solved numerically. This has spawned a new sub-branch of astronomy, called computational cosmology where the universe is modeled or simulated using super-computers. These models are able to recreate the structures that are seen in the sky to an unprecedented accuracy.

The last 40 years have been a golden age for computational cosmology. Simulations started with simple n-body dark matter only simulations(Frenk and White, 2012). With increasing processing power and resolution, the recent simulations have incorporated complex baryonic physics (Duffy et al., 2010; Schaye et al., 2014; Schaller et al., 2015; Furlong et al., 2015; Chan et al., 2015). This is achieved by incorporating hydrodynamics and semi-analytics into the n-body simulations reproducing the directly observable universe (Springel et al., 2005; Springel, 2010). The process of running a cosmological simulation can be divided into three steps. Firstly, the seed perturbations referred as the initial-conditions(ICs) are generated (Frenk, 1999; Scannapieco, 2012; Reed et al., 2013; LH́uillier et al., 2014). The ICs that represent the initial power or perturbations form the input to a cosmological simulation, which models the universe as a 3D box with particles evenly distributed at the beginning. The initial-conditions are applied and the positions of particles are allowed to evolve under the influence of gravity, to the present day. These simulation codes model the cosmic structure formation as seen in the universe today (Frenk and White, 2012). Further to running a simulation, a "structure finder" is run to identify over-dense collapsed objects called haloes. The output of such a tool would result in producing a catalog of haloes.

The following step is to build an analysis tool to analyse the haloes and measure their distribution. Halo finders identify structures and substructures in the simulation data by locating overdensities that are gravitationally bound. Such a system is called a dark matter halo (Jenkins et al., 2001; Reed et al., 2007). The properties of these objects identified are then converted to other forms such as dark matter density profiles (Reed et al., 2005; Klypin et al., 2014), halo concentration-mass, mass accretion histories etc. The properties derived from these relations are used by several other astrophysical applications like semi-analytic models (Croton, 2006; Somerville et al., 2008; Monaco et al., 2007; Henriques et al., 2009; Benson, 2012), galaxy formation(Scannapieco and Athanassoula, 2012; Cole et al., 2000; Benson et al., 2002; Croton, 2006; De Lucia et al., 2006; Bower et al., 2006; Bertone et al., 2007; Font et al., 2008), large-scale structure(Courtin et al., 2011), near-field cosmology(Libeskind et al., 2012), streams(Sharma and Steinmetz, 2006; Elahi et al., 2011), strong gravitational lensing (Falck et al., 2012; Bhattacharya et al., 2011)), weak gravitational lensing (Kaiser and Squires, 1993; Schneider, 2006), dark matter detection and modified gravity simulations. With object finding becoming an important discipline in the past decade, many halo finders have been coded with variations in their methods and techniques. As different applications use different halo finders, the choice of halo finder influences the application in hand. The big question is - Does all these halo finders provide the same physical information about the structures? This question has spawned a series of structure finder comparison projects 'Haloes gone MAD', 'Subhaloes going Notts' (Knebe et al., 2011, 2013; Onions et al., 2012; Behroozi et al., 2015; Onions et al., 2013; Knebe et al., 2013). This comparison project brought in several halo finders into a common analysis pipeline, a common set of procedures to perform halo centring, and generate halo catalogues. Onions et al. (2012) showed that the scatter in the mass of haloes can be

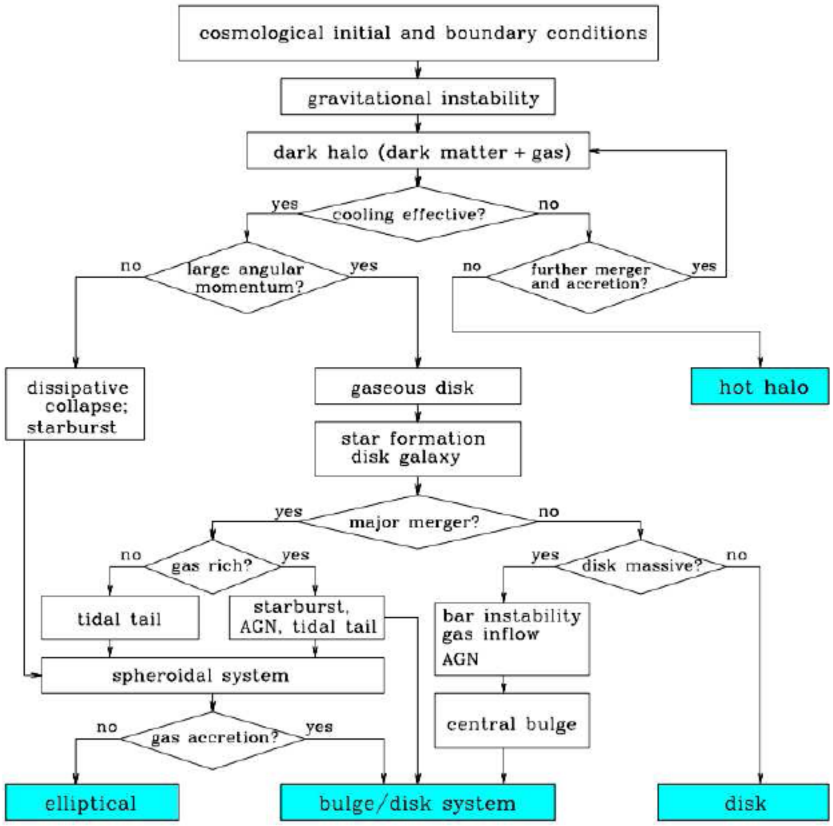

Figure 1.1: Flowchart from Mo et al. (2010) describing galaxy formation.

minimized to 10%. This work extends the comparison project of Onions et al. (2012) by comparing common-analysis (Onions et al., 2012) to each halofinder's individual analysis and highlights the differences in properties such as mass, radius and other methods like unbinding.

The rest of this chapter organized as follows. Structure formation requires understanding of the dark matter, baryons (Chan et al., 2015), evolution of dark matter and baryons, and the various astrophysical processes involved. Section 1.1 summarizes the theory of structure formation in the universe with cold dark matter and a cosmological constant, section 1.2 describes modeling of the structures using simulations, section 1.3 provides an introduction to the Aquarius project and section 1.4 provides introduction to common-analysis and section 1.5 describes the various astrophysical applications.

1.1 Structure formation

Structure formation is an exciting area with complex physical processes involved (Coles, 2000; Baugh, 2006; Mo et al., 2010). Figure 1.1 provides a flowchart that describes the present model of the formation of structures (dark matter and gas). The initial conditions set the ground for dark matter structures to form halos that trap gas at their centres. The gas cools by radiative processes and forms galaxies and stars. The stars and galaxies merge into others, accrete gas and and release energy through feedback mechanisms such as supernovae and AGN (active galactic nuclei). These processes later determine the properties of galaxies. Our universe is thought to be homogeneous (same everywhere) and isotropic (same in all directions) on large scales. Edwin Hubble (1929) made the remarkable breakthrough in proving the expansion of the Universe which recently proved to be an accelerated expansion (Riess, 1998; Schmidt, 1999; Perlmutter et al., 1999).

The matter content of the universe can be broadly classified as dark matter and baryonic matter. The baryonic matter can be further divided into luminous matter and non-luminous matter. Fritz Zwicky (1933) observed the Coma cluster and suggested that a large fraction of mass that exists but unaccounted. This discovery was corroborated with the flat rotation curves of galaxies (Rubin and Ford, 1970; Ostriker et al., 1974). Dark matter does not absorb light, does not interact with light, does not shine and cannot be seen. Experiments are being conducted to detect dark matter both directly and indirectly. WIMPS (Weakly Interacting Massive Particles), MACHOS (Massive Compact Halo Objects) or Axions are thought to be possible candidates for dark matter particles, with WIMPS being the most likely candidate. Dark matter particles are yet to be detected.

Dark matter particles are defined as hot, cold or warm depending on their velocities relative to the speed of light. It was initially thought to consist of hot particles such as neutrinos, traveling at ultra-relativistic velocities. The hot dark matter leads to 'top down' formation of structures, clusters first and galaxies later. This is due to the ultra relativistic particles smoothing out the fluctuations. This does not explain the quasars which were formed at very early times ($z = 7$) and does not agree with observations (Frenk et al., 1983). This led to the idea of cold dark matter as particles travelling much slower than the speed of light, which implies a bottom-up theory of structure formation, according to which galaxies form first and clusters later (Davis and Djorgovski, 1985; Springel et al., 2005). The early universe is radiation dominated and the interaction rate of particles is higher than the expansion rate of the Universe and therefore the particles are in thermal equilibrium until z ¡ 1100, when the radiation domination era ends and matter domination era starts. As a result of the expansion of the Universe, particles fall out of thermal equilibrium. The photons decouple from the hot Big-Bang soup, and protons combine with electrons to form neutral hydrogen atoms, which is referred to as 'recombination'. This leftover background thermal radiation (black body radiation) peaks in the microwave region as the cosmic background radiation (CMB). The discovery of the CMB (Penzias and Wilson, 1965) provided clear evidence for the Big-Bang theory. The CMB is observed to have temperature fluctuations of the order of 10^{-5} which is a highly smooth universe. The temperature fluctuations observed in the CMB are the quantum fluctuations seeding the galaxies that form later. Even though the Universe is expanding, quantum fluctuations lead to over-densities which collapses to form web structure (Shen et al., 2006). Sheets are formed by the collapse along one axis, filaments along two axes and halos along three axes. Small structures form first and large structures form later. The gas trapped in the halo of dark matter forms stars (White and Rees, 1978). The stars congregate to form galaxies and galaxies congregate to form galaxy clusters. The best model which fits very well with the observation is CDM (cold dark matter).

1.2 Modeling Structure formation

Cosmological simulations are essential to build computer models for structure formation. Cosmological simulations started as early as 1970 with the very first simulations run for nonlinear structure formation. After the standard model of cosmology was established, the first CDM (Cold Dark Matter) simulations were run in the 1980s. N-body codes are used to implement dark matter simulations. Modeling dark matter is simpler than modeling baryonic matter as dark matter is collision-less and the only force acting is gravity. A historical listing of milestone achievements in the context dark matter simulations is presented in Frenk and White (2012). An n-body simulation considers a standard cosmological model, the ΛCDM model, flat universe with cold dark matter, dominated by dark energy, $\Omega = 1$, $\Omega_m = 0.27$, $\Omega_\Lambda = 0.73$. The initial conditions for these simulations are generated using the power spectrum of CMB (cosmic microwave background) radiation from surveys such as PLANCK. A uniform particle distribution such as a grid is perturbed with this power spectrum using the Zel'dovich approximation. As cold dark matter dominates, structures form due to gravity. Structures grow bottom up with small structures forming first which aggregate to form bigger structures later. The Millennium simulation, an n-body simulation run using Gadget (Springel, 2012) was implemented by the Virgo Consortium in 2005. It has 10 billion particles and a box size of 500Mpc/h (a billion light-years) on a side.

N-body simulations are extended to incorporate gas particles which eventually forms stars and galaxies. As gas can be treated as a fluid, one can use fluid equations on the gas particles and evolve them. This is referred to as hydrodynamical simulation or simply hydro simulation (Tormen, 1996). Illustris simulation Vogelsberger et al. (2014), a hydrodynamical simulation was run with a box size of 106Mpc and 12 billion particles, from a very high redshift equivalent to 12 million years from Big Bang. The EAGLE (Evolution and Assembly of Galaxies and their environments) a hydrodynamical simulation executed at Durham University with a box size of 100Mpc and 7 billion particles (Springel et al., 2001a). It implemented many astrophysical processes including metal-dependent cooling, star formation, metal enrichment from supernovae explosions and stars, accretion, supernova feedback, black holes, AGN feedback (Schaye et al., 2014; Furlong et al., 2014). Figure 1.2 shows a visualization of the EAGLE simulation.

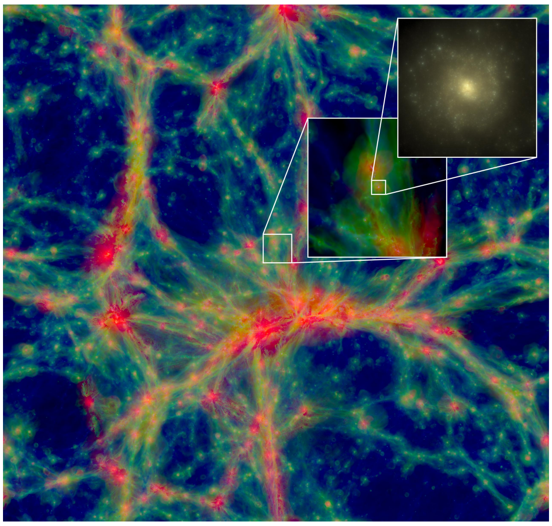

Figure 1.2: EAGLE simulation, an N-body code simulated with 7 billion particles using the initial conditions from the CMB (Cosmic Microwave Background) observations surveyed by the Planck satellite. Credit - EAGLE-Project (2015)

The further subsection 1.2.1 on n-body implementation.

1.2.1 N-body simulation : Implementation methods

The theory on the n-body implementation is as follows. Readers who do not wish to go into the details of n body implementation may skip to the further sections. The gravitational potential due to dark matter is given by

$$\nabla^2 \phi = 4\pi G \rho \tag{1.1}$$

where ∇^2 is the Laplace operator, ϕ is the gravitational potential and ρ is the density of the gravitating object. The gradient of the potential gives acceleration and gravitational force on the particle. Force on the particle can be calculated using any of the following methods.

(a) Particle-Particle(PP) method

The simplest method to find the force on a particle is using the Particle-Particle(PP) method (Aarseth, 1963). The gravitational force over a particle will be the vector sum of all the forces due to all other particles.

$$F = \frac{GMm}{(r^2 + \epsilon^2)^{(\frac{3}{2})}} r \tag{1.2}$$

F is the gravitational force between masses m and M, r is the distance between particles. As $r \to 0$, numerically force $F \to \infty$. To avoid this problem, gravitational softening ϵ is introduced. As the number of particles increases, the processing time scales as N^2, thereby making it slow.

(b) Tree method

A more efficient method to solve the N-body problem is by using a tree algorithm. The time complexity can be reduced to O(Nlog(N)) operations. The initial box is recursively subdivided into eight sub nodes of length equal to half of the parent node until a node has a single particle or is empty. Forces are then calculated by just 'walking' the tree which takes O(Nlog(N)) time. The force calculation starts from the root node and checks if the force calculation is accurate enough by looking at number of particles in the sub-box. If there is a single particle in the relevant box, the walk along the tree is terminated. If there is more than one particle, the force calculation proceeds to further sub-levels. Even though the force calculation is an approximation, the gain in efficiency outperforms the approximation.

(c) PM (Particle-Mesh) method

The Particle-mesh (Efstathiou and Eastwood, 1981; Klypin and Shandarin, 1983) method uses a mesh to smooth out the particle masses on to a grid. The PM(Particle-Mesh) algorithm computes the force using quantities on the mesh derived from the particle positions. The field quantity is converted into Fourier space and potential is calculated using Green's method and the Poisson equation. Potentials are then used to calculate forces between individual particles using interpolation techniques. The potential for this grid is calculated as in Equation 1.1 using a Fast Fourier Transform (FFT) which is faster than direct summation as its time complexity is O(NlogN). This method has a limitation that the number of particles cannot exceed the number of mesh cells N and hence the resolution is limited. On large scales, the Particle-Mesh (PM) method is much quicker than the Particle-Particle (PP) method. However on small scales, PM is not efficient due to the low resolution of the grid. A more efficient method called the Barnes Hut uses a tree instead of a FFT (Barnes and Hut, 1986; Porter and Jernigan, 1986; Jernigan and Porter, 1989). The time complexity of the method scales as O(nlog(n)). At small scales, it is more precise than PM. At large scales, most n-body codes use PM for efficiency and at small scales use PP or trees for accuracy.

(d) Hybrid or Tree-PM (Particle-Mesh) method

A combination of Tree and PM methods such as Tree-PM are referred as hybrid methods (Xu, 1995; Bode et al., 2000; Bagla, 2002; Bagla and Ray, 2003). The hybrid methods have better performance compared to the tree methods. It is important to note that a tree algorithm uses approximation and at long ranges the tree is avoided and hence the force calculation is more precise. A TreePM has further benefits including unlimited dynamical range, less sensitive to clustering, a good handle on softening length for the force. The code used for this thesis work is Gadget (Springel et al., 2005) which is a Tree-PM code. More details on other N-body codes and algorithms are discussed in Hockney and Eastwood (1981); Dehnen and Read (2011). On small ranges, TreePM uses direct summation to calculate the forces. Further improved versions of the P3M are the spatially adaptive mesh refinements (Couchman, 1991).

1.2.2 Analysis pipeline

After N-body simulations are run, a structure finder (halo-finder) is run to identify dark matter haloes. Once the dark matter haloes are found, they are analyzed further and also form the input for merger trees and semi-analytic model.

The general steps in the analysis pipeline are as follows.

1. Initial conditions are generated which forms the input for the simulation.

2. The simulation is run and snapshots are saved for different time steps. Each snapshot has data for each particle such as positions and velocities. This can

be used for analysing other parameters or quantities such as power spectrum etc.

3. The snapshots form the input to a halo finder which identifies overdensities and generates halo catalogues. These are elaborated in chapter 2. Halo catalogue is a collection of basic and derived attributes. Basic attributes are location, velocity, mass, radius and the derived attributes are spin, shape etc.

4. The halo catalogues form the input for the construction of a merger tree. Using the snapshots, the history of every halo is tracked, and the progenitors can be found.

5. Merger tree and halo catalogues form the input for models (such as semi-analytic model) that would populate galaxies into haloes and follow their evolution.

Figure 1.4 shows the general flowchart of an analysis pipeline. Steps 2 forms the input for this project. The scope of this project is limited to the step 3 (halo finding and analysis). Step 4 (Merger Trees) and step 5 (Models such as semi-analytics) are not used in this project, however, it is important to understand that they are dependent on step 3.

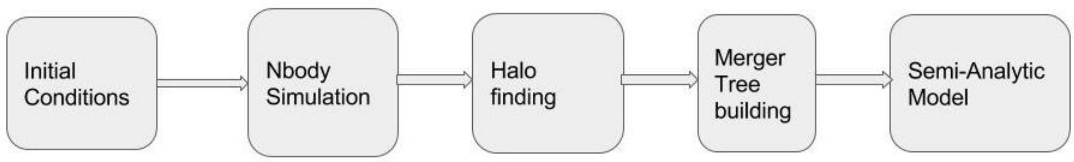

Figure 1.3: Flowchart of dark matter simulation pipeline.

1.3 The Data

The data for this project was generated from the comparison project (Onions et al., 2012). The comparison project used a common-processing pipeline to provide a uniform platform for analysing halo properties of many leading halo finders. The data for the Onions et al. (2012) project comes from the Aquarius simulation (Springel et al., 2008), a simulation of a Milky Way sized halo at five different resolutions, using a parallel Tree-PM code called 'Gadget3'. The Aquarius simulation uses ΛCDM cosmology with box of 100Mpc h^{-1}, with parameters $\Omega = 1$, $\Omega_m = 0.25$, $\Omega_\Lambda = 0.75$, $n_s = 1$, $\sigma_8 = 0.9$,$h = 0.73$ and Hubble constant $H_0 = 100h\mathrm{kms}^{-1}\mathrm{Mpc}^{-1}$. There are 5 levels of resolution, level 5 being the lowest resolution with 2.3 million particles, level 4 has 8 times the number of particles, and so on. Level 1 has the highest resolution with 4.25 billion particles. The data used for this project is generated from the analysis of level 4.

1.4 Common Analysis

Over the last few decades, many halo finding algorithms were run on N-body simulations and a comparison study was performed by Knebe et al. (2011); Knebe et al. (2013). This comparison study was further extended by Onions et al. (2012); Onions et al. (2013) to analyse substructure properties, This comparison study used a common post-processing pipeline (addressed here after as 'common-analysis'), a common method for halo centering, unbinding (removal of unbound subhaloes) and determining the basic attributes for the subhaloes. Initially, each individual halo finder was asked to read the simulation data of a Milky Way sized background halo, identify the sub-structures and return a subhalo catalog. The subhalo catalogs that were received from each finder, was analysed by the common-analysis and subhalo properties such as mass, size, V_{max} (peak velocity of the rotation curve) were measured. According to Onions et al. (2013) report a good agreement with the properties in the inner part of the subhalo, up to the peak of the rotation curve. However, at the outer edges, the scatter increases to 20%. Figure 1.4 shows the schematic architecture of the project with common analysis in perspective. Each halo finder's individual analysis on the same simulation data is referred here after as "own-analysis".

A procedure followed by the common-analysis is described as follows. Subhalo objects are identified by each halo finder and a list of particles belonging to each object are returned from every halo finder to the common-analysis. This forms the input data to the common-analysis. A particle is allowed to belong to a single subhalo and hence any duplicate particles across different subhaloes are removed. The particle lists were sorted in the order of mass and starting from the smallest halo various operations such as centring, trimming and overdensity checks were performed. Following this, the center of each subhalo is identified using the 'centre of mass' of all the particles contained in that subhalo. With this center, the particles are sorted radially and only the innermost 10% particles are considered a new "centre of mass" is computed. This procedure is iterated until a stable centre is found. After identifying the centre, particles are ordered radially from the center. Over-density is calculated repeatedly until the density drops below 200 times the critical density ρ_{crit}. This density marks the radius R_{200c} of the halo. All the particles within this radius are considered belonging to that halo. The mass of the halo is computed as the sum total of all the particle masses. Finally, all the particles not bound to the halo are removed. This procedure is called as unbinding. Unbinding in common analysis is achieved in three different configurations, own-unbinding, common-unbinding and no-unbinding. With own unbinding option, every halo finder implements its own unbinding procedure. With common unbinding option, a common unbinding procedure is implemented in the common-analysis. With no-unbinding option, unbinding is neither implemented at each finder level nor at individual finder level. Finally, the mass of the halo M_{200} is calculated as the total mass of the particles bound to the halo within R_{200}. Similarly, rest of the basic attributes are deduced and the halo catalogues are generated from the common-analysis.

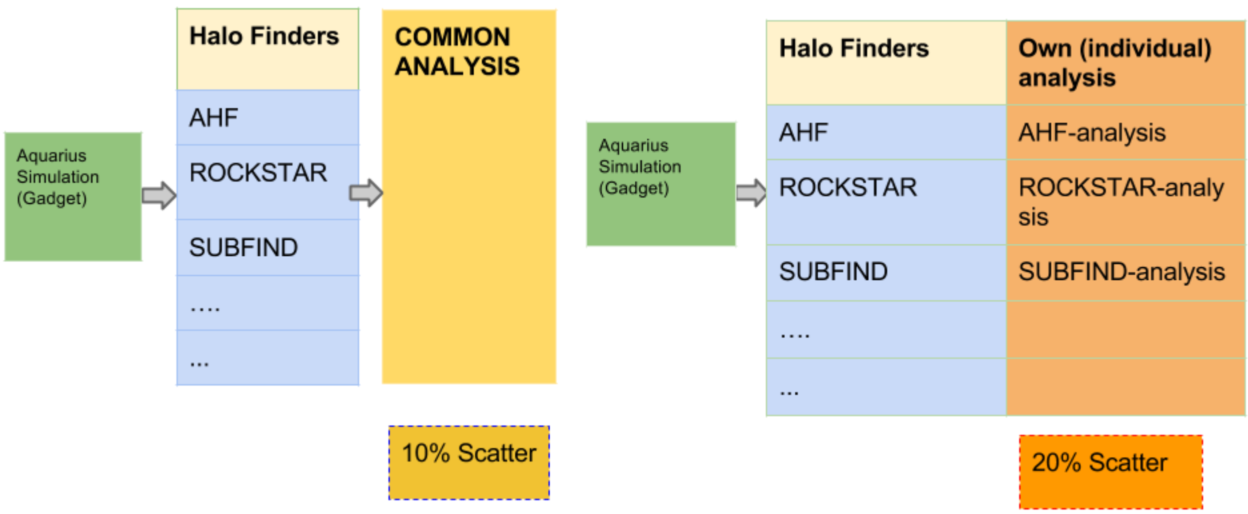

Figure 1.4: Schematic diagram showing analysis pipelines with percentage of scatter in the mass. own-analysis (Individual halofinder's analysis) is at 20% and the common-analysis is at 10%.

1.5 Astrophysical Applications

Many astrophysical applications use substructure finding algorithms, the scatter in the subhalo attributes from these halo-finders introduces uncertainties in the dependent application models. Some of the dependent applications are described as follows.

1.5.1 Semi Analytical Models

Semi-analytics (SAM) is a method of introducing galaxies into N-body simulations. The first model was proposed based on the initial idea of galaxy formation by White and Rees (1978). Further developments were made with more physics incorporated into the model (Cole et al., 2000; Bower et al., 2006; Croton, 2006; De Lucia and Blaizot, 2007; Font et al., 2008; Guo et al., 2011). Using an N-body simulation, a tree is constructed with a merger history of the haloes at $z = 0$. This tree forms the basis for the semi-analytics. The branches of the tree represent progenitors that merge to form the final haloes. The evolution of baryons within the haloes is determined by a set of equations which are connected using free parameters. The free parameters are then fine tuned to fit the model to match properties at various redshifts such as the galaxy luminosity function (Bower et al., 2010). The model generates a galaxy catalogs at various redshifts. Understanding of the parameters requires further investigation into the physical processes. SAM may be accurate and stable if the merger tree is accurate and realistic. This means the input halo catalogues have to be more accurate. There should not be sudden change in mass or size of haloes, or sudden disappearing or appearing of haloes in catalogues across snapshots. This particularly happens if there are any mergers. These anomalies arise due to a halo finder that is not well constrained. The halo centring is another important area of concern to make sure that the centre should not suddenly move across snapshots. Another important area of concern is that the halo finder should have a robust “unbinding” feature. This is because if there are structures which are unbound, however they still contribute to enhancing the background density leading to structures in the catalogue which should otherwise be absent.

1.5.2 Galaxy formation

Galaxy formation models incorporate gas along with dark matter in order to simulate galaxies and stars. This involves the complex physical processes that come into play due to gas interactions. These models use semi-analytics constructed from merger trees. Stable merger trees are built using halo and subhalo catalogues that require a proper choice of a halo finder (Scannapieco and Athanassoula, 2012; Cole et al., 2000; Benson et al., 2002; Croton, 2006; De Lucia et al., 2006; Bower et al., 2006; Bertone et al., 2007; Font et al., 2008). The evolution of gas and stars requires hydrodynamic simulations (Aragón-Calvo et al., 2007; Hahn et al., 2007; Hoffman et al., 2012).

1.5.3 Large-scale structure

The LSS can be used to measure the cosmological parameters (Courtin et al., 2011). The large scale surveys such as DES (Dark Energy Survey) are used to constrain the theoretical halo mass function (Wu et al., 2010). These surveys make use of dark matter simulations and halo finders (Lacey and Cole, 1994; Cole and Lacey, 1996; Tinker et al., 2008; Lukić et al., 2009; More et al., 2011; Watson et al., 2013).

1.5.4 Near-field cosmology

Near-field cosmology (Libeskind et al., 2012) primarily focuses on computational modeling of the Milky Way subhaloes and their dynamics. As subhaloes are identified using halo finders, the scatter in the halo finding affects the subhalo finding.

1.5.5 Streams

Streams (Sharma and Steinmetz, 2006; Elahi et al., 2011) are unbound structures such as debris formed due to the tidal disruptions. Streams can be detected in haloes (Carollo et al., 2007; Helmi, 2008) using halo finders with an efficient unbinding procedure. Halo finders which use velocity information are more efficient to detect streams (Fairbairn and Schwetz, 2009; Kuhlen et al., 2010, 2012). Several techniques are used to detect streams (Sharma and Steinmetz, 2006; Diemand et al., 2008; Zemp et al., 2009; Ascasibar, 2010; Elahi et al., 2011). The currently used technique in simulations to identify streams is the particle tagging method (Warnick et al., 2008; Cooper et al., 2010; Helmi et al., 2011; Rashkov et al., 2012). Once tidal debris are identified, it can be used to study the morphology of satellite galaxies by including them into the semi-analytic models. As semi-analytic models depend on merger trees, the accuracy of halo finding becomes relevant.

1.5.6 Gravitational lensing

Light bends due to gravity as described by the general theory of relativity. This applies to dark matter structures, causing "lensing" effect, the deflection of light due to presence of matter. If the lensing is strong enough to produce multiple images of the source, it is referred as strong lensing (Falck et al., 2012; Bhattacharya et al., 2011). If the lensing produces general distortions measured statistically, it is called weak lensing. In case of strong lensing, lensed images of the source are processed using halo finders to form the dark matter halo mass distribution. The scatter in the halo attributes does affect strong lensing. For example, the halo finders cannot assume spherical symmetry as the haloes are triaxial in shape (Jing and Suto, 2002; Oguri et al., 2005; Gavazzi, 2005; Sereno and Zitrin, 2012; Limousin et al., 2012).

Weak gravitational lensing can be used to test dark matter, dark energy, cosmological model, and history of the growth of structures (Kaiser and Squires, 1993; Wilson et al., 1996; Bartelmann and Schneider, 2001; Schneider, 2006). New research has analysed the statistical distortions of the galaxies from the background sources and evaluated the shear in the matter distribution (Mellier, 1999; Refregier, 2003; Schneider, 2006; Munshi et al., 2008).

1.5.7 Dark matter detection

Dark matter detection methods can be divided into two types. Direct and indirect detection. The indirect detection looks for particles that are generated from the self-annihilation of dark matter particles due to their decay. The direct detection method looks for the dark matter particles that recoil from the nucleus of certain atoms in a detector. In both the methods, the detection is affected by the dark matter substructures. The emission signal from the indirect method is affected by the density of the substructures from a halo. (Stoehr et al., 2003; Diemand et al., 2006; Elahi, 2009; Maciejewski et al., 2011; Blanchet and Lavalle, 2012; Gao et al., 2012).

1.5.8 Modified gravity simulations

MG (Modified gravity) simulations use N-body simulations with a new definition for gravity, a modified version of the GR (General Theory of Relativity). MG is an alternative to dark energy (Schmidt, 2009; Zhao et al., 2011; Li et al., 2012). Just as in CDM simulations, the MG simulations use halo finders which makes use of the high mass end of the halo mass function (LoVerde et al., 2011; Hoyle et al., 2011; Carlesi et al., 2011; Baldi, 2012).

1.6 Summary

In this chapter the reader is introduced to the theory of structure formation followed by computer models to simulate the dark matter. using N-body codes. Following this, an introduction is provided for the Aquarius simulation and the "common-analysis" project. This is followed by describing various astrophysical applications that are dependent on the halo finders. The following chapter would give an introduction to halo finders.

Chapter 2

Halo Finders

2.1 Introduction

A halo finder looks for overdensities, identifying and quantifying structures and sub-structures. Overdensities are identified usually by one of the two common methods, FOF (Friends of Friend) (Davis and Djorgovski, 1985) or SO (Spherical Overdensity) (Press and Schechter, 1974; Lacey and Cole, 1994), or combination of both. FOF is a percolation algorithm, which does not assume any geometry and therefore the structures identified are non-spherical. This is especially advantageous for detecting streams and other non-spherically shaped haloes (Tinker et al., 2008). An FOF algorithm gathers all the neighbouring particles up to predefined length called the linking length (Huchra and Geller, 1982; Press and Davis, 1982; Eke et al., 2004). Linking length is used as a threshold parameter which determines particle's membership of the halo. A linking length of b=0.2 is 0.2 times the mean distance between the particles. The linking length is a dimensionless parameter that defines the group's boundary limit and is not a function of redshift or density (Jenkins et al., 2001). This linking length results in an overdensity of 180 times the box density (More et al., 2011), which contains more particles than a halo that has overdensity of 200 times the critical density of universe, which is typically called the M_{200} mass. According to the spherical top-hat model, the collapse exceeds the expansion of the Universe at an overdensity of 178 times the critical density for an Einstein-de Sitter universe. An overdensity of 200, is well above the overdensity of 178 provided by the spherical top-hat collapse model (Peebles, 1980), and hence the latter extends out further than the former and collects enough particles to be bound to that halo.

Some of the disadvantages of the FOF algorithm (Tinker et al., 2008) include the fact that the centre could be offset and may even lie outside the actual candidate. As FOF algorithm uses linking length, there is a possibility of clubbing neighbouring structures and therefore substructures could be counted as separate structures (demonstrated in the results section 3.6) which may not lead to a one-to-one mapping between the objects seen in the observations to the objects found in the simulations. Another disadvantage is that substructures might be missed out if they are not within the linking length despite the substructure lying within the spherical boundary of the host structure. Figure 2.1 shows an example of an FOF finder where the distance between the two particles is greater than the linking length d and therefore two separate structures are identified. The FOF based finders define the mass of a halo as the cumulative mass of all the linked particles.

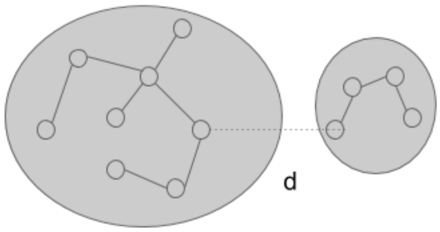

Figure 2.1:
Schematic illustration of an FOF (Friends-Of-Friends) overdensity finder where two haloes are recovered as the distance(d) between the two particles is greater than the linking length.

A spherical overdensity finder on the other hand looks for overdense regions by computing densities in spherical shells with an initial highest density point being the centre and eventually a centre of mass is computed and fine-tuned (Tinker et al., 2008). SO halos are spherical by definition, and hence the mass and edge is determined by the spherical top-hat model. Generally, an SO finder calculates the mass of a halo as follows:

$$\frac{M_{ref}(< R_{ref})}{\frac{4}{3}\pi R_{ref}^3} = \Delta_{ref}\rho_{ref} \tag{2.1}$$

where Δ_{ref} is the virial density contrast. Density contrast is a number which indicates the overdensity. For example, an density contrast of $\Delta_{ref} = 200$ indicates that the overdensity is 200 times that of the ρ_{ref} which can be the critical density ρ_{crit} of the universe or the background density $\rho_{background}$ of the simulation box.

Mass definitions The virial mass of a halo is an important definition to determine the halo mass. Several definitions for the mass were listed in the workshop by Knebe et al. (2015) as below.

- Friends-of-Friends mass - This is the total mass of all the particles gathered using friends-of-friends algorithm.
- Bound mass - This is the friends-of-friends mass with unbinding (unbound particles removed).
- M_{200c} - This is the total mass of all the particles up to a size where the average density of the halo is 200 times the critical density of the universe.
- M_{200b} - This is the total mass of all the particles up to a size where the average density of the halo is 200 times the background, or average density of the Universe.
- BN - This is the the spherical top-hat collapse mass as defined by Bryan and Norman (1998).

The Figure 2.2 shows a schematic example of a halo size due to the different mass definitions ρ_{crit} or $\rho_{background}$. Also seen are the subhaloes, which are haloes found within the radius of a larger halo.

Despite FOF and SO being the most common ways of locating overdensites, there are other methods such as Voronoi tessellation, where each particle is surrounded by a region inside which any point is closer to this particle than to any other particle. For every region, local density can be calculated to form structure. Another method which is useful to identify streams relies on velocity information to identify comoving groups even before the positions are used to segregate.

2.2 Halo Finder Types

A halo finder can be classified based on the internal algorithm it incorporates (as discussed in the previous subsection). A density peak locator such as a Spherical

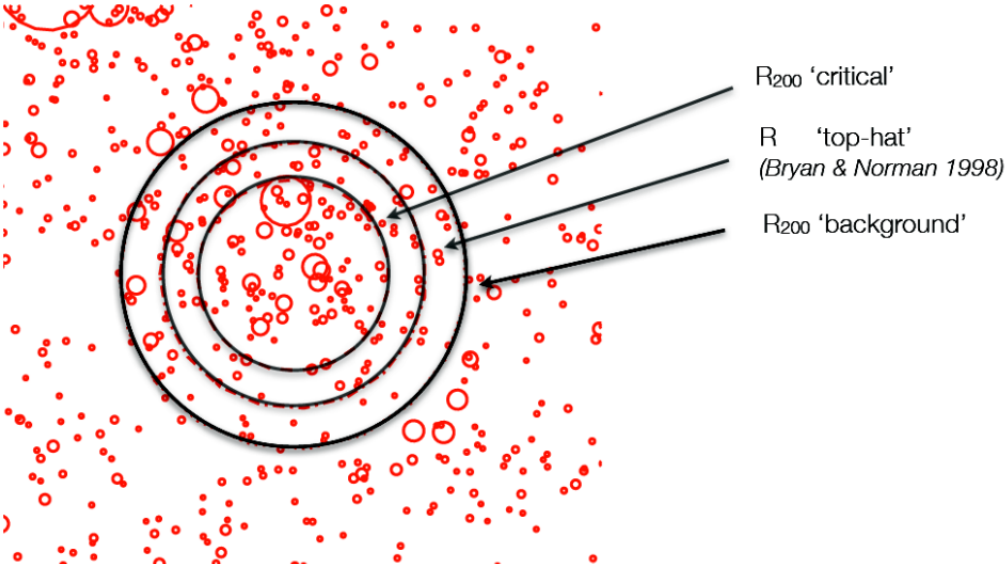

Figure 2.2: Schematic illustration of different halo sizes due to different virial mass definitions.

Overdensity(SO) or a direct particle collector such as an FOF or a combination of both. It can also be classified based on the number of dimensions (3D, 6D or 7D) of information the halo finder uses in order to identify haloes.

2.2.1 Configuration-space finders

Configuration-space finders (real-space finders) (Knollmann and Knebe, 2011; Springel et al., 2001b; Colombi, 2013; Mario Agustín Sgró, 2015) use 3 dimensions (spatial positions x,y,z) to identify structures. Applications involving full mass studies may find the 3-d finders best suited as they look for complete mass. In close encounters (i.e. if two objects are closely passing by), a 3-d finder may detect a single structure instead of two. This is due to the lack of velocity information to distinguish the particle membership, as the objects get closer. A configuration-space finder along with an unbinding procedure works as a pseudo-phase-space finder. E.g. SUBFIND, H3D, ADAPTAHOP, AHF, MENDIETA, VOBOZ.

2.2.2 Phase-space finders

Phase-space finders (Elahi et al., 2011; Behroozi et al., 2012; Maciejewski et al., 2009; Ascasibar and Binney, 2005) use 6 dimensions (3-d positions and 3-d velocities) to identify haloes. The velocity information has the advantage of effectively and accurately identifying unbound objects such as tidal remnants, diffused streams, tidal tails, etc. Finders such as ROCKSTAR, H6D and HSF use full phase-space information for all types of dynamical analyses such as an infall, flyby or merger. STF is best suited for identifying diffused tidal streams as it does not use full phase-space information, and therefore is computationally more advantageous than the other phase-space finders.

2.2.3 Time space halo finders

Usually a halo finder uses single snapshot to identify halo objects in a simulation. However, one might be interested in tracking the halo across multiple snapshots for purposes such as identifying missing objects, short lived objects or to remove spurious structures (Tormen et al., 2004; Giocoli et al., 2008, 2010; Benson, 2012). E.g. ROCKSTAR, HBT (Han et al., 2011; Han et al., 2012), MHT (Gill et al., 2004) or SURV (Tormen et al., 2004; Giocoli et al., 2008, 2010).

2.3 General algorithm to find subhaloes

The general steps followed by all halo finders are as shown in the Figure 2.3. The first step is candidate identification. This is achieved by identifying the peaks in the density fields or troughs in the gravitational potential field. The candidates are identified by using one of the two methods FOF or SO as mentioned in the earlier sections. The following step is to collect the particles belonging to the candidate objects. Finders such as AHF include sub-structures (Knollmann and Knebe, 2011) to host halo, and are referred to as "inclusive". Finders such as SUBFIND exclude, and so are termed as "exclusive"(Springel et al., 2001b). In other words, if a particle belongs to a single halo, it is called 'exclusive', and if a particle belongs to more than one halo, it is termed 'inclusive'. The choice of inclusive or exclusive could lead to a difference in the mass inferred for the host halo. This is because the "inclusive" finder would add all the substructure masses to the host halo, unlike the "exclusive" finder which discounts the mass of substructures. This choice depends on the scientific problem in hand: gravitational lensing simulations do include substructures, whereas semi-analytical models do not. The following step is to identify the halo centre and bulk velocity. Some finders use "centre-of-mass" to identify the centre. Others go by density peaks or the gravitational potential. Bulk velocity is calculated for an object using the velocities of all the particles or a subset of particles, or it could be the velocity of the most bound particle. The final step, although optional, is unbinding. This is a procedure to discard gravitationally unbound particles. One of the ways for checking boundedness is to see if the total energy (kinetic and potential energy) is negative. Another equivalent way of checking the boundedness is to check if velocity satisfies the escape condition $V_{esc} > \sqrt{2\Phi}$ where Φ is the potential. Some finders do not have an unbinding feature. The centre and bulk velocity determination is iteratively carried out with unbinding. After the unbinding, each structure is identified with a set of bound particles. Section 2.5 provides a more detailed explanation of the unbinding procedure. The following step is to determine the edge or size (and therefore the mass) of a subhalo finding method (Macciò et al., 2003; Prada et al., 2006; Cuesta and Prada, 2008; Anderhalden and Diemand, 2011). The edge or the size determination is ambiguous and is open to a wide range of definitions such as the distance to the farthest bound particle, or it can be defined using the spherical top-hat collapse model or it can be the zero velocity radius, or as some define it as the first isodensity contour at a saddle point. There are other definitions as suggested in Knebe et al. (2013) page 7, suggesting not to define an edge, but instead provide every halo with density profile with fitting function and best fit parameters or a bound particle list. Others suggest to define an object over several dynamical times and to include only those particles that stay over multiple snapshots. Having such a wide range of possible definitions leads to a potential area of scatter across halo finders, which is demonstrated in the radius comparison project (see section 3.3) of our analysis. The final structure is called a halo. Some temporal finders have few optional features such as "tracking" of halos, a procedure to track the evolution of halos. This is achieved by tracking the objects across snapshots at different time steps.

- Generally, the size of a halo is initially determined using the virial radius which is determined using virial density threshold (density contrast). Figure 2.4 depicts a common way of identifying the subhaloes with density peaks and saddle points. The density threshold (ρ_{ref}) is used to determine initial halo edge where ρ_{ref} is density

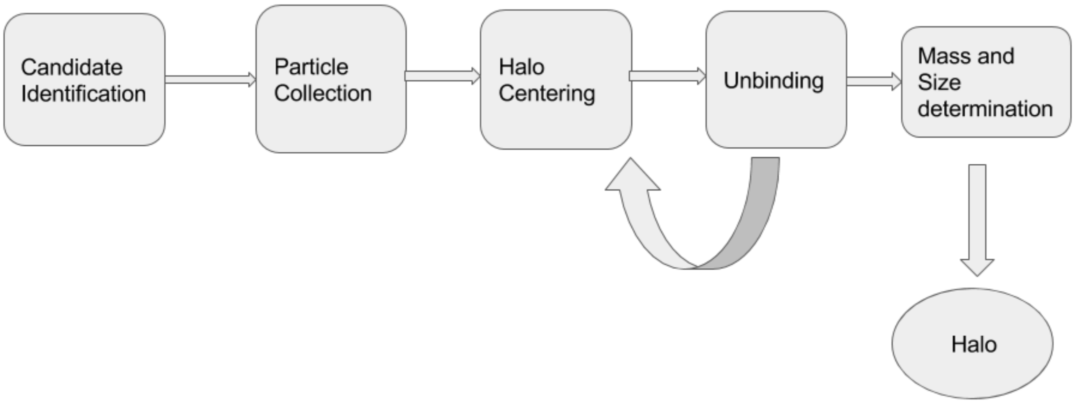

Figure 2.3: A sequence diagram listing the general steps of a halo finder.

with reference to background or critical density. The final subhalo size is refined after further pruning and unbinding which depends on the halo finder. The subhalo edges are most commonly determined using the saddle points which are given by the rise in the density profile above the virial density threshold. If a saddle point is below the density threshold, the density peaks form separate haloes. The final edge is derived by pruning the particle list from the initial edge. Once a halo is identified, all the basic attributes can be measured. The following step is to identify all the substructures. Figure 2.4 shows a schematic diagram with density (background density) plotted against the x position. The saddle points below the virial density threshold segregates a halo from another halo. The saddle points above the virial density threshold segregates a halo from a subhalo. The top diagram shows three peaks with the saddle point to the right of the first peak (from left to right) below the virial density, and therefore the second peak is not a subhalo of the first, but rather a separate second halo. The saddle point to the right of the second peak is above the virial density threshold and hence the third structure is a subhalo of the second or vice versa, but not a separate halo. The bottom diagram shows three peaks with both the saddle points above the virial density threshold resulting in a single halo with two subhaloes. Table 2.1 lists the various halofinders participating in the comparison, and provides a short description for each of them.

Halofinder	Method	Type	Description	Reference
AHF	SO	3D	Uses AMR (Adaptive Mesh Refinement) to identify overdensities.	(Knollmann and Knebe, 2011)
ROCKSTAR	FOF	7D	Uses full phase space and adaptive refinement to identify overdensities.	(Behroozi et al., 2012)
SUBFIND	FOF	3D	Identifies locally overdense, gravitationally bound regions	(Springel et al., 2001b)
MENDIETA	FOF	3D	Identifies haloes with particles more than a threshold number	(Mario Agustín Sgró, 2015)
HSF	FOF	6D	Uses SPH (smoothing kernel) to estimate phase-space density. Also identifies tidal streams.	Maciejewski et al. (2009)
STF	FOF	6D	Uses velocity space to identify tidal streams and subhaloes	(Elahi et al., 2011)
ADAPTAHOP	Octral-tree	3D	Uses a 20 particle SPH kernel to identify local density, No unbinding procedure is used.	(Colombi, 2013)
H3D	FOF	3D	It uses tessellation of 3D space and constructs a binary tree.	(Ascasibar and Binney, 2005)
H6D	FOF	6D	It is an extension of H3D with phase-space and constructs a binary tree.	(Ascasibar and Binney, 2005)
HBT	FOF	4D	Uses time tracing to identify subhaloes and construct merger trees.	(Han et al., 2011).
VOBOZ	SO	3D	Uses watershed algorithm (Voronoi tessellation) to identify and separatesubhaloes from each other.	Neyrinck et al. (2005)

Table 2.1: Participating subhalo finders with the underlying method used, number of dimensions, description and literature reference.

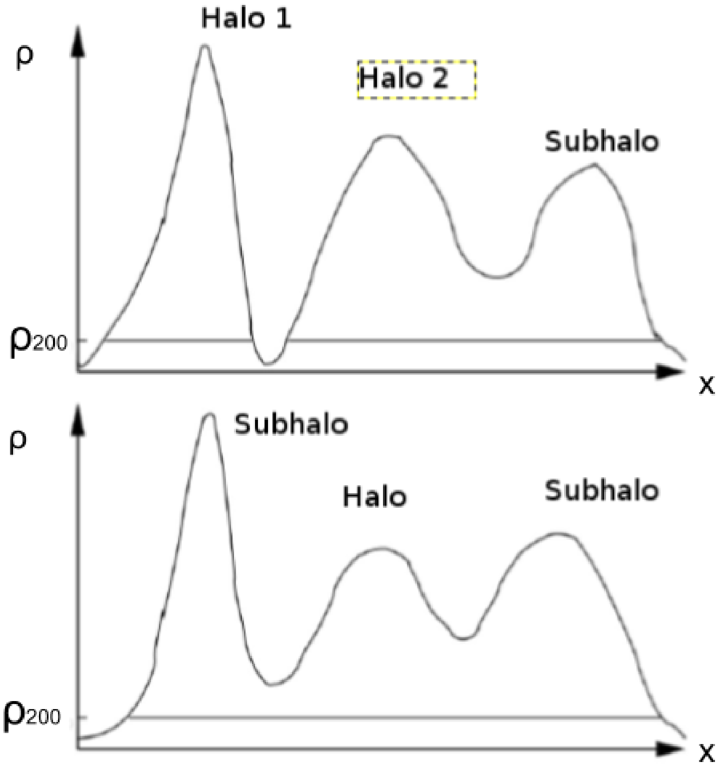

Figure 2.4: One of the common methods of identifying a halo and a subhalo using the virial density threshold and saddle points.

2.4 Halofinders in this comparision project

2.4.1 AHF (Knollmann & Knebe)

AHF (Knollmann and Knebe, 2011) is a 3-d spherical overdensity halo finder (Gill et al., 2004). It uses the AMR (Adaptive Mesh Refinement) grid method to locate density peaks which form the halo and subhalo centres. The grid is used to construct a tree of haloes and subhaloes. To start with, the particles within half the distance between current halo centre and the neighbouring halo centre are considered to belong to the current halo. Gravitationally unbound particles are removed if the particle velocities are more than the escape velocity. Unbinding is iterated with fixed subhalo centre using adaptive mesh refinement hierarchy. Some of AHF's strengths are its ability to execute parallel modules, strategy to handle large simulation data and the scalability for high resolution simulations. AHF uses two definitions (Page 56, Knebe (2015)) for the size of haloes : (1) Virial radius (2) Distance to the farthest bound structure within the tidal radius. The second definition is used for substructures where the first definition does not derive an edge, if the edge density is above the virial density. Figure 2.5 depicts the two different sizes for the two definitions.

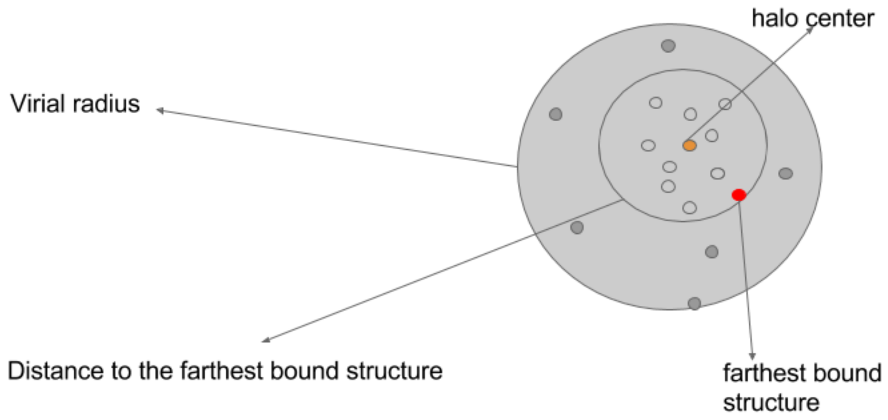

Figure 2.5: AHF uses two definitions for the size. First definition: virial radius, second definition: distance to the farthest bound structure within the tidal radius.

2.4.2 ROCKSTAR (Behroozi)

ROCKSTAR is a grid-independent, shape-independent, highly parallel, adaptive hierarchical refinement method to find haloes and subhaloes. The earlier versions of ROCKSTAR used 6 dimensions, the latest version uses seven dimensions (six dimensions in phase-space and one time dimension) (Behroozi et al., 2012; Behroozi et al., 2013). Initially, the 3-d FOF algorithm finds groups in the simulation volume. Following this, the particle positions and velocities are normalized for each group to derive the phase-space information. The liking length is adaptively chosen to identify subgroups, such that the total particles in the subgroup amounts to 70% of the particles in the group. The positions and velocities in the subgroups are re-normalized and the same procedure is repeated for the subsequent levels of subgroups with a new linking length. The lowest level structures form the haloes and particles are assigned to the closest halo hierarchically in phase-space. Finally, unbound particles are removed using a single pass Barnes-Hut algorithm. However, unbinding is optional and can be switched off for studies such as tidal streams. The time dimension checks for consistency across the time-steps and therefore useful in validating the halo catalogues. The use of phase-space information leads to high precision in recovering halo properties especially during close encounters such as mergers, in-falls, etc.

2.4.3 SUBFIND (Springel)

SUBFIND (Substructure Finder) (Springel et al., 2001b) is a 3-d finder built over FOF, identifies locally overdense, gravitationally bound regions within a background halo. Overdensities are identified using a FOF algorithm with a standard linking length of b=0.2. The density at each particle is computed using kernel interpolation to closest n neighbours. The particle with highest density forms the parent halo. The subsequent higher densities form the subhalo candidates. The edge of a subhalo is determined by saddle point in the density profile connecting the subhalo candidates. Each subhalo candidate is checked for self boundedness. Particles with positive total energy are considered unbound and are discarded. If the number of bound particles is greater than a minimum threshold, the candidate is a subhalo. The remaining particles are assigned to the background halo.

2.4.4 MENDIETA

MENDIETA (Mario Agustín Sgró (2015)) is a 3-d finder built over FOF with a particle resolution of 20. For each subhalo, FOF is run to isolate local overdensities. All particles with positive total energy are unbound and assigned to the most massive subhalo. The resulting subhalo catalogue is used as a new input catalogue for the next level of subhaloes and the procedure is repeated with a decreased linking length parameter. Finally, unbinding is executed in the main halo and all unbounded particles are marked as particles that do not belong to any substructure.

2.4.5 HSF (Maciejewski)

Structures such as streams and caustics are well defined only in phase-space. HSF (Hierarchical Structure Finder) (Maciejewski et al., 2009), a modified version of SUBFIND is a phase-space FOF finder which identifies all types of structures including pure streams, tidal streams, tidal tails and caustics. With its full phase-space capabilities, HSF is well suited for dynamical analyses such as an infall, flyby or a merger. The algorithm identifies overdensities by tracing the isodensity contours dened by the saddle points.

2.4.6 STF (Elahi)

STF (Structure Finder) (Elahi et al., 2011) a 6-d finder, uses velocity space information to accurately identify substructures. The local velocity distribution provides information on substructures that stand out (i.e. strongly clustered) relative to host background halo, which is a smooth Maxwellian. FOF is used to group the substructures and groups with positive total energy are discarded. As this finder does not use full phase-space, it is computationally more efficient than the other phase-space finders. This finder is best suited to identify diffused tidal streams.

2.4.7 ADAPTAHOP (Tweed)

ADAPTAHOP is a 3-d spherical overdensity finder. It uses a 20 particle SPH kernel to identify local density maxima (Colombi, 2013). For each particle, n closest neighbours are identified using standard Octral tree algorithm. Particles are grouped around those density peaks. The density threshold is increased to separate the groups (nodes) using the saddle points. The particles between the saddle points form the subhaloes. A structure tree is constructed with these nodes, and every sub-node is a subhalo. Haloes and subhaloes are defined using this hierarchical tree of density peaks. ADAPTAHOP does not have an unbinding procedure and therefore unbound particles may still be part of the candidate objects. This also makes is ideally suited for astrophysical applications such as streams that considers full mass.

2.4.8 H3D and H6D (Ascasibar)

HOT (Hierarchical Overdensity Tree) + Fiesta (Field Estimator for Arbitrary Sciences) (Ascasibar and Binney, 2005), is a clustering analysis tool with a wide scope of application across many research domains including biological and social sciences. This finder comes in two variants. While HOT3D (H3D) uses particle locations to find bound haloes, HOT6D (H6D) adaptively uses the full phase-space information. This method uses sample points and tessellates the three dimensional space and assigns volume at each point using a binary tree. Following this, an adaptive kernel is used to compute density at each sample point. The edges of a haloes are defined using isodensity contours at saddle points. Both H3D and H6D does not perform unbinding. H6D is effective in detecting tidal streams.

2.4.9 HBT (Hierarchical Bound Tracing) (Han)

HBT is a FOF based finder which not only identifies haloes and subhaloes, but keeps an evolutionary record of the mergers by means of a merger tree (Han et al., 2011). The extra dimension of time along with 3 space provides the edge in identifying consistent structures across different times (snapshots). This finder is also termed as a minor implementation of a semi-analytic model for CDM subhaloes. The size of a subhalo is limited by the tidal radius, which is defined as the radius of the satellite subhalo at which its gravity equals the tidal force of the host halo. About 95% of the particles within the tidal radius are considered bound. It has a robust unbinding algorithm.

2.4.10 VOBOZ (Neyrinck)

VOBOZ (VOronoi BOund Zones) is a parameter free, 3-d halo finding algorithm (Neyrinck et al., 2005) which uses watershed algorithm (Voronoi tessellation) to identify haloes. For each particle, density is calculated and compared with its neighbours and the neighbour with the highest density is chosen. The procedure is repeated until a density peak is reached, which is considered as the centre of a potential halo. A density peak becomes a subhalo if the ratio of the density peak to the density at saddle point crosses a threshold. Unbinding is used iteratively to remove gravitationally unbound particles.

2.5 Unbinding

"Unbinding" is a procedure to remove particles or objects with positive total energy. The most common technique involves calculating the escape velocity at each particle's position. A particle is unbound if a particle's velocity is greater than the local escape velocity. The escape velocity is computed using the potential as $V_{esc} > \sqrt{2\Phi}$ where Φ is the potential.

The unbinding procedure followed in the AHF is described as follows.

- Step 1: Obtain initial set of particles and determine M_{vir} (Virial Mass) and R_{vir} (Virial radius)
- Step 2: Calculate potential ϕ
- Step 3: If the particle's velocity is greater than escape velocity, then the particle is unbound.
- Step 4: Bound particles define a new set of initial particles for M_{vir} and R_{vir} and the procedure is iterated again from step 2 to 4 until there are no more unbound particles.

Knebe et al. (2013) has discussed many differences between halo finders in performing unbinding. Firstly, differences can arise while calculating the potential. Some finders compute the potential by integrating the Poisson equation assuming spherical symmetry (e.g. AHF). Others finders such as HOT3D and HOT6D use non spherical density profiles. Differences also exist due to number of particles unbound in single iteration. Some finders remove one particle at each iteration before recalculating the potential. Other finders remove fraction of total particles before iterating over. Differences also exist in the termination condition. Some finders exit the iteration when all the unbound particles are removed. Others stop the iteration as the fraction of particles removed reaches a minimum. Some finders such as ADAPTAHOP, do not have an unbinding feature. Halo finders which does not have unbinding procedure may produce halo catalogues contaminated with low mass spurious (discussed in results chapter, section 3.4.1) haloes. Knebe et al. (2013) argues that configuration space finders may include unbound particles (false positives) as they do not have velocity information and hence recommends running an unbinding procedure for all configuration space finders unless the application wants to include particles that are unbound (e.g. lensing, X-ray properties, tidal relics, streams, Sunyaev-Zeldovich effect, Sachs-Wolfe effect). Table 2.2 describes the unbinding procedure followed by each of the halo finders, with the first column representing the name of the halofinder, second column describing whether an unbinding procedure exists in the halofinder and the third column providing a summary of the unbinding procedure followed by the halofinder.

2.6 Summary

This chapter describes the general algorithm for halo finding and provides an introduction to various halo finders participating in this analyses project.

Halofinder	Unbinding	Description
AHF	Y	Particles are unbound if their velocity crosses the escape velocity of the system. M_{vir} and R_{vir} are recalculated and particles are removed iteratively. Assumes spherically symmetric potential (Knollmann and Knebe, 2011).
ROCKSTAR	Y	Single pass unbinding using modified Barnes-Hut Algorithm to compute potential energies of the particles with binary space partitioning(BSP) tree. Particles with positive energies are removed. The unbinding procedure does not output halos where fewer than 50% of the particles are bound Behroozi et al. (2012).
SUBFIND	Y	Particle is removed if the total energy(Kinetic plus Potential energy) is greater than zero. Unbinding is iterated, with no more than quarter of particles removed at once. Unbinding of particles in physical coordinates (3D). centre of the potential is determined by the position of the most bound particle (Springel et al., 2001b).
MENDIETA	Y	Particles with positive total energy(potential plus kinetic energies) are removed from a subhalo and assigned to its host subhaloMario Agustín Sgró (2015).
HSF	Y	Iterative unbinding in 6D. Quarter of the particles with positive energies are unbound in each iteration Maciejewski et al. (2009).
STF	Y	Iterative unbinding procedure removing particles with total positive energies (Elahi et al., 2011).
ADAPTAHOP	N	No unbinding
H3D and H6D	N	No unbinding.
HBT	Y	Particles are iteratively unbound till the bound mass converges using core-averaged unbinding algorithm designed to tolerate contamination. For each iteration, the reference frame is chosen to be the centre of mass and bulk velocity of an inner-most core consisting of a certain fraction of the remaining particles with the lowest potential Han et al. (2011).
VOBOZ	Y	Particles are iteratively unbound if their velocities exceed the escape velocity from their subhalo. The most unbound particles are removed in each iteration using a boundedness threshold which is changed in each iteration Neyrinck et al. (2005).

Table 2.2: Different halo finders and the unbinding procedure followed.

Chapter 3

Results

3.1 Introduction

This chapter presents the results of comparing the subhalo mass, size and unbinding procedures, across the participating halo finders using the two analyses, the common-analysis and the own-analysis on Aquarius simulation data. The 'common-analysis', is a common pipeline, with common set of methods for halo centering, unbinding and deriving basic attributes such as mass, size, etc. The "own-analysis" is each halo finder's individual analysis on the same simulation data. The 'common-analysis' has a functionality similar to AHF (Amiga Halo Finder). Therefore, comparing a halofinder with 'common-analysis' can be considered as comparing with another halo finder. Sections 3.2 and 3.3 present the results of comparing mass and size respectively across the finders and analyse the reasons for the mass scatter. The section 3.4 presents the results of comparing distributions of unbound subhaloes and shows that the choice to unbind and the halo finder impacts the scatter in the mass.

3.2 Mass comparison

The subsection 3.2.1 presents the subhalo mass functions for the two analyses and presents the potential reasons for mass scatter from the literature. The subsection 3.2.2 shows that the inclusive-exclusive mass contributes around 10% to the mass scatter. Further, the subsection 3.2.3 presents and the results from mass comparison across the two analyses and investigates into the sources of scatter in the mass.

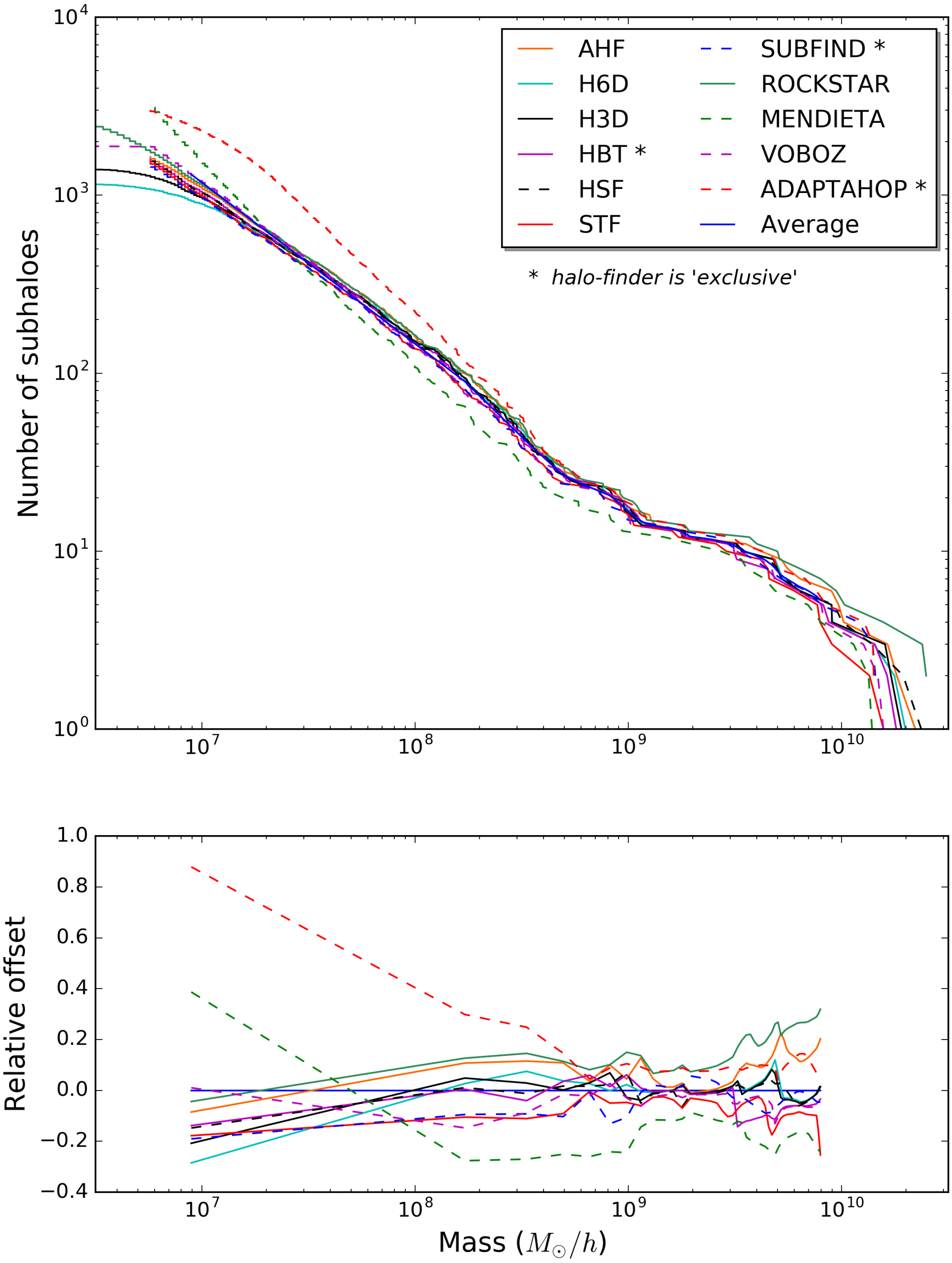

Figure 3.1: Top panel shows cumulative subhalo mass function from the common-analysis for the eleven halo finders as indicated in the legend. Bottom panel shows residuals with a mass scatter of 10% from the mean. The blue line is the average mass.

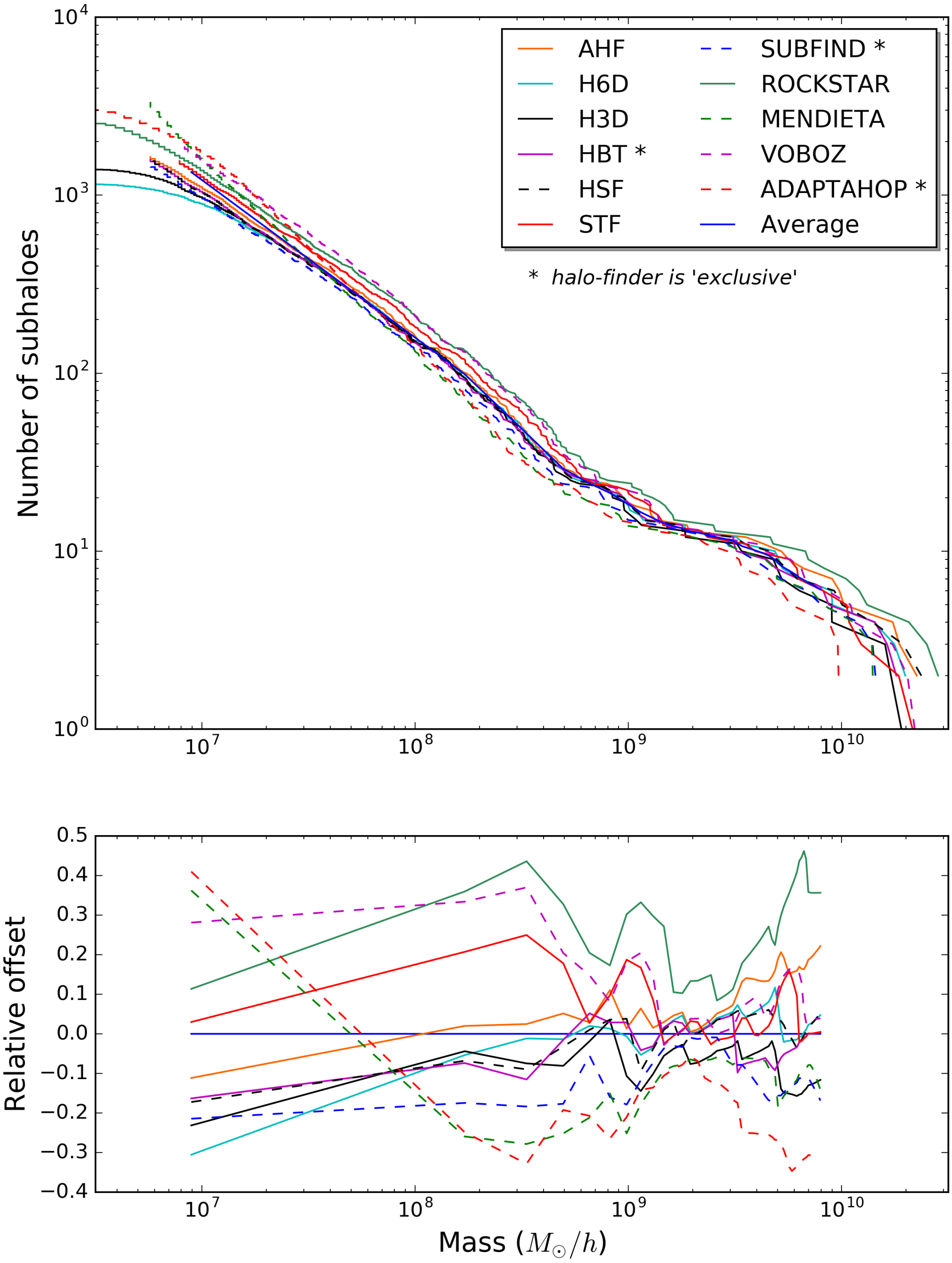

Figure 3.2: Top panel shows cumulative subhalo mass function for each finder's own-analysis from the different halo finders as indicated in the legend. Bottom panel shows residuals with a mass scatter of up to 20% from the mean. The solid blue line is the average mass.

3.2.1 Subhalo Mass Function

Figures 3.1 and 3.2 show cumulative subhalo mass functions for the common-analysis and own-analysis respectively. Figure 3.1 is in good agreement with Figure 3 in Onions et al. (2013) which constrains the average scatter in the mass to 10%. Figure 3.2 shows a scatter of 20% for each finder's own-analysis. The bottom panel shows residuals with scatter amplified between the masses 10^8 and $10^{9.5}$. The scatter in the own-analysis is at least a factor of two larger than in the common-analysis. The solid blue line marks the reference showing the average of the values. At low mass end, ADAPTAHOP recovered the maximum number of subhaloes and H6D recovered the least. At the high mass end, ROCKSTAR recovered the maximum and ADAPTAHOP found the least. The Table 3.1 describes the participating halo finders used in this comparison study with definitions for subhalo mass and size as found in the literature. Firstly, differences exist in the mass definitions. Halofinder such as AHF computes the virial mass(M_{vir}) from M_{200} whereas ROCKSTAR computes it from V_{max}. Secondly, the density contrast differs across finders. AHF uses Δ_{vir} =178 from the spherical tophat collapse whereas ROCKSTAR uses $\Delta_{vir} = 360b$ and VOBOZ uses ρ_{min} =100x(x can be background density or critical density based on setting). Thirdly, the choice of b(background density) or c(critical density) impacts the final properties. Lastly, HSF and HBT considers 95% of bound particles, however MENDIETA considers 91% of bound particles. AHF uses a different definition - the distance to the farthest bound particle within the 'tidal radius'. These factors could potentially lead to the scatter in the mass.

3.2.2 Inclusive or exclusive mass

One of the reasons for the scatter in mass is the option to include or exclude the substructures (Avila et al., 2014). Also, Onions et al. (2013) had shown that subhaloes account for about 10% of the parent halo mass. An 'inclusive' halofinder such as AHF and ROCKSTAR includes the bound subhalo masses to the parent halo mass. An 'exclusive' halofinder such as SUBFIND and HBT excludes the mass of the substructures. AHF and ROCKSTAR are 'inclusive', whereas SUBFIND and HBT are 'exclusive'. Figure 3.3 shows the cumulative subhalo mass function for ADAPTAHOP.

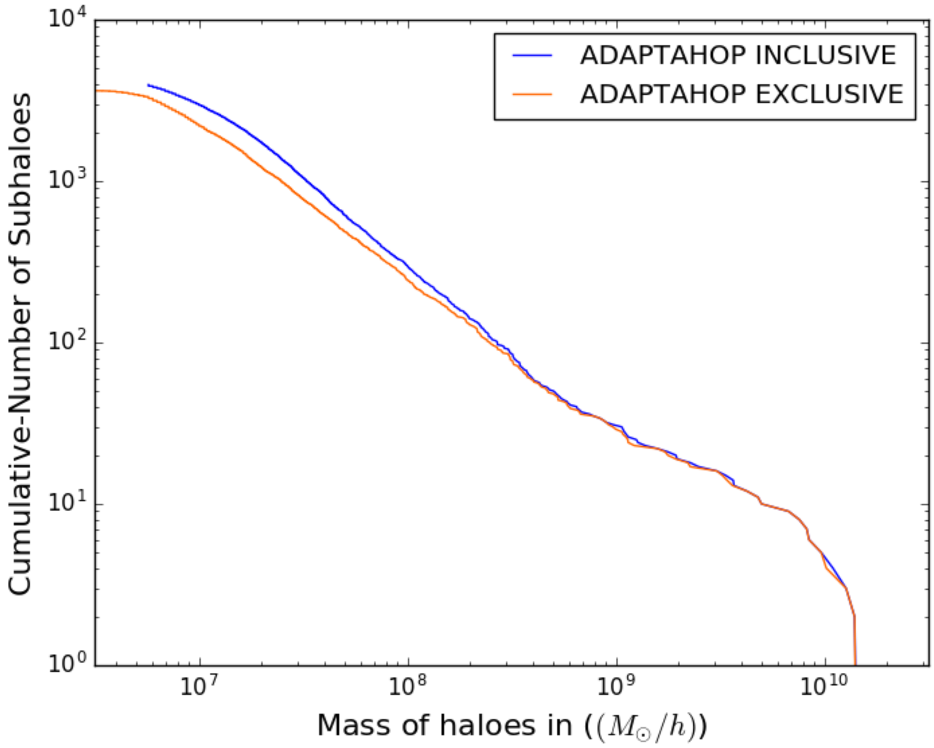

Figure 3.3: Cumulative mass functions for ADAPTAHOP that shows exclusive mass (red) and inclusive mass (blue). The inclusive mass is calculated using particle list ($N \times m_p$, where N is number of particles and m_p is mass of each particle). The exclusive mass is using M_{200c}, which is the mass returned from common-analysis own-unbinding.

The red and the blue line correspond to the two mass definitions used. The blue line shows inclusive mass($N \times m_p$) where N is number of particles and m_p is mass of each particle for the subhalo. The red line shows exclusive mass M_{200c} , which is the mass returned from common-analysis own-unbinding. The inclusive mass (in blue) is consistently more than the exclusive mass (in red) and the gap increases at the low-mass-end. This indicates that the option to 'include' or 'exclude' contributes to the scatter in the host halo mass.

3.2.3 Matching the two analyses

For each of the eleven halo finders, subhalo catalogues were matched (on subhalo identifications), across the two analyses, the common-analysis and the own-analysis as shown in the Figure 3.4. A point lying close to the dashed line indicated that the mass of a subhalo remained consistent across the two analyses. A point lying

Halofinder	**Halo and subhalo edge**
AHF	$R_{vir} = (M_{200}/\frac{4}{3}\pi\rho_b\Delta_{vir}(z))^(\frac{1}{3})$ where default Δ_{vir} =178 (spherical tophat collapse) Page2 eq2 (Knollmann and Knebe, 2011)) Virial radius or the distance to the farthest bound particle within the 'tidal radius' AHF documentation page 56.
ROCKSTAR	$R_{dyn,vir} = V_{max}/(\frac{4}{3}\pi G\rho_{vir})^(\frac{1}{2})$ where ρ_{vir} is from Bryan and Norman(1998) $\rho_{vir} = 360b$ Page 5 of Behroozi et al. (2012)
SUBFIND	$R_{vir} = (M_{200c}/\frac{800}{3}\pi\rho(z))^(\frac{1}{3})$, ρ =200c, page 7 (Springel et al., 2001b)
MENDIETA	91% of bound particles from documentation Mario Agustín Sgró (2015)
HSF	ρ =200c, 95% of the bound particles, page 2 (1330) and page 3(1331) in Maciejewski et al. (2009)
STF	Δ =200 page 4 (323) in (Elahi et al., 2011), Page (8) 327 in (Elahi et al., 2011)
ADAPTAHOP	$R_{vir} = (M_{200c}/\frac{800}{3}\pi\rho(z))^(\frac{1}{3})$, ρ =200c page 3 in (Colombi, 2013).)
H3D and H6D	ρ =200c , R_{max}, Page 8(879) of Ascasibar and Binney (2005)
HBT	ρ =101, 95% of the bound particles within the tidal radius, page 7 in Han et al. (2011)
VOBOZ	ρ_{min} =100x Page 6 in Neyrinck et al. (2005) , Sheth et al. (2001)

Table 3.1: Subhalo edge definitions as listed by various halo finders in the literature.

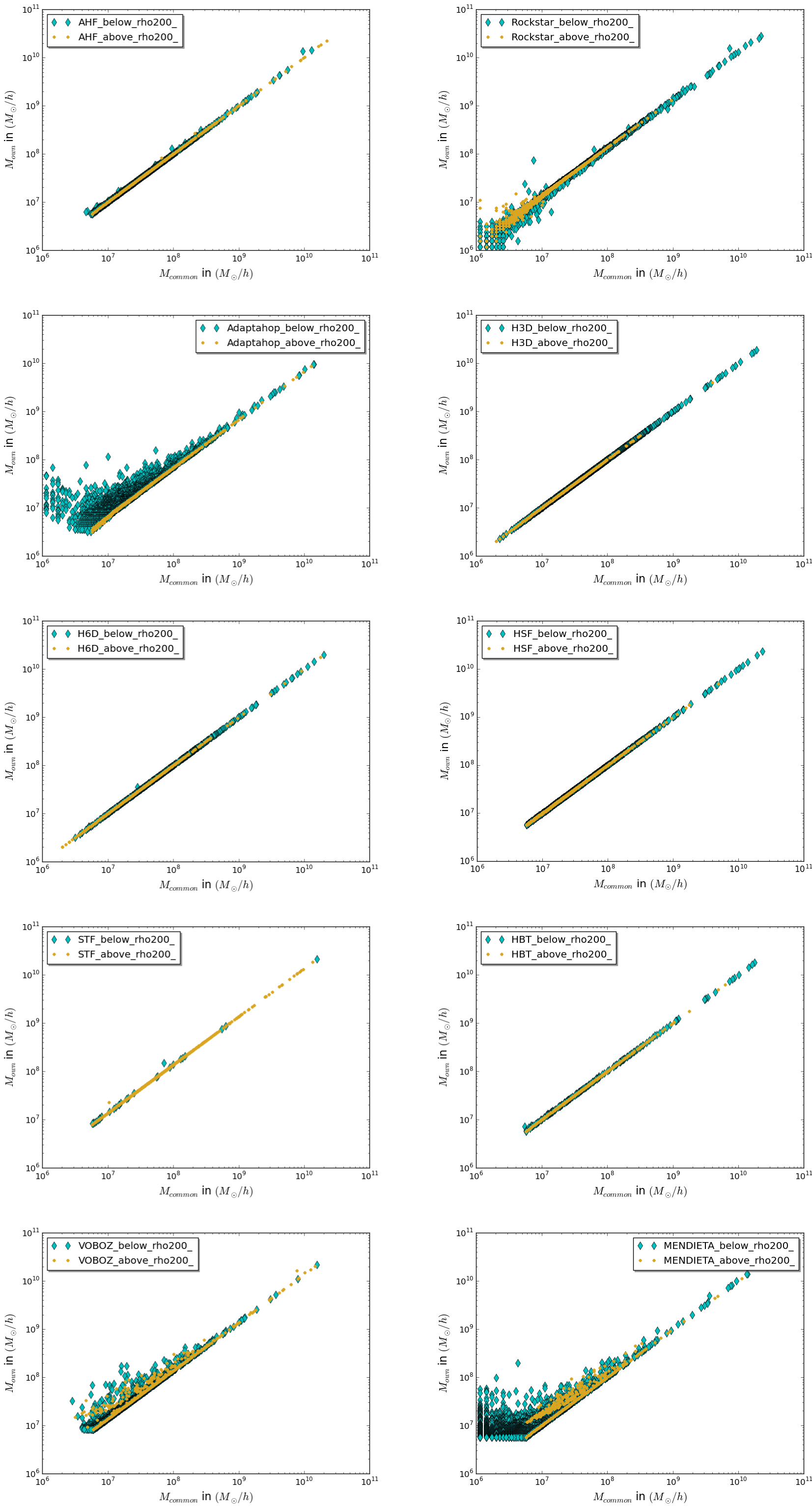

Figure 3.4: Mass of subhalo from their own-analysis plotted against the mass from common-analysis. The cyan diamonds represent subhaloes with density above the density threshold $\rho_{threshold}$. The yellow circles represent subhaloes with density below the density threshold.

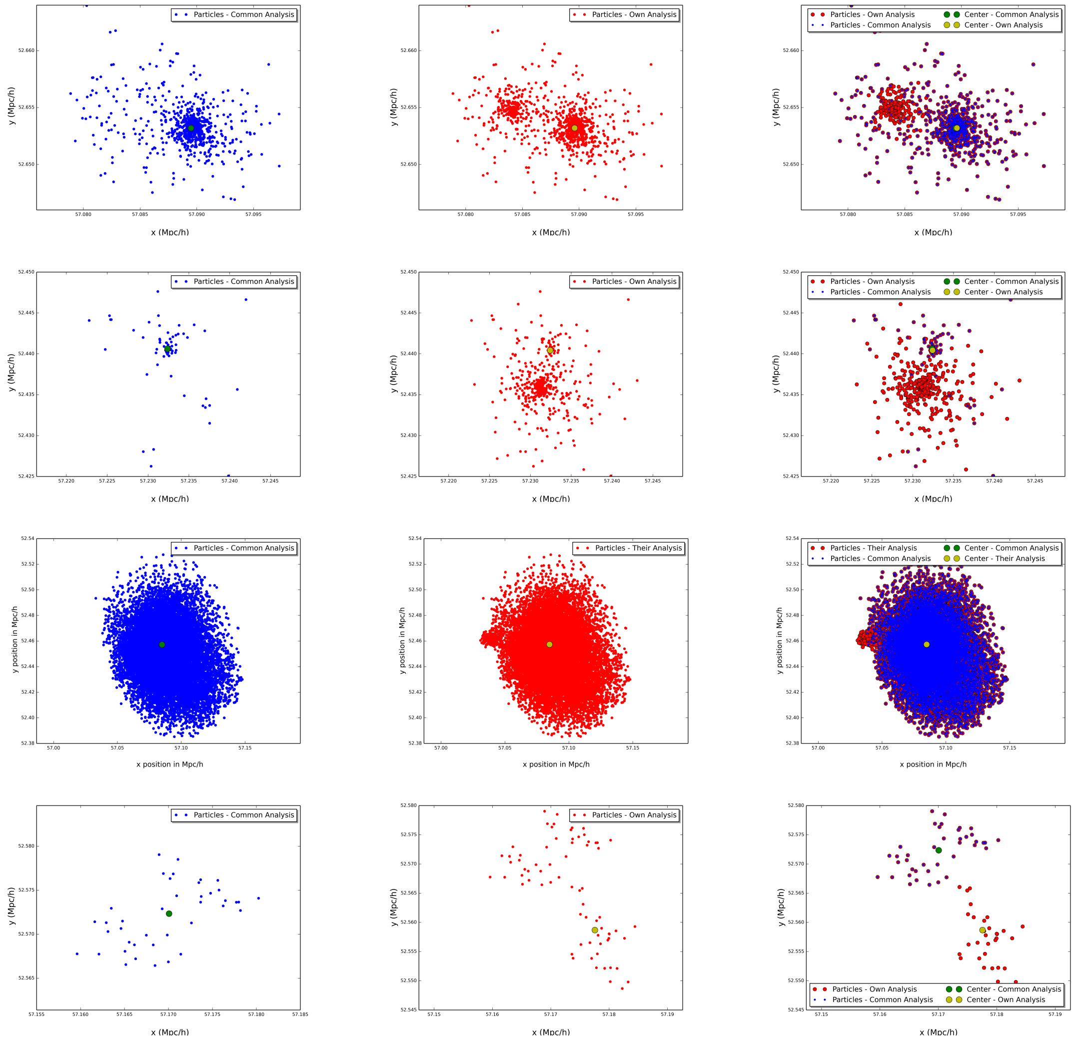

Figure 3.5: 2D plots showing contents of sample haloes from various halofinders AHF, VOBOZ, HBT and MENDIETA. The leftmost column shows the subhalo particles (in blue) as recovered in the common-analysis, the second column shows subhalo particles (in red) from their own-analysis. The right most column shows the overlap of the images from the first and second column, showing substructures found in own-analysis, but missing from the common-analysis. The missing substructures account for the mass differences.

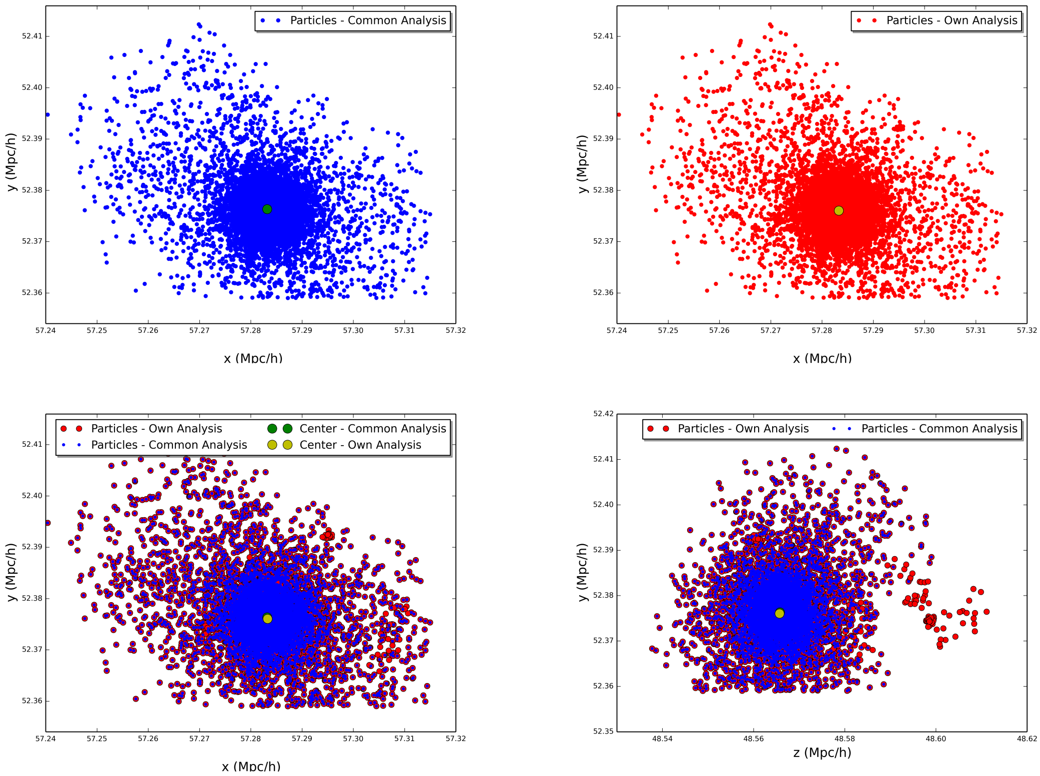

Figure 3.6: Constituents of halo (ID 1363) plotted for MENDIETA. The top left image is from common-analysis while the top right image is from their own-analysis. The bottom images were produced by overlapping both the images, showing missing structures. An illustration of simulation artifact seen in all the images, as if the halo is chopped off.

further away from the dashed line indicated that the mass was not consistent across the two analyses. The cyan diamonds represent subhaloes with density above a density threshold. The yellow circles represent subhaloes with density below the density threshold. The density threshold was calculated using the density of the most massive halo as discussed in the later section 3.3. As common-analysis follows an identical procedure to AHF, the top left plot in Figure 3.4 has a good match with all the subhaloes lying close to the 45° line. Halofinders H3D, H6D, HBT and STF do not show significant scatter across the two analyses. However, ROCKSTAR, MENDIETA, VOBOZ and ADAPTAHOP showed high scatter at the low mass end. Cyan subhaloes representing the high density subhaloes in ADAPTAHOP, VOBOZ and MENDIETA are more massive in own-analysis. The reasons for this scatter will be discussed later in section 3.3. For VOBOZ, the mass of subhaloes in own-analysis was higher than the mass in common-analysis. This can be explained by the fact that VOBOZ used $\delta = 101$ in their own-analysis (see table 3.1) as opposed to $\rho = 200$ in common-analysis. A low density contrast equates to a large volume, hence a large initial mass and therefore a large final mass. This shows that the scatter in the mass was due to different virial mass definitions employed across finders.

A sample of 20 outliers which were away from the dashed line were picked up and investigated for traits that illustrated mass differences. Each out-lier was investigated by exploring the configuration space by plotting the particle positions which were extracted from the simulation snapshot. The particle positions from both analyses were overlapped and compared to spot any traits such as missing substructures, mismatch in the halo centres or simulation artifacts. This process of searching for the outliers and visualizing the subhalo in configuration space was automated for each halo finder. Figure 3.5 shows outliers from various halo-finders illustrating signatures of mass difference. The top row shows AHF(subhalo id 584), second row shows VOBOZ (subhalo id 175551), third row shows MENDIETA (subhalo id 3) and the bottom row (subhalo id 2493) demonstrates missing substructures and centre offsets. The AHF subhalo in the top row has a mass of 2.6x$10^7 M_\odot/h$ and 2.1x$10^7 M_\odot/h$ in own-analysis and the common-analysis respectively. Similarly the plots in the second row show a subhalo found in VOBOZ with mass 1.7x$10^8 M_\odot/h$ and 2x$10^7 M_\odot/h$ in own-analysis and the common-analysis respectively. The third row shows a subhalo found in HBT with a mass difference of 2.1x10$^5 M_\odot/h$. The plots in the third column were produced by an overlap of the particle positions from the two analyses. The bottom row shows a subhalo in MENDIETA which is a halo picked from the low mass end of the mass with mass of 2x10$^7 M_\odot/h$ and 1x10$^7 M_\odot/h$ in their own-analysis and common-analysis respectively. This difference in mass highlighted in the third column, amounts to one half of the structure not being present in the common-analysis. Figure 3.6 shows a subhalo in MENDIETA demonstrating missing substructures and a simulation artifact. The subhalo is selected from the mid-mass range such that it lies away from the dashed line with masses 3.1x10$^9 M_\odot/h$ and 3.0x10$^9 M_\odot/h$ in their own-analysis and the common-analysis respectively.

3.3 Size comparison

This section presents the results from comparison of subhalo sizes across the two analyses. The investigation begins by exploring all the possible size definitions in the AHF finder. AHF was chosen because common-analysis was built over AHF. AHF documentation states that it uses two definitions for halo edge (see Figure 2.5). The first definition is the virial radius ($\rho_{vir} = 200\rho_{ref}$) where ρ_{ref} is background density or critical density. This definition does not hold good for all subhaloes as the edge density may not drop below the virial density ($\rho_{vir} = 200\rho_{ref}$), in which case the "distance to the farthest bound particle within the tidal radius" is used to determine the edge. In order to investigate if these two definitions lead to two sets of subhalo sizes, density was plotted against the size for all the finders as shown in the Figure 3.7. The density was chosen as it is tightly related to density contrast. All the plots show segregation in the densities as depicted by the two colours, cyan and yellow from the common-analysis, red and blue from the own-analysis. All the plots show the formation of characteristic line at 10^4 indicating a specific density, henceforth referred as threshold density. The threshold density line is formed due to the virial density coming from the first definition $\rho_{vir} = 200\rho_{ref}$. In order to confirm this, the average density for the most massive halo (which is the host halo) was computed. The AHF documentation mentions that the host halo uses the first definition (virial density). All the plots show that the average density of the most massive halo (host halo) lies on this threshold line. The threshold density line that bifurcates the two sets suggests that, the subhaloes with density below the virial density $\rho_{threshold}$ represented by yellow points, was derived from the first definition. The subhaloes with density above the $\rho_{threshold}$ represented by cyan points, was derived from the second definition "distance to the farthest bound particle within the tidal radius". The red and blue points represent subhaloes from the own-analysis, the cyan and yellow points represent the subhaloes from the common-analysis. The plot for the AHF (top left) shows that cyan and yellow points precisely overlap the red and blue points.

ADAPTAHOP showed scatter above the dashed line which could be attributed to the fact that ADAPTAHOP has no unbinding procedure and hence the radius measured in own-analysis was higher compared to the radius in common-analysis. All the halofinders showed scatter in density for all sizes with the exception of ROCKSTAR. ROCKSTAR showed constant density for all the subhaloes in their own-analysis. This suggests that for all the finders (with the exception of ROCKSTAR), a direct relation could not be established between the mass and size, as density did not remain constant across the sizes. In the case of ROCKSTAR, it was evident that the size was derived from the mass as density remained constant across all sizes. VOBOZ showed subhaloes (seen in blue) scattered towards the high end of the size in the own-analysis. This was due to the fact that VOBOZ used a critical density of $\rho_c = 100$ as shown in the Table 2.1. With this definition, the radius recovered was expected to be larger in their own-analysis.

Figure 3.8 shows the radius (size) from own-analysis plotted against the radius from the common-analysis. A bigger radius in the common-analysis corresponds to subhaloes that are below the dashed line closer to the x-axis, and a bigger radius in own-analysis corresponds to subhaloes that are above the dashed line closer to the y-axis. The cyan circles represent subhaloes with density above the density threshold $\rho_{threshold}$ as described in the section 3.3. The yellow circles represent subhaloes with density below the density threshold $\rho_{threshold}$. The common-analysis showed accurate match with AHF (top left plot in the Figure 3.8) and most of the subhaloes lie on the dashed line(45°). In the case of VOBOZ, the size of subhaloes in own-analysis on both the ends was higher than the size from the common-analysis. This is because

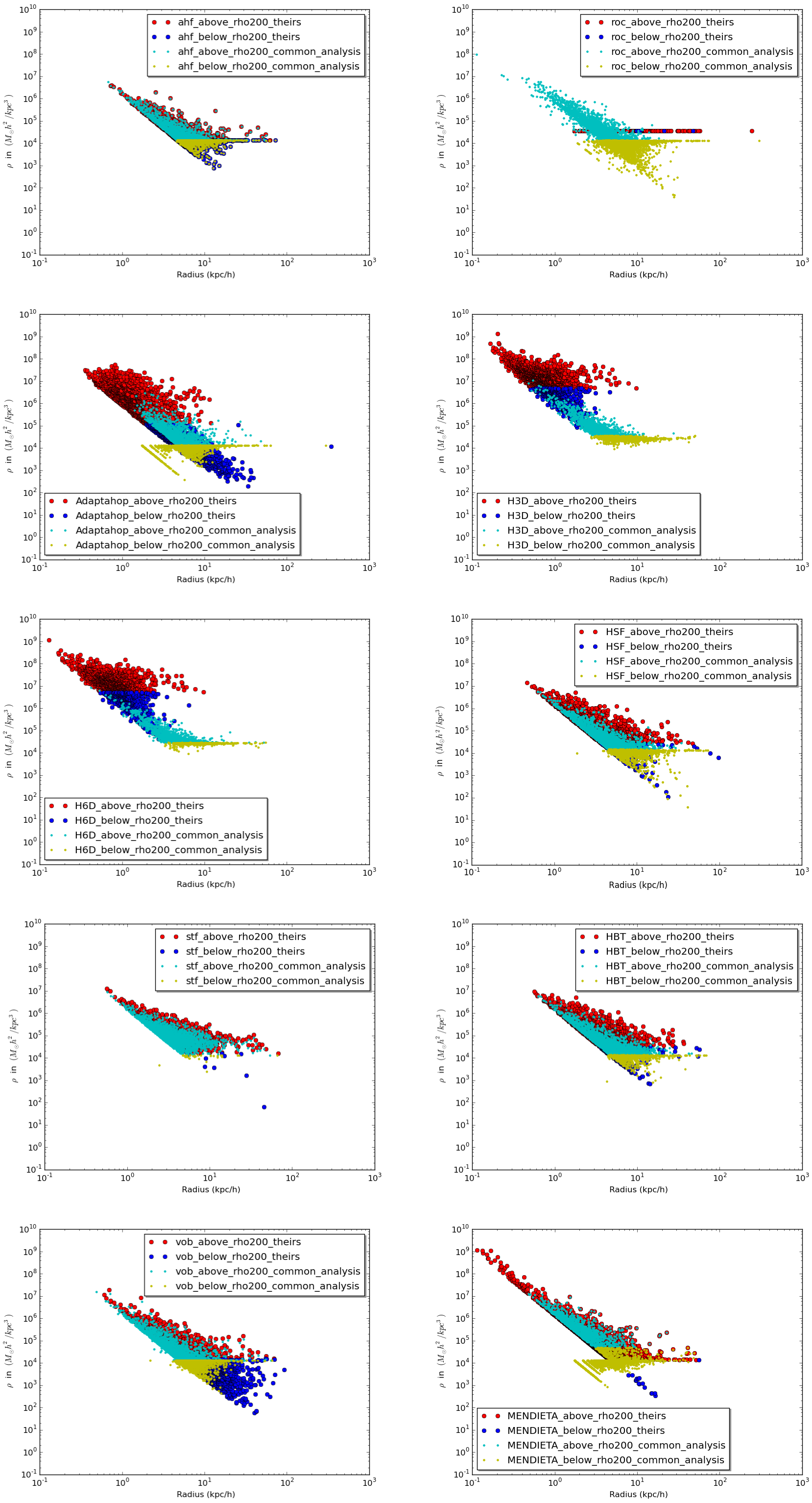

Figure 3.7: Density plotted against radius of subhaloes for various halo finders with red and blue for their own-analysis, cyan and yellow for common-analysis. Cyan and red represent subhaloes with density above the threshold density. Yellow and blue represents subhaloes below the threshold density.

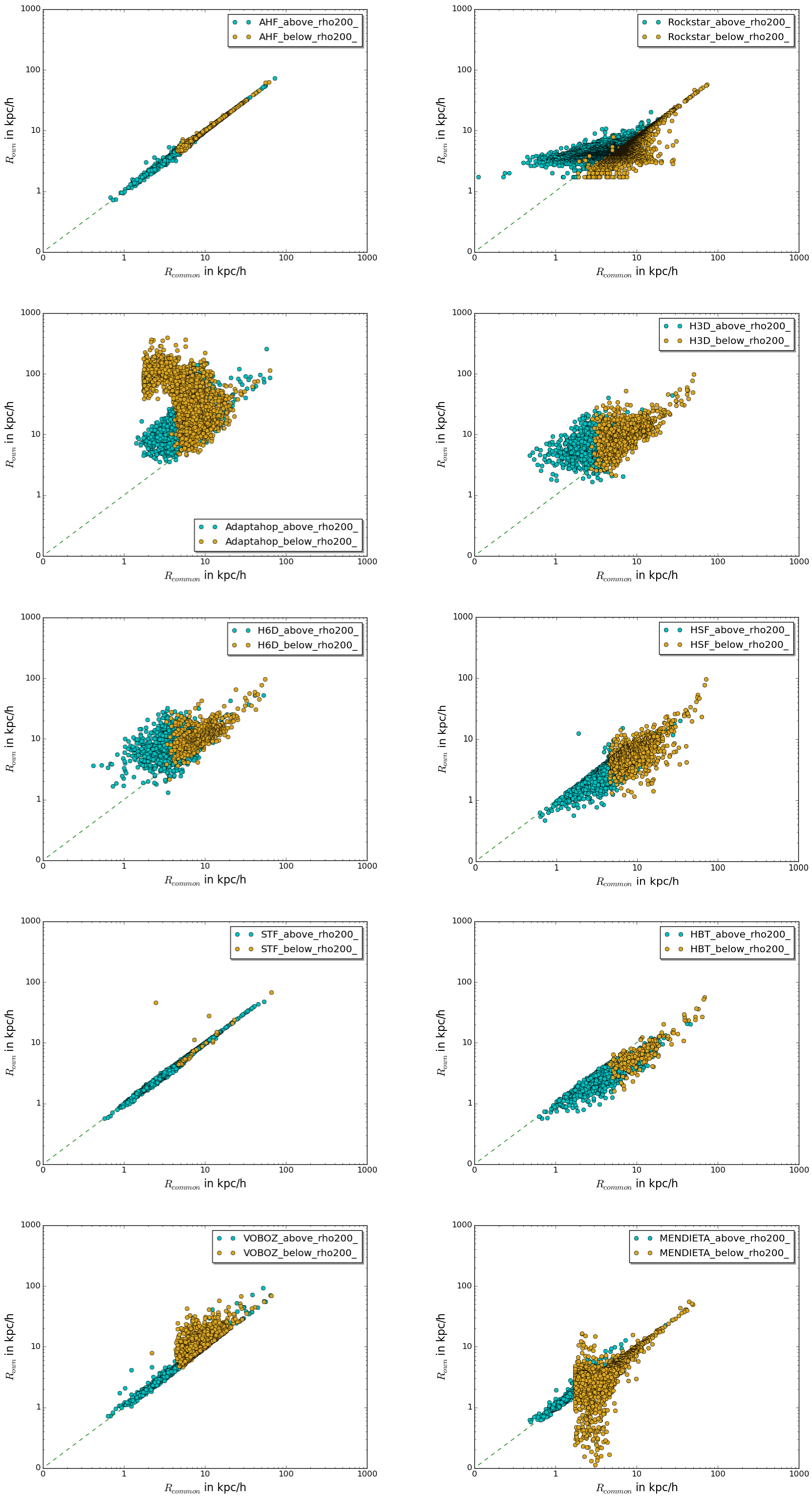

Figure 3.8: Radius from their own-analysis plotted against radius from common-analysis for subhaloes from various halo finders. The cyan represents subhaloes with density above the threshold density. $\rho_{threshold}$. The yellow represents subhaloes with density below the density threshold.

$\delta = 101$ was used by VOBOZ (see table 3.1) as opposed to $\rho = 200$ in the common-analysis. A lower density contrast amounts to a larger volume and hence a larger size. This example shows that the scatter in the mass was likely due to the different virial mass definitions. ADAPTOHOP, H3D and H6D show increased size which may be attributed to the absence of unbinding routine in them. Figure 3.8 shows a vertical split in the size due to density bifurcation for all the halo finders with an exception of ROCKSTAR. The two size definitions from AHF leads to two sets of densities and therefore leads to two sets of sizes. This showed that the sizes were derived from densities and not directly from masses. This leads to the conclusion that the sizes from the halo catalogues may not be trusted to be in consistent with the masses.

For each of the halo finders, 20 sample outliers lying away from the dashed line (see Figure 3.8) were picked and further investigated in order to find the cause of the scatter in the size. Figure 3.9 shows two sample subhaloes from ROCKSTAR with different radii inferred from the two analyses. The size of the halo differs by 6kpc in the left panel and 15kpc in the right panel. The yellow circle represents the radius returned by the common-analysis and the cyan circle represents the radius returned from ROCKSTAR's own-analysis. The plot on the left shows that ROCKSTAR (own-analysis) inferred a larger radius compared to the common-analysis. However, the plot on the right shows that ROCKSTAR inferred a smaller radius compared to the common-analysis. This is an illustration of the scatter in the sizes between ROCKSTAR and common-analysis. The subhalo on the left with ID=13227 had radius 9kpc in own-analysis and 3kpc in the common-analysis. The root cause for this may be attributed to the fact that ROCKSTAR defines the radius as

$$R_{dyn,vir} = V_{max}/\sqrt{(\frac{4}{3}\pi G\rho_{vir})(\frac{1}{2})} \tag{3.1}$$

where V_{max} is the maximum circular velocity and $\rho_{vir} = 360b$, where b refers to background.

While, the common-analysis used AHF's definition

$$R^3_{vir} = M_{200}/\frac{4}{3}\pi\rho_b\Delta_{vir}(z) \tag{3.2}$$

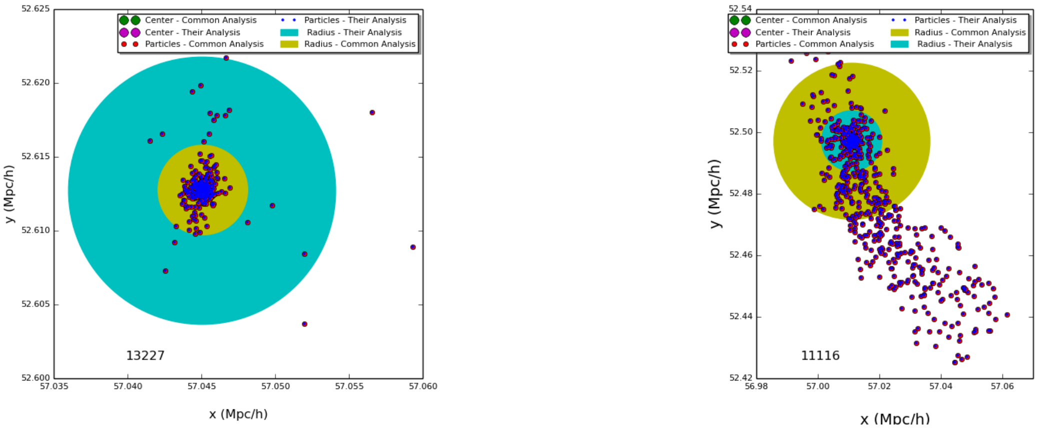

Figure 3.9: Two sample subhaloes in ROCKSTAR showing different radii in the two analyses. The yellow circle represents the radius from common-analysis and the cyan from own-analysis. The size of subhalo ID=13227 (left) differs by 6Kpc and the size for subhalo ID=11116 (right) differs by 15Kpc between the two analyses.

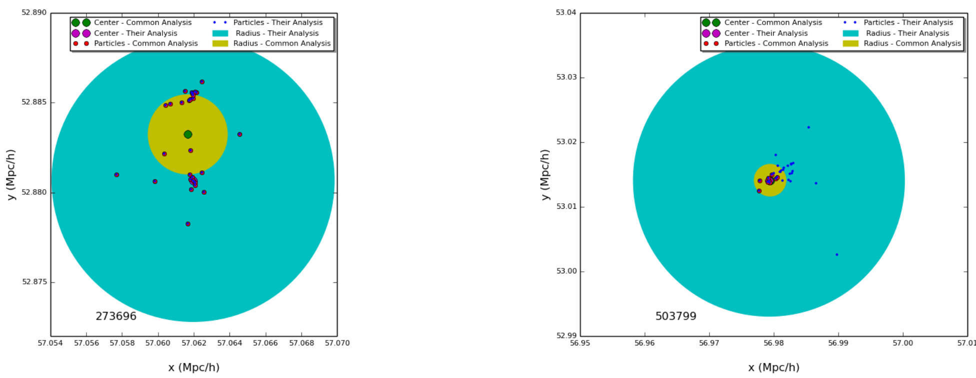

Figure 3.10: Two sample subhaloes in VOBOZ showing different radii in the two analyses. The yellow circle represents the radius from common-analysis and the cyan from own-analysis. The size of subhalo ID=273696 (left) differs by 5.6Kpc and the size for subhalo ID=503799 (right) differs by 19Kpc between the two analyses.

where Δ_{vir} =178 at z=0 as shown in Table 2.1.

The subhalo on the right with ID=11116 has radius of 10kpc in ROCKSTAR's own-analysis and 25kpc in the common-analysis. The Figure 3.10 shows two sample haloes from VOBOZ with a radius difference of 5.5kpc and 19kpc between the two analyses (for the subhalo IDs 273696 and 503799) respectively. This is because the own-analysis used ρ_{min} =100x and the common-analysis used AHF's definition as in the equation 3.2. The left panel in the Figure 3.10 illustrates similar trend in VOBOZ with size approximately 31kpc in own-analysis and 6kpc in common-analysis. Furthermore, the centres were offset between the analyses.

The Figure 3.11 shows two subhaloes from MENDIETA that showed radius larger by 14kpc in own-analysis as compared to common-analysis. The subhalo on the left plot with ID=4124 lies at the high end of the radius along the y-axis (see Figure 3.8), where the radius in own-analysis was larger than the radius in the common-analysis. For the halo on the right with ID=3701, the radius inferred by the own-analysis was smaller by 3kpc. Figure 3.7 shows a plot of density versus radius and Figure 3.8 compares the radius across the two analyses. Figures 3.9, 3.10 and 3.11 illustrate the size differences across the analyses.

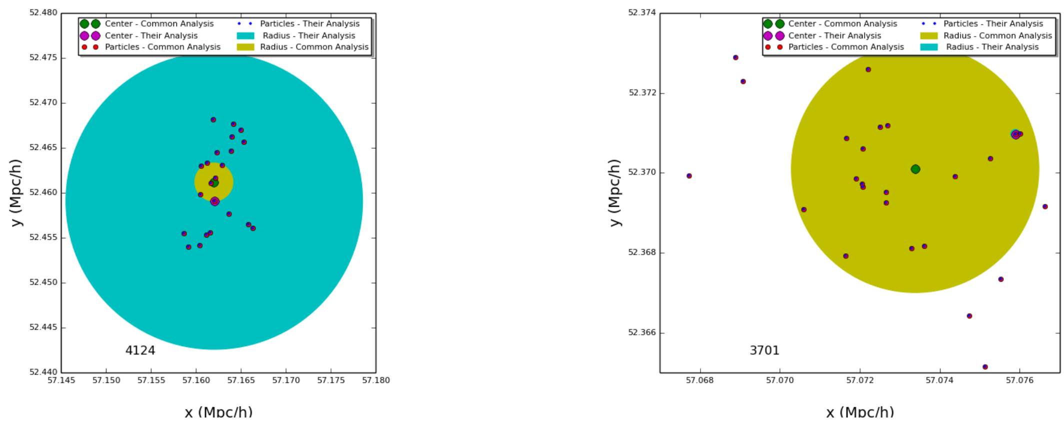

Figure 3.11: Two sample subhaloes in MENDIETA showing different radii in the two analyses. The yellow circle represents the radius from common-analysis and the cyan from own-analysis. The size of subhalo ID=4124 (left) differs by 14Kpc and the size for subhalo ID=3701 (right) differs by 3Kpc between the two analyses. Furthermore, the centres are offset.

3.4 Unbinding

This section describes the impact of the choice of unbinding (ON/OFF) and the choice of a halo finder, to the scatter in the mass and size. This is achieved by comparing the subhalo catalogs available for the three unbinding modes in common-analysis. The three unbinding options are as follows : (a) no-unbinding (unbinding OFF), (b) own-unbinding (unbinding ON) and common-unbinding (unbinding ON at the common-analysis as well as at each finder level).

Figure 3.12 shows the results of comparing subhalo mass from each finder's own-analysis, to the mass from the common-analysis, for all the three unbinding options. The top section of the plot represent each finders own-unbinding option for common-analysis with approximately 10-20% scatter for ROCKSTAR, MENDIETA, VOBOZ and ADAPTAHOP with the rest of the halo finders having low scatter. The middle section presents the common-unbinding option with an overall increased scatter of approximately 20% as compared to own-analysis. The bottom section presents the results for no-unbinding that shows higher scatter in general for all finders and more specifically for MENDIETA and VOBOZ in comparison to common-unbinding. The top, middle and bottom plots present each finder's own-unbinding, the common-unbinding and no-unbinding respectively. The scatter increases from own-unbinding (top-panel) to common-unbinding (middle-panel) for STF, H3D, H6D, HBT and MENDIETA. The scatter further increases from own-unbinding (top-panel) to no-unbinding (bottom-panel) for VOBOZ, H3D, HBT MENDIETA. This comparison from unbinding-on (own-unbinding, top-panel) to unbinding-off (no-unbinding, bottom-panel) suggests that that own-unbinding option has least scatter. This corroborates or re-proves the use of own-unbinding data in the common-analysis project Onions et al. (2013). Also, please note that both the mass functions in Figure 3.2 and Figure 3.1 use own-unbinding data, the former using own-analysis own-unbinding, and the latter using common-analysis own-unbinding. Just the unbinding part of it is not executed in common-analysis, but executed by the individual finders themselves.

Figure 3.13 shows the results of comparing the size obtained from each finders own-analysis to the size obtained from the common-analysis for the same three unbinding options. The top, middle and bottom plots present each finder's own-

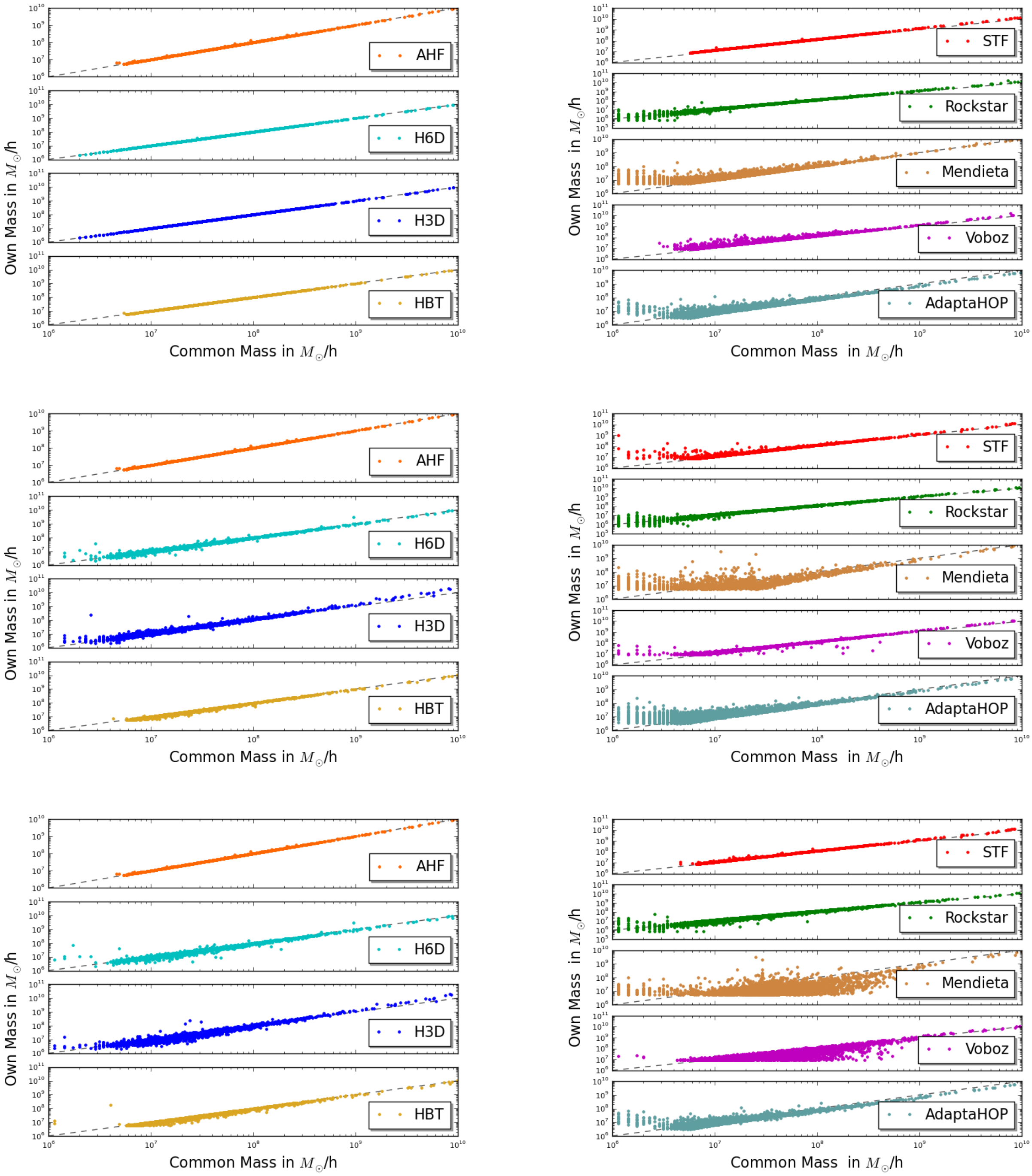

Figure 3.12: Mass from their own-analysis plotted against mass from the common-analysis for various halo finders. Top: subject to own-unbinding, Middle: subject to common unbinding, Bottom: subject to no-unbinding at the common-analysis.

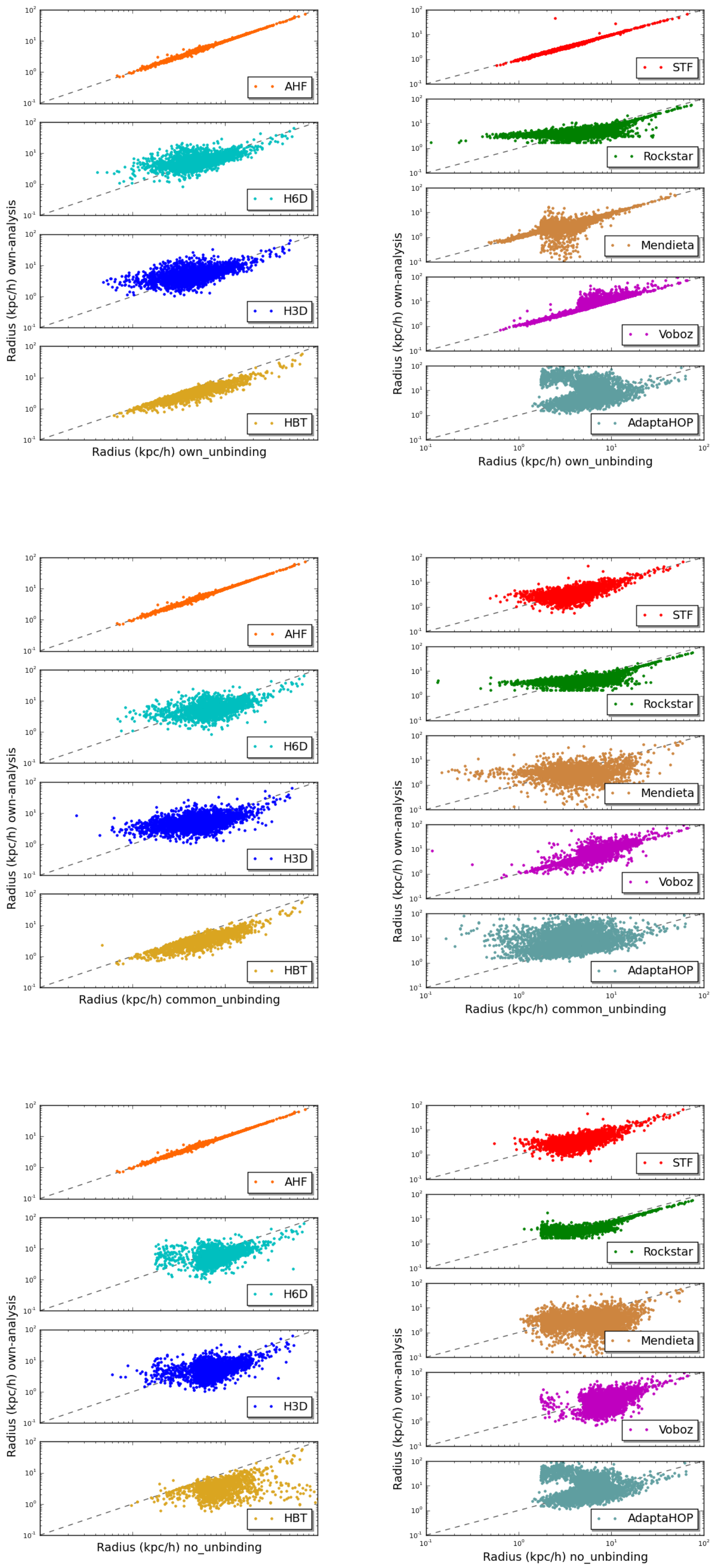

Figure 3.13: Radius from their own-analysis plotted against radius from the common-analysis for various halo finders. Top: subject to each finders own unbinding, Middle: subject to common-unbinding, Bottom: subject to no-unbinding at the common-analysis.

unbinding, the common-unbinding and no-unbinding respectively. ADAPTAHOP, H6D and H3D show no change because they do not have a functional unbinding routine. The scatter increases from own-unbinding (top-panel) to common-unbinding (middle-panel) for STF, VOBOZ and MENDIETA. The scatter further increases from own-unbinding (top-panel) to no-unbinding (bottom-panel) for VOBOZ and HBT finders. This comparison from unbinding-on (own-unbinding, top-panel) to unbinding-off (no-unbinding, bottom-panel) suggests that that own-unbinding option has least scatter. This again corroborates the use of own-unbinding data in the common-analysis project Onions et al. (2013).

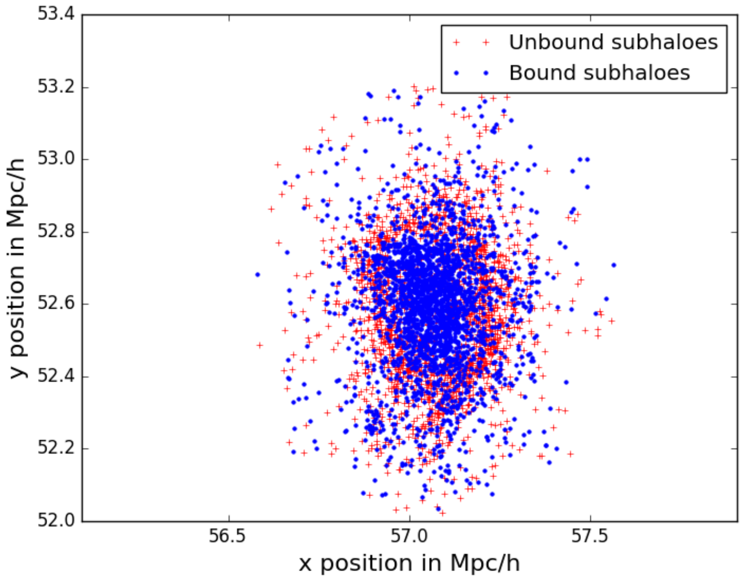

Figure 3.14: Subhaloes of a Milky Way sized halo in the Aquarius simulation (Aq-A-4) identified using the HBT halo-finder. Red points are unbound subhaloes and blue points are bound subhaloes. More unbound subhaloes are seen at the outer regions of the halo.

3.4.1 Spurious subhaloes

Spurious subhaloes are substructures gravitationally unbound to the host halo, however is still included as part of the host halo. In other words, these structures are also referred as 'false positives'. This section discusses the contribution of spurious subhaloes to the mass scatter. The option to unbind and the choice of halo finder influence the spurious subhalo count. This study investigates two unbinding options, own-unbinding and no-unbinding in the common-analysis and shows the presence of spurious subhaloes. The no-unbinding data has unbinding turned off and the own-unbinding data has unbinding turned on. By comparing the data from own-unbinding to no-unbinding, the spurious count can be deduced.

Firstly, the subhaloes from HBT halofinder were analysed by plotting their spatial centers as shown in the Figure 3.14, the unbound subhaloes are shown in red and the bound subhaloes are shown in blue. Unbound subhaloes are distributed on the edges of the halo, resulting in the formation of a ring-like structure (in red). Figure 3.15 shows a histogram, with the first and second columns showing the subhalo count for bound (in blue) and unbound subhaloes (in red) for the two resolutions, 20 and 200 particles per subhalo respectively. The plot on the top right shows unbound subhaloes distributed beyond 150kpc and peaks around 200kpc. The radial distribution of the subhaloes suggests that the unbound subhaloes are spread on the outskirts. The plots in the second row show cumulative fractions (cumulative from left to the right) for unbound and bound subhaloes in red and blue respectively. The plots in the third row show the cumulative number count of the unbound subhaloes increased from 14 (left) to 1923 (right) as the resolution was changed from 200 to 20 particles per subhalo. The fraction of unbound subhaloes increased from less than 1% in the left plot to around 40% in the right plot. The study showed that most of the unbound subhaloes were distributed on the low mass end.

Secondly, Figure 3.16 shows the mass and size distributions for SUBFIND, ROCKSTAR, H3D and AHF with the plots in first row showing the cumulative mass functions, and the bottom plot showing the fractions for two different resolutions (particles per subhalo) 200 and 20 respectively. The histograms and fractions are cumulative from high-mass-end towards low-mass-end with blue representing the bound and red representing the unbound subhaloes. The unbound subhalo count rises sharply at the low-mass end for all the finders with the exception of AHF that showed a steady count at low mass end. ROCKSTAR, a 6D finder, showed negligible count of unbound subhaloes mostly on the low-mass end and no count at high mass end. This also indicates that the option to unbind have very little affect on phase-space finders, due to their intrinsic velocity information. While H3D showed more than 50% of its haloes as unbound, AHF showed more than 80% as unbound. SUBFIND recorded 90% of its haloes as unbound and shows a sharp rise

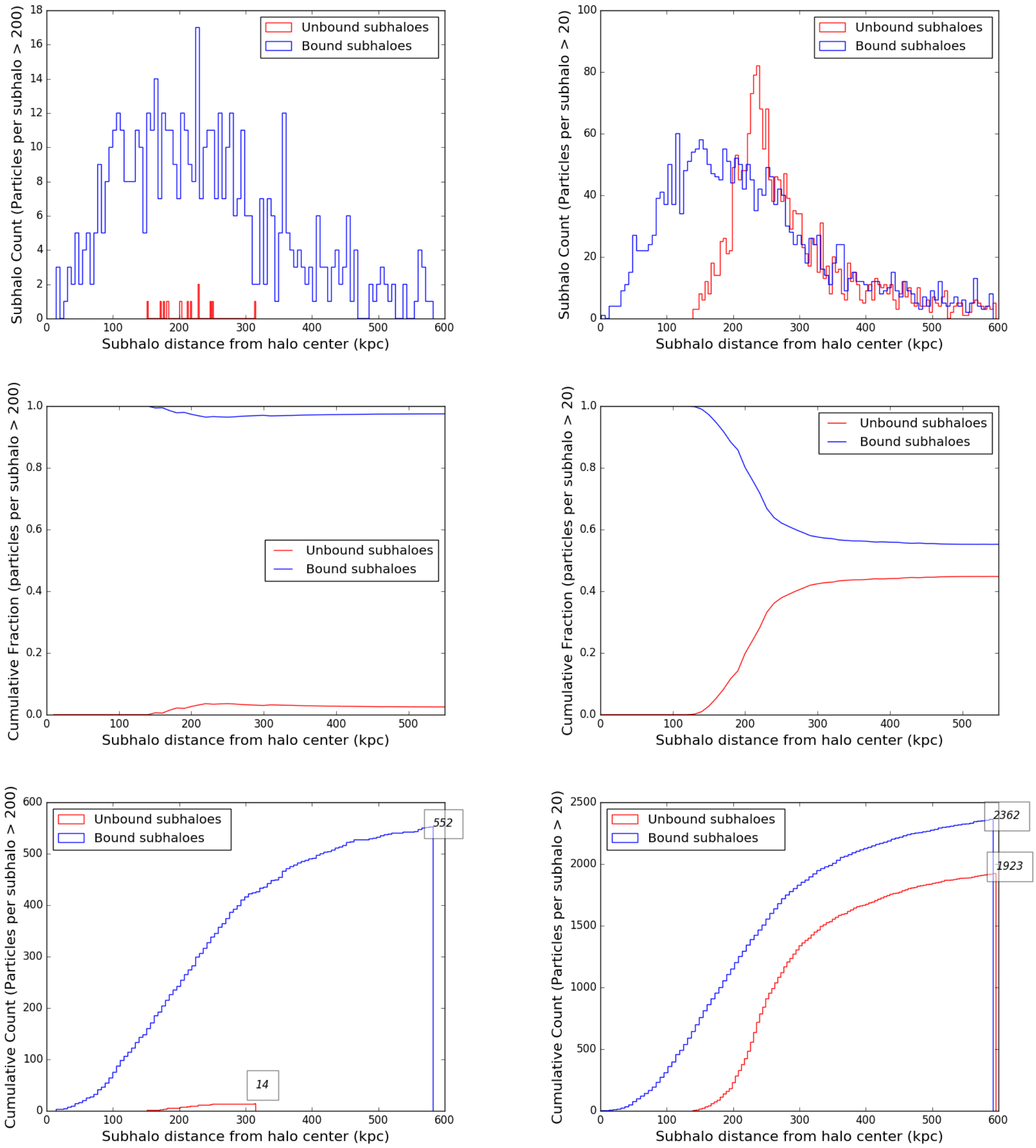

Figure 3.15: Distributions and fractions of bound (in blue) and unbound (in red) subhaloes in HBT halo-finder common-analysis. Left and right columns show subhaloes with more than 200 and 20 particles per subhalo respectively. The top row shows histogram showing the number count of subhaloes versus radial distance of the subhalo from the halo centre. The middle row shows the fraction subhalo number count, from centre radially outwards. Similarly, the bottom row shows the cumulative number of subhaloes, from the centre radially outwards.

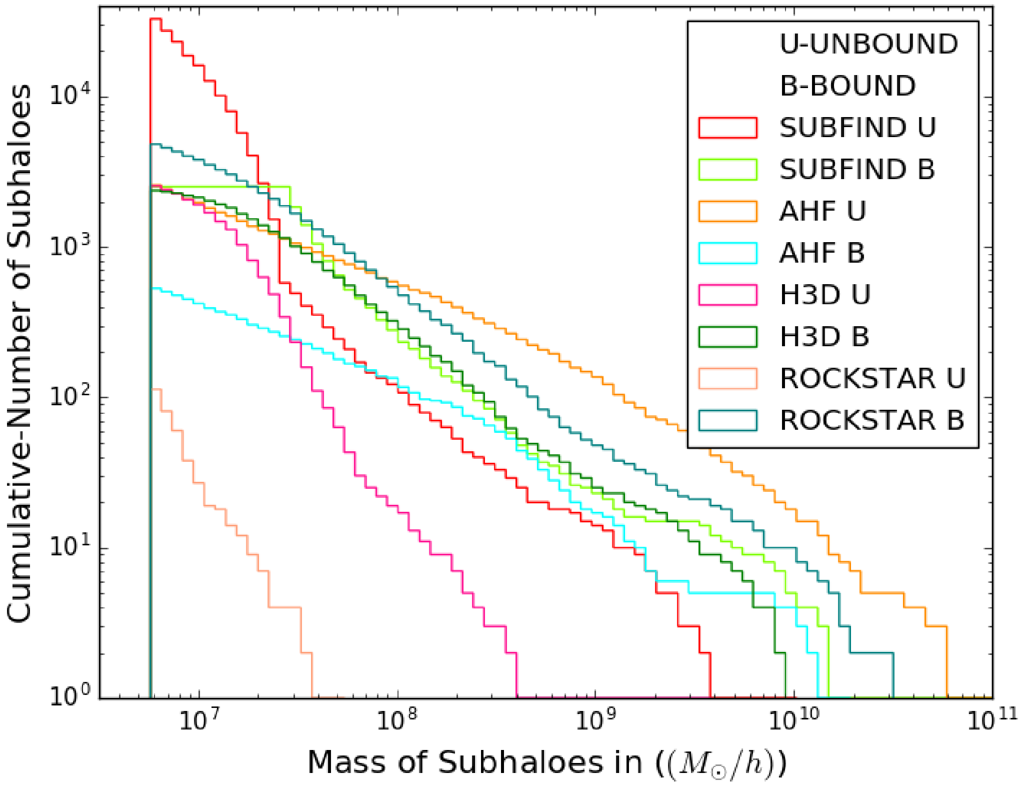

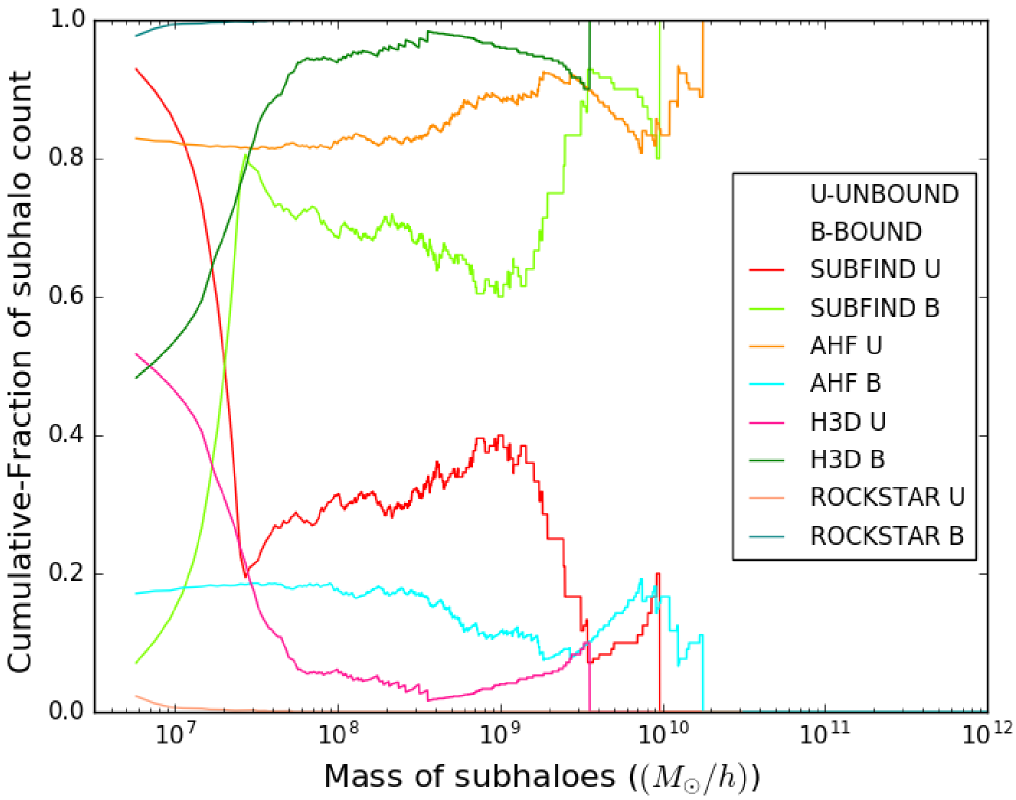

Figure 3.16: Cumulative number count (top plot) of subhaloes with bound and unbound fractions (bottom plot), both plotted against the mass of subhaloes for SUBFIND, AHF, H3D and ROCKSTAR halo-finders at a resolution of 20 particles per subhalo.

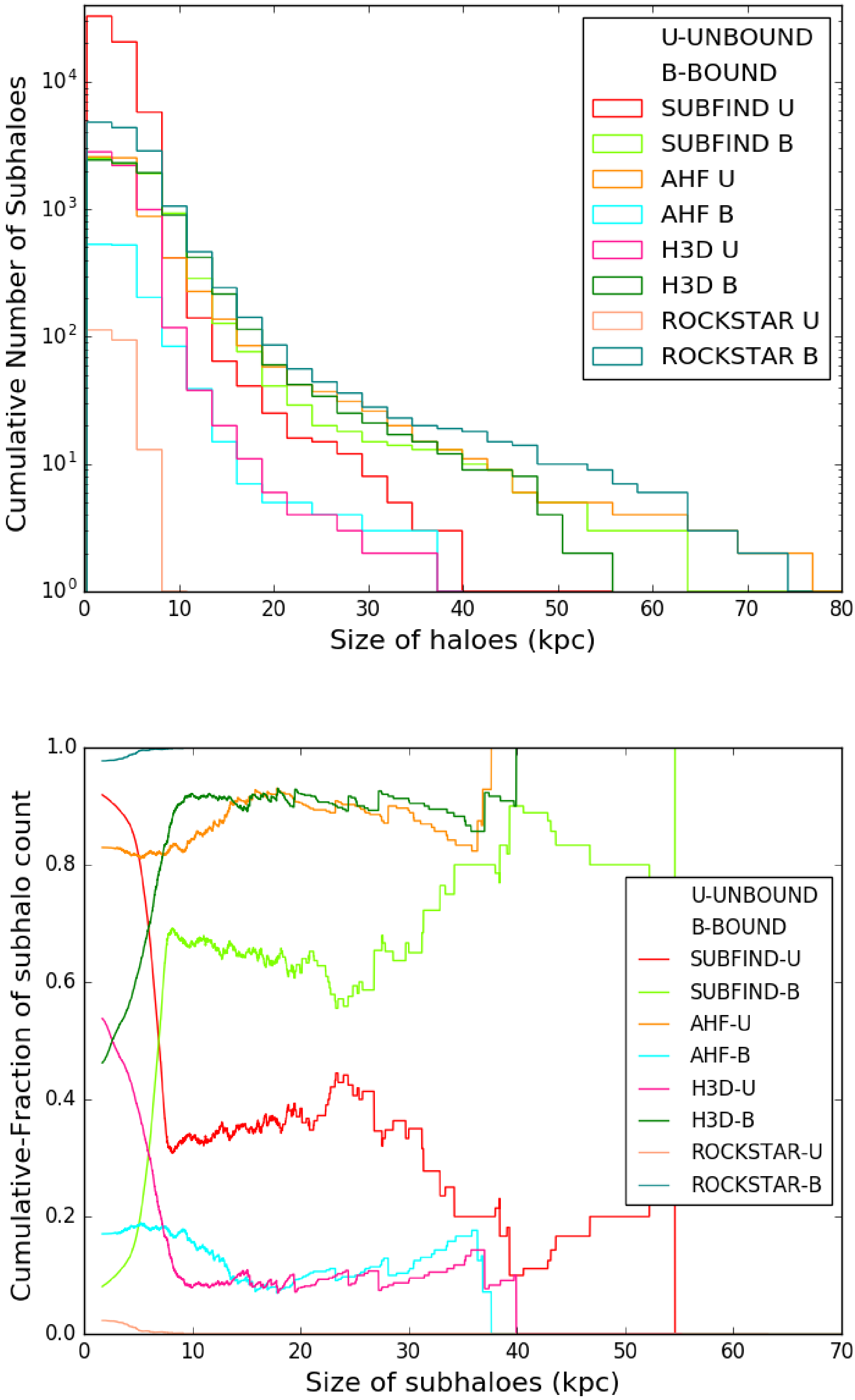

Figure 3.17: Cumulative number count (top plot) of subhaloes with bound and unbound fractions (bottom plot), both plotted against the size of subhaloes for SUBFIND, AHF, H3D, ROCKSTAR halo-finders at a resolution of 20 particles per subhalo.

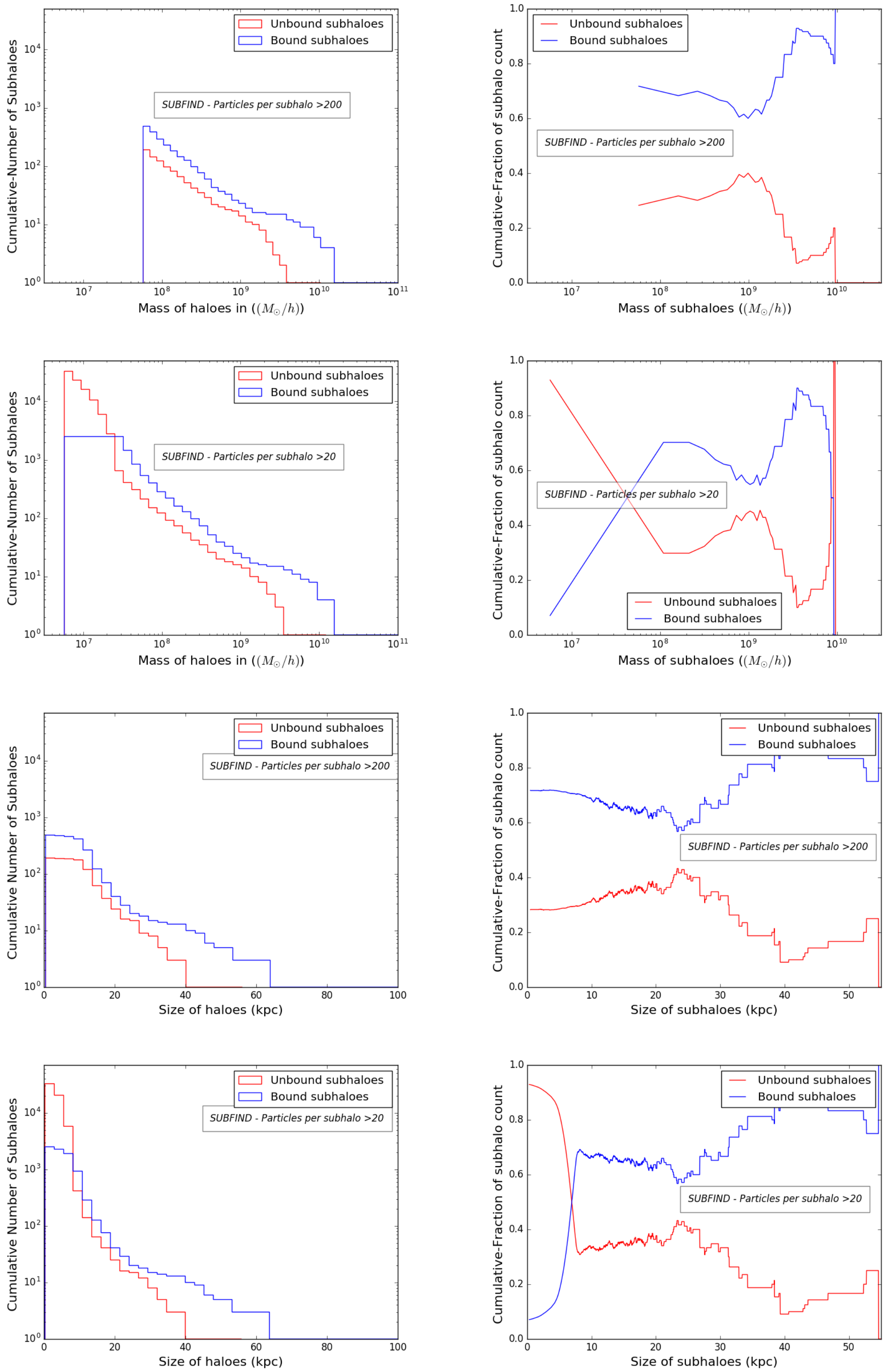

Figure 3.18: Distributions and fractions of bound (in blue) and unbound (in red) subhaloes in the SUBFIND halo-finder common-analysis. The first column and second column shows cumulative histogram and fractions respectively. The first and second row shows subhaloes plotted against mass with minimum of 20 and 200 particles per subhalo respectively. Similarly, the last two rows shows subhaloes plotted against the size of subhaloes.

in the unbound count towards the low mass end. AHF shows a cumulative unbound fraction of 80% consistently across all mass ranges. All configuration space finders SUBFIND, H3D and AHF show unbound fraction above 50% towards the low mass end, therefore suggesting the necessity of unbinding for configuration space finders. This also indicated that the astrophysical applications using low mass subhaloes are more affected. Comparing the configuration finders, on the low mass end, H3D performed better unbinding than AHF (80%), and AHF better than SUBFIND (90%). On the high mass end, SUBFIND (20%) was more efficient than AHF (80%). This showed that the choice of halo finder does affect the mass and size of subhaloes.

Figure 3.17 shows size of subhaloes at a resolution of 20 particles per subhalo. The histograms and fractions are cumulative from high size end towards low size end. The results from the size comparison show a very similar trend to mass comparison and therefore similar conclusions can be drawn. The unbound subhaloes are distributed predominantly on the low-size-end. ROCKSTAR stands out with the least unbound count, suggesting the advantage of using a phase-space finder. Again, all configuration space finders SUBFIND, H3D and AHF show unbound fraction above 50% towards the low size end, therefore suggesting that configuration space finders suffer from the contamination of spurious subhaloes. The 'unbinding' procedure is therefore essential and more so. Further subsections discuss the impact of unbinding for configuration space finders in more detail.

Figure 3.18 shows the cumulative histogram (first column), of bound and unbound fractions (second column) for the SUBFIND halo-finder. The upper two rows show distributions against the mass and the lower two rows (third and fourth) show distributions against the size. The analysis is run for two sets of resolutions 20 particles per subhalo in first and third rows, 200 particles per subhalo in second and last row. The plots on the left (first and second rows), show that as the resolution was increased from 200 to 20 particles per subhalo the number of unbound subhaloes increases by more than a factor of 100, indicating that most of the unbound subhaloes are on the low mass end. The plots on the right (first and second rows), show that as the resolution was increased from 200 to 20 particles per subhalo, the fraction of unbound subhaloes increased from 30% to 80% or more, again , indicating that most of the unbound subhaloes are on the low mass end, and astrophysical applications using low mass subhaloes are more affected and have to be aware of it. Similar trend is observed when plotted against the sizes (third and last rows).

Figures 3.19, 3.20, 3.21 show cumulative histogram and fractions for H3D, ROCKSTAR and AHF halo-finders respectively, for two resolutions, 50 and 20 particles per subhalo. The upper two rows show distributions against mass and the lower two rows show distributions against the size of subhaloes. The plots in the first and third row show subhaloes with a minimum resolution of 50 particles per subhalo. The plots in the second and last row show subhaloes with a minimum resolution of 20 particles per subhalo. In Figure 3.19, the plot on the right in the first row shows the fraction of unbound subhaloes to be 40% at a resolution of 50 particles per subhalo. As the resolution was increased from 50 to 20 particles per subhalo, the fraction of unbound subhaloes increases beyond 50%. The same trend repeated for size as seen in plot showing fractions in third and fourth rows. Astrophysical applications which account for low mass subhaloes are more affected and have to be more careful. Figure 3.20 shows negligible number of unbound subhaloes only on very small scales. As the resolution increases from 50 to 20 particles per subhalo, the fraction of unbound subhaloes increased to 3%. As ROCKSTAR is a phase-space halo-finder, the intrinsic velocity information helps removing the unbound particles or group, suggesting the advantage of using a phase-space finder over configuration space finders. In Figure 3.21, the fraction of unbound subhaloes was stable at 80% for both resolutions of 50 and 20 particles per subhalo indicating the presence of unbound subhaloes on all scales. Comparing the configuration finders, on the low mass end, H3D performed better unbinding than AHF (80% unbound), and AHF better than SUBFIND (90% unbound). On the high mass end, SUBFIND (20% unbound) was more efficient than AHF (80% unbound). This showed that the choice of halo finder does affect the mass and size of subhaloes.

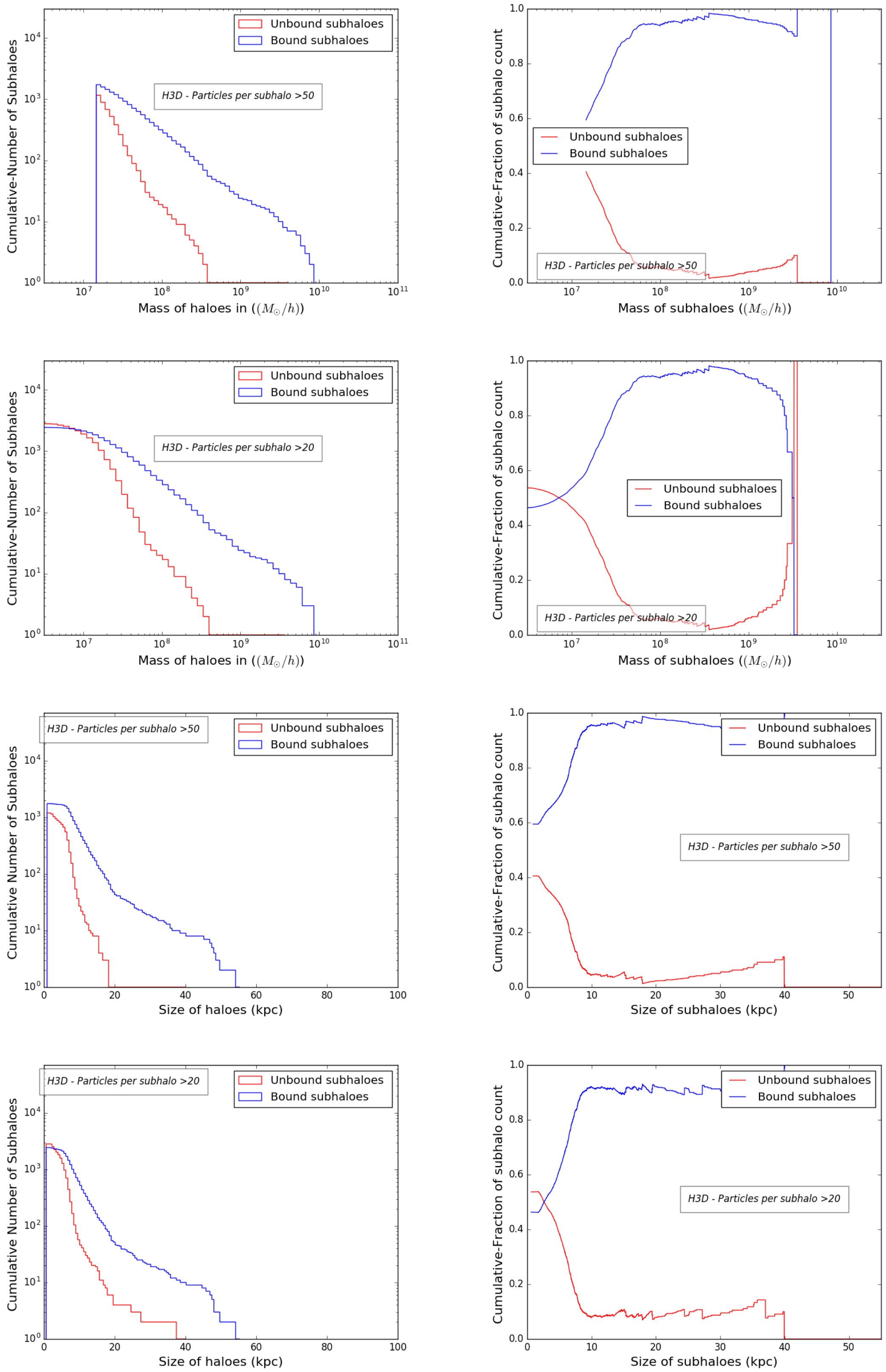

Figure 3.19: Distributions and fractions of bound (in blue) and unbound (in red) subhaloes in H3D halo-finder in common-analysis. The first column and second column shows cumulative histogram and fractions respectively. The first and second row shows subhaloes plotted against mass with minimum of 20 and 50 particles per subhalo respectively. Similarly, the last two rows shows subhaloes plotted against the size of subhaloes.

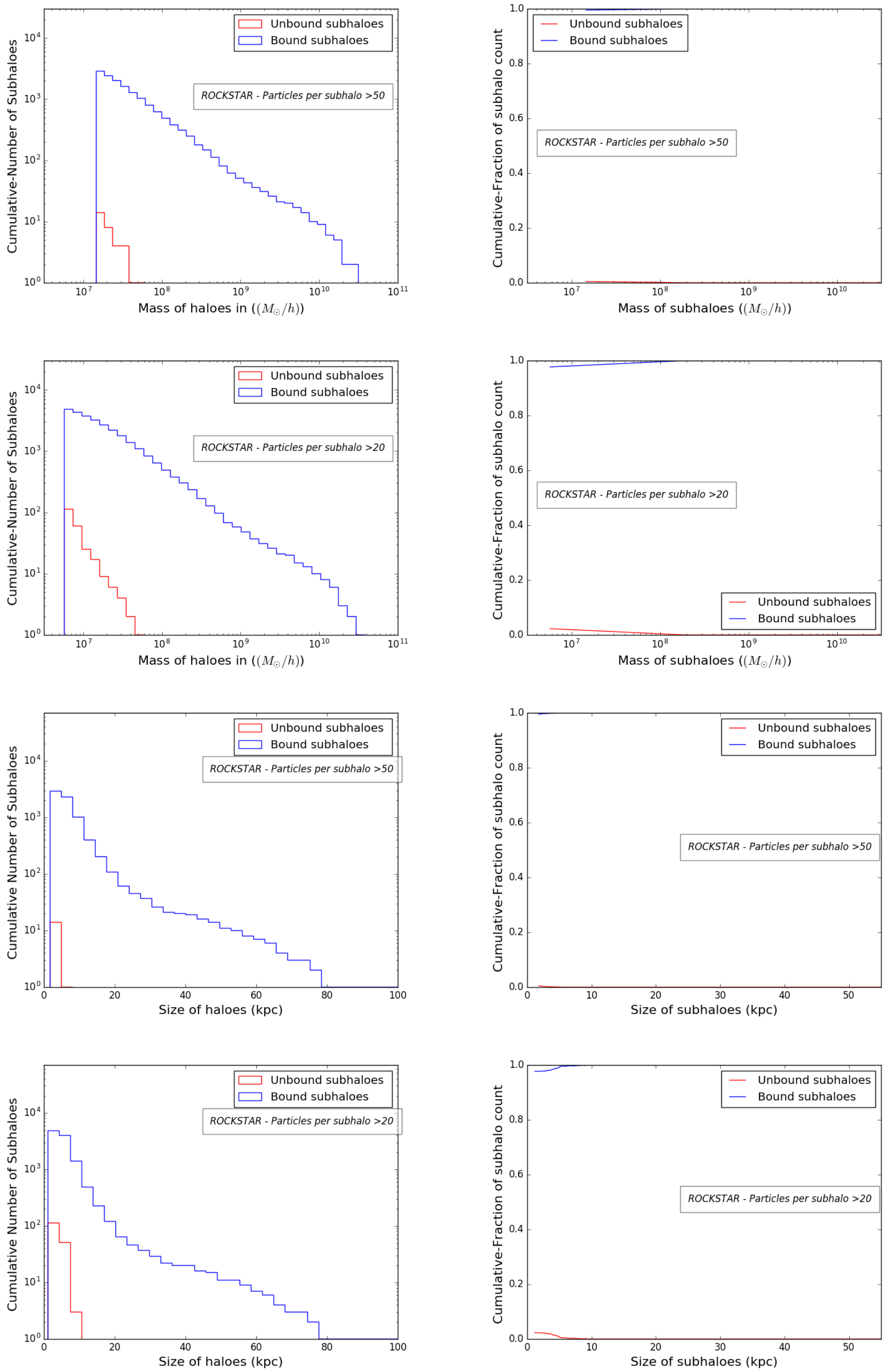

Figure 3.20: Distributions and fractions of bound (in blue) and unbound (in red) subhaloes in ROCKSTAR halo-finder in common-analysis. The first column and second column shows cumulative histogram and fractions respectively. The first and second row shows subhaloes plotted against mass with minimum of 20 and 50 particles per subhalo respectively. Similarly, the last two rows shows subhaloes plotted against the size of subhaloes.

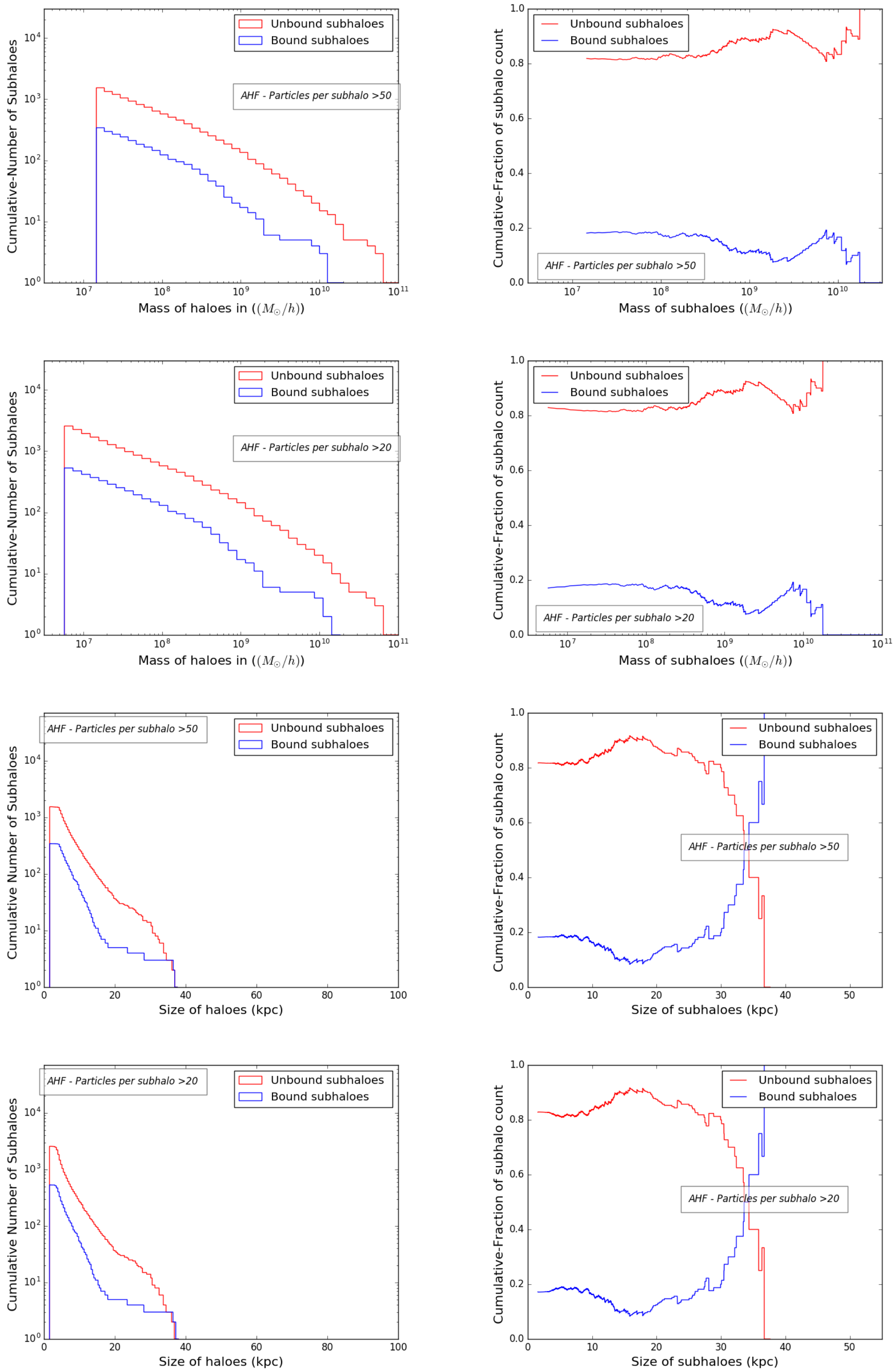

Figure 3.21: Distributions and fractions of bound (in blue) and unbound (in red) subhaloes in AHF halo-finder in common-analysis. The first column and second column shows cumulative histogram and fractions respectively. The first and second row shows subhaloes plotted against mass with minimum of 20 and 50 particles per subhalo respectively. Similarly, the last two rows shows subhaloes plotted against size of subhaloes

Chapter 4

Conclusions

The accuracy of halo-finding has increasingly become important as many astrophysical applications such as semi-analytical models, gravitational lensing, large scale structure surveys, streams, modified-gravity models, dark-matter detection models, near-field cosmology, etc are dependent on it. This project looks into the accuracy of various halofinders in recovering subhalo properties such as mass and size and investigates the method sources such as unbinding that cause the scatter. This is achieved by analyzing and comparing two sets of data, 'common-analysis' and 'own-analysis'. The 'common-analysis', is a common post-processing pipeline executed on Aquarius simulation data. The common post-processing pipeline comprises of common methods for halo centering, unbinding and determining the basic attributes for all participating finders. The "own-analysis" is the individual analysis of each halofinder themselves, run on the same simulation data. The need for the two analyses arises as the halo objects identified by these halofinders cannot be compared directly across the finders. With the common-analysis, the halo objects can be matched across finders. The data for this project is sourced from a Milky Way sized halo in Aquarius simulation. This work is explored on three major areas. (1) Mass comparison, (2) Size comparison, and (3) Unbinding.

Firstly, the own-analysis showed a scatter of 20% in the subhalo mass as against 10% scatter in the common-analysis. Unlike common-analysis, a benchmark analysis which is not used by any astrophysical applications or models, the own-analysis is widely used by several astrophysical applications. With a scatter of 20% in the halofinder's own-analysis, which is a factor of two times higher as compared to common-analysis, it is of paramount importance to investigate the reasons for the scatter and constrain them. The subhalo catalogs were matched between the common-analysis and the own-analysis for all the participating halofinders (AHF, SUBFIND, ROCKSTAR, VOBOZ, HBT, ADAPTAHOP, MENDIETA, H3D, H6D, HSF and STF) based on the halo identifications. Sample haloes were identified through extensive eyeball checking and investigated for traits such as missing substructures, center offsets and artifacts. Several samples from AHF, VOBOZ, HBT, ADAPTAHOP and MENDIETA showed missing substructures. Samples from MENDIETA showed simulation artifacts. The mass comparison in VOBOZ suggested that the different virial mass definitions lead to different subhalo masses. Using the cumulative mass functions (for exclusive and inclusive masses) for ROCKSTAR and ADAPTAHOP, the study showed the choice to include or exclude substructures, leads to 10% scatter in the mass. As substructures amount to 10% of a halo, their inclusion alters the subhalo mass by this amount. The act of including or excluding therefore contributes to the mass scatter, and the end user using the halo catalogues is advised to be cautious.

Secondly, across all the finders, size of haloes was compared mainly on two parameters, density and size. As mass, size and density are related in theory, size can be derived from mass (provided the density remains constant), and the mass of a halo is usually calculated as the total mass of the constituent particles. The size comparison lists the following important results. (a) The size-density comparison in ROCKSTAR suggested that the density indeed remained constant for all the haloes and hence the size of a halo was derived from mass. The rest of the halo finders showed scatter in the density suggesting that the size was not directly derived from mass, but from other possible definitions such as "distance to the farthest bound particle" or 'virial radius', as in the case of AHF. (b) VOBOZ showed that the scatter in the size was due to different virial mass definitions. (e) AHF finder showed that the two definitions for size, lead to two sets of subhalo sizes suggesting that subhalo sizes read from halo catalogues cannot be trusted.

Lastly, the study investigated the distributions of the unbound subhaloes in selected finders and the results are as follows. (a) Three unbinding options were explored and compared. The data for the three options were available in the common-analysis project. 'own-unbinding'- unbinding was executed at individual finder level, 'common-unbinding'- unbinding was executed in common-analysis, 'No-unbinding' - no unbinding at the individual finder level and no unbinding in the common-analysis. Halo finders STF, VOBOZ and MENDIETA showed scatter (in mass and size) that increased from own-unbinding to common-unbinding, and VOBOZ and HBT showed further increase in the scatter from common-unbinding to no-unbinding options. The comparison suggested that that own-unbinding option had the least scatter (in mass and size) and this explains the reason for choosing the own-unbinding option in the common-analysis project Onions et al. (2013) (literature version). (b) Most of the spurious (unbound) subhaloes were found towards the edges, spread on the outskirts of the halo. This was illustrated with HBT finder that showed spurious subhaloes that peaked beyond 200kpc of the halo centre. This study also showed that most of the spurious subhaloes were distributed on the low mass end. (c) ROCKSTAR showed very little unbinding (5% of particles unbound) at a resolution of 20 particles, suggesting that the option to unbind had very little impact on phase-space finders. This also indicates that the phase-space finders demonstrated better accuracy in constraining the mass than the configuration-space finders. (d) All configuration-space finders (SUBFIND, H3D and AHF) showed spurious (unbound subhaloes) fraction above 50% suggesting that an unbinding procedure is essential for configuration-space finders. Most of the spurious subhaloes were distributed on the low mass end indicating that the astrophysical applications using the low mass subhaloes need to be cautious. While H3D showed 50% of its haloes as spurious, AHF showed 80% and SUBFIND recorded 90% of its haloes as spurious. This suggested that, H3D performed better unbinding than AHF and AHF better than SUBFIND. In summary, the choice of unbinding and the choice of halo finder did affect the mass and size of subhaloes and hence contributed to their scatter.

Finally, the results from this study would hope to caution and guide the users on what to expect from a halofinder and to choose the right halo finder that suits their application. Applications such as the gravitational lensing requires complete mass and therefore a halo finder that includes substructures is recommended, whereas mass profile investigations would require a halo finder such as SUBFIND that excludes substructures. Configuration-space finders include spurious particles (false positives) as they do not have velocity information and therefore the end-users are strongly recommended to run unbinding procedures provided by the respective finders, unless the application wants to include particles that are unbound (e.g. Tidal relics, Streams, X-ray properties, Sachs-Wolfe effect, Sunyaev-Zeldovich eect, Gravitaional lensing). Finders such as ADAPTOHOP, H3D and H6D do not have a built in unbinding routine and therefore applications using them have to be cautious. In other words, configuration-space finder along with an unbinding procedure works as a pseudo-phase-space finder. Phase-space finders such as ROCKSTAR, H6D, HSF is recommended for applications involving dynamical analysis such as mergers, flybys, etc. STF is recommended for diffused streams and tidal remnants. ROCKSTAR and HBT is best suited for temporal applications involving tracking structures.

Bibliography

Aarseth, S. J. Dynamical evolution of clusters of galaxies, I. , 126:223, 1963. 17

Anderhalden, D. and Diemand, J. The total mass of dark matter haloes. , 414: 3166–3172, July 2011. doi: 10.1111/j.1365-2966.2011.18614.x. 32

Aragón-Calvo, M. A., van de Weygaert, R., Jones, B. J. T., and van der Hulst, J. M. Spin Alignment of Dark Matter Halos in Filaments and Walls. , 655:L5–L8, January 2007. doi: 10.1086/511633. 24

Ascasibar, Y. Estimating multidimensional probability fields using the Field Estimator for Arbitrary Spaces (FiEstAS) with applications to astrophysics. *Computer Physics Communications*, 181:1438–1443, August 2010. doi: 10.1016/j.cpc.2010.04.011. 24

Ascasibar, Y. and Binney, J. Numerical estimation of densities. *mnras*, 356:872–882, January 2005. doi: 10.1111/j.1365-2966.2004.08480.x. 30, 34, 38, 48

Avila, S., Knebe, A., Pearce, F. R., Schneider, A., Srisawat, C., Thomas, P. A., Behroozi, P., Elahi, P. J., Han, J., Mao, Y.-Y., Onions, J., Rodriguez-Gomez, V., and Tweed, D. SUSSING MERGER TREES: the influence of the halo finder. , 441:3488–3501, July 2014. doi: 10.1093/mnras/stu799. 46

Bagla, J. S. TreePM: A Code for Cosmological N-Body Simulations. *Journal of Astrophysics and Astronomy*, 23:185–196, December 2002. doi: 10.1007/BF02702282. 19

Bagla, J. S. and Ray, S. Performance characteristics of TreePM codes. , 8:665–677, September 2003. doi: 10.1016/S1384-1076(03)00056-3. 19

Baldi, M. The CoDECS project: a publicly available suite of cosmological N-body simulations for interacting dark energy models. , 422:1028–1044, May 2012. doi: 10.1111/j.1365-2966.2012.20675.x. 26

Barnes, J. and Hut, P. A hierarchical O(N log N) force-calculation algorithm. , 324: 446–449, December 1986. doi: 10.1038/324446a0. 19

Bartelmann, M. and Schneider, P. Weak gravitational lensing. , 340:291–472, January 2001. doi: 10.1016/S0370-1573(00)00082-X. 25

Baugh, C. M. A primer on hierarchical galaxy formation: the semi-analytical approach. *Reports on Progress in Physics*, 69:3101–3156, December 2006. doi: 10.1088/0034-4885/69/12/R02. 14

Behroozi, P., Wechsler, R., and Wu, H.-Y. Rockstar: Phase-space halo finder. October 2012. 30, 34, 36, 42, 48

Behroozi, P., Knebe, A., Pearce, F. R., Elahi, P., Han, J., Lux, H., Mao, Y.-Y., Muldrew, S. I., Potter, D., and Srisawat, C. Major Mergers Going Notts: Challenges for Modern Halo Finders. *ArXiv e-prints*, June 2015. 12

Behroozi, P. S., Wechsler, R. H., and Wu, H.-Y. The ROCKSTAR Phase-space Temporal Halo Finder and the Velocity Offsets of Cluster Cores. , 762:109, January 2013. doi: 10.1088/0004-637X/762/2/109. 36

Bennert, V. N., Auger, M. W., Treu, T., Woo, J.-H., and Malkan, M. A. The Relation between Black Hole Mass and Host Spheroid Stellar Mass Out to z ˜ 2. , 742:107, December 2011. doi: 10.1088/0004-637X/742/2/107. 109

Benson, A. J. G ALACTICUS: A semi-analytic model of galaxy formation. , 17: 175–197, February 2012. doi: 10.1016/j.newast.2011.07.004. 12, 31, 105

Benson, A. J., Cole, S., Frenk, C. S., Baugh, C. M., and Lacey, C. G. The nature of galaxy bias and clustering. , 311:793–808, February 2000. doi: 10.1046/j.1365-8711.2000.03101.x. 106

Benson, A. J., Ellis, R. S., and Menanteau, F. On the continuous formation of field spheroidal galaxies in hierarchical models of structure formation. *mnras*, 336: 564–576, October 2002. doi: 10.1046/j.1365-8711.2002.05774.x. 12, 24

Benson, A. J., Bower, R. G., Frenk, C. S., Lacey, C. G., Baugh, C. M., and Cole, S. What Shapes the Luminosity Function of Galaxies? , 599:38–49, December 2003. doi: 10.1086/379160. 109

Berlind, A. A. and Weinberg, D. H. The Halo Occupation Distribution: Toward an Empirical Determination of the Relation between Galaxies and Mass. , 575: 587–616, August 2002. doi: 10.1086/341469. 106

Bertone, S., De Lucia, G., and Thomas, P. A. The recycling of gas and metals in galaxy formation: predictions of a dynamical feedback model. *mnras*, 379: 1143–1154, August 2007. doi: 10.1111/j.1365-2966.2007.11997.x. 12, 24

Bhattacharya, S., Heitmann, K., White, M., Lukić, Z., Wagner, C., and Habib, S. Mass Function Predictions Beyond ΛCDM. , 732:122, May 2011. doi: 10.1088/0004-637X/732/2/122. 12, 25

Blanchet, S. and Lavalle, J. Diffuse gamma-ray constraints on dark matter revisited I: the impact of subhalos. , 11:021, November 2012. doi: 10.1088/1475-7516/2012/11/021. 26

Blumenthal, G. R., Faber, S. M., Flores, R., and Primack, J. R. Contraction of dark matter galactic halos due to baryonic infall. , 301:27–34, February 1986. doi: 10.1086/163867. 109

Bode, P., Ostriker, J. P., and Xu, G. The Tree Particle-Mesh N-Body Gravity Solver. , 128:561–569, June 2000. doi: 10.1086/313398. 19

Bower, R. G., Benson, A. J., Malbon, R., Helly, J. C., Frenk, C. S., Baugh, C. M., Cole, S., and Lacey, C. G. Breaking the hierarchy of galaxy formation. , 370: 645–655, August 2006. doi: 10.1111/j.1365-2966.2006.10519.x. 12, 23, 24, 108, 109

Bower, R. G., Vernon, I., Goldstein, M., Benson, A. J., Lacey, C. G., Baugh, C. M., Cole, S., and Frenk, C. S. The parameter space of galaxy formation. , 407: 2017–2045, October 2010. doi: 10.1111/j.1365-2966.2010.16991.x. 23, 105

Boylan-Kolchin, M., Bullock, J. S., and Kaplinghat, M. Too big to fail? The puzzling darkness of massive Milky Way subhaloes. , 415:L40–L44, July 2011. doi: 10.1111/j.1745-3933.2011.01074.x. 109

Brooks, A. M. and Zolotov, A. Why Baryons Matter: The Kinematics of Dwarf Spheroidal Satellites. , 786:87, May 2014. doi: 10.1088/0004-637X/786/2/87. 109

Bryan, G. L. and Norman, M. L. Statistical Properties of X-Ray Clusters: Analytic and Numerical Comparisons. , 495:80–99, March 1998. doi: 10.1086/305262. 29

Bullock, J. S. Notes on the Missing Satellites Problem. *ArXiv e-prints*, September 2010. 110

Burkert, A. The Structure and Evolution of Weakly Self-interacting Cold Dark Matter Halos. , 534:L143–L146, May 2000. doi: 10.1086/312674. 108

Carlesi, E., Knebe, A., Yepes, G., Gottlöber, S., Jiménez, J. B., and Maroto, A. L. Vector dark energy and high-z massive clusters. , 418:2715–2719, December 2011. doi: 10.1111/j.1365-2966.2011.19660.x. 26

Carollo, D., Beers, T. C., Lee, Y. S., Chiba, M., Norris, J. E., Wilhelm, R., Sivarani, T., Marsteller, B., Munn, J. A., Bailer-Jones, C. A. L., Fiorentin, P. R., and York, D. G. Two stellar components in the halo of the Milky Way. , 450:1020–1025, December 2007. doi: 10.1038/nature06460. 24

Chan, T. K., Kereš, D., Oñorbe, J., Hopkins, P. F., Muratov, A. L., Faucher-Giguère, C.-A., and Quataert, E. The impact of baryonic physics on the structure of dark matter haloes: the view from the FIRE cosmological simulations. , 454: 2981–3001, December 2015. doi: 10.1093/mnras/stv2165. 11, 13

Cole, S. and Lacey, C. The structure of dark matter haloes in hierarchical clustering models. , 281:716, July 1996. doi: 10.1093/mnras/281.2.716. 24

Cole, S., Lacey, C. G., Baugh, C. M., and Frenk, C. S. Hierarchical galaxy formation. , 319:168–204, November 2000. doi: 10.1046/j.1365-8711.2000.03879.x. 12, 23, 24

Coles, P. Large-Scale Structure. In van Haarlem, M. P., editor, *Perspectives on Radio Astronomy: Science with Large Antenna Arrays*, page 53, 2000. 14

Colombi, S. AdaptaHOP: Subclump finder. May 2013. 30, 34, 38, 48

Conroy, C., Wechsler, R. H., and Kravtsov, A. V. Modeling Luminosity-dependent Galaxy Clustering through Cosmic Time. , 647:201–214, August 2006. doi: 10.1086/503602. 106, 110

Cooper, A. P., Cole, S., Frenk, C. S., White, S. D. M., Helly, J., Benson, A. J., De Lucia, G., Helmi, A., Jenkins, A., Navarro, J. F., Springel, V., and Wang, J. Galactic stellar haloes in the CDM model. , 406:744–766, August 2010. doi: 10.1111/j.1365-2966.2010.16740.x. 25

Couchman, H. M. P. Mesh-refined P3M - A fast adaptive N-body algorithm. , 368: L23–L26, February 1991. doi: 10.1086/185939. 19

Couchman, H. M. P., Thomas, P. A., and Pearce, F. R. Hydra: an Adaptive-Mesh Implementation of P 3M-SPH. , 452:797, October 1995. doi: 10.1086/176348. 104

Courtin, J., Rasera, Y., Alimi, J.-M., Corasaniti, P.-S., Boucher, V., and Füzfa, A. Imprints of dark energy on cosmic structure formation - II. Non-universality of the halo mass function. , 410:1911–1931, January 2011. doi: 10.1111/j.1365-2966.2010.17573.x. 12, 24

Croton, D. J. Evolution in the black hole mass-bulge mass relation: a theoretical perspective. , 369:1808–1812, July 2006. doi: 10.1111/j.1365-2966.2006.10429.x. 12, 23, 24, 105, 108, 109

Cuesta, A. J. and Prada, F. The Mass of Virialized Dark Matter Haloes. In Kodama, T., Yamada, T., and Aoki, K., editors, *Panoramic Views of Galaxy Formation and Evolution*, volume 399 of *Astronomical Society of the Pacific Conference Series*, page 121, October 2008. 32

Davé, R., Spergel, D. N., Steinhardt, P. J., and Wandelt, B. D. Halo Properties in Cosmological Simulations of Self-interacting Cold Dark Matter. , 547:574–589, February 2001. doi: 10.1086/318417. 108

Davis, M. and Djorgovski, S. Galaxy clustering as a function of surface brightness. , 299:15–20, December 1985. doi: 10.1086/163678. 15, 27 de Blok, W. J. G., Walter, F., Brinks, E., Trachternach, C., Oh, S.-H., and Kennicutt, R. C., Jr. High-Resolution Rotation Curves and Galaxy Mass Models from THINGS. , 136:2648-2719, December 2008. doi: 10.1088/0004-6256/136/6/2648. 108

De Lucia, G. and Blaizot, J. The hierarchical formation of the brightest cluster galaxies. , 375:2–14, February 2007. doi: 10.1111/j.1365-2966.2006.11287.x. 23

De Lucia, G., Springel, V., White, S. D. M., Croton, D., and Kauffmann, G. The formation history of elliptical galaxies. *mnras*, 366:499–509, February 2006. doi: 10.1111/j.1365-2966.2005.09879.x. 12, 24

Dehnen, W. and Read, J. I. N-body simulations of gravitational dynamics. *European Physical Journal Plus*, 126:55, May 2011. doi: 10.1140/epjp/i2011-11055-3. 19

Del Popolo, A. The Cusp/Core Problem and the Secondary Infall Model. , 698: 2093–2113, June 2009. doi: 10.1088/0004-637X/698/2/2093. 109

Di Cintio, A., Brook, C. B., Macciò, A. V., Stinson, G. S., Knebe, A., Dutton, A. A., and Wadsley, J. The dependence of dark matter profiles on the stellar-to-halo mass ratio: a prediction for cusps versus cores. , 437:415–423, January 2014. doi: 10.1093/mnras/stt1891. 109

Diemand, J., Kuhlen, M., and Madau, P. Early Supersymmetric Cold Dark Matter Substructure. , 649:1–13, September 2006. doi: 10.1086/506377. 25

Diemand, J., Kuhlen, M., and Madau, P. Evolution of Dark Matter Subhalos. In *American Astronomical Society Meeting Abstracts #210*, volume 39 of *Bulletin of the American Astronomical Society*, page 144, May 2007. 110

Diemand, J., Kuhlen, M., Madau, P., Zemp, M., Moore, B., Potter, D., and Stadel, J. Clumps and streams in the local dark matter distribution. , 454:735–738, August 2008. doi: 10.1038/nature07153. 24

Duffy, A. R., Schaye, J., Kay, S. T., Dalla Vecchia, C., Battye, R. A., and Booth, C. M. Impact of baryon physics on dark matter structures: a detailed simulation study of halo density profiles. , 405:2161–2178, July 2010. doi: 10.1111/j.1365-2966.2010.16613.x. 11

Dunstan, R. M., Abazajian, K. N., Polisensky, E., and Ricotti, M. The Halo Model of Large Scale Structure for Warm Dark Matter. *ArXiv e-prints*, September 2011. 108

EAGLE-Project, P. Eagle (evolution and assembly of galaxies and their environments), Jan 2015. URL `http://icc.dur.ac.uk/Eagle/`. 17

Efstathiou, G. and Eastwood, J. W. On the clustering of particles in an expanding universe. , 194:503–525, February 1981. 18

Eke, V. R., Baugh, C. M., Cole, S., Frenk, C. S., Norberg, P., Peacock, J. A., Baldry, I. K., Bland-Hawthorn, J., Bridges, T., Cannon, R., Colless, M., Collins, C., Couch, W., Dalton, G., de Propris, R., Driver, S. P., Efstathiou, G., Ellis, R. S., Glazebrook, K., Jackson, C., Lahav, O., Lewis, I., Lumsden, S., Maddox, S., Madgwick, D., Peterson, B. A., Sutherland, W., and Taylor, K. Galaxy groups in the 2dFGRS: the group-finding algorithm and the 2PIGG catalogue. , 348:866–878, March 2004. doi: 10.1111/j.1365-2966.2004.07408.x. 27

El-Zant, A., Shlosman, I., and Hoffman, Y. Dark Halos: The Flattening of the Density Cusp by Dynamical Friction. , 560:636–643, October 2001. doi: 10.1086/322516. 109

Elahi, P. J. *Simulations of scale-free cosmologies for the small-scale cold dark matter universe*. PhD thesis, Queen's University (Canada, 2009. 26

Elahi, P. J., Thacker, R. J., and Widrow, L. M. Peaks above the Maxwellian Sea: a new approach to finding substructures in N-body haloes. *mnras*, 418:320–335, November 2011. doi: 10.1111/j.1365-2966.2011.19485.x. 12, 24, 30, 34, 38, 42, 48

Elbert, O. D., Bullock, J. S., Garrison-Kimmel, S., Rocha, M., Oñorbe, J., and Peter, A. H. G. Core formation in dwarf haloes with self-interacting dark matter: no fine-tuning necessary. , 453:29–37, October 2015. doi: 10.1093/mnras/stv1470. 108

Fairbairn, M. and Schwetz, T. Spin-independent elastic WIMP scattering and the DAMA annual modulation signal. , 1:037, January 2009. doi: 10.1088/1475-7516/2009/01/037. 24

Falck, B. L., Neyrinck, M. C., and Szalay, A. S. ORIGAMI: Delineating Halos Using Phase-space Folds. , 754:126, August 2012. doi: 10.1088/0004-637X/754/2/126. 12, 25

Ferrarese, L. and Merritt, D. A Fundamental Relation between Supermassive Black Holes and Their Host Galaxies. , 539:L9–L12, August 2000. doi: 10.1086/312838. 109

Flores, R. A. and Primack, J. R. Observational and theoretical constraints on singular dark matter halos. , 427:L1–L4, May 1994. doi: 10.1086/187350. 108

Font, A. S., Bower, R. G., McCarthy, I. G., Benson, A. J., Frenk, C. S., Helly, J. C., Lacey, C. G., Baugh, C. M., and Cole, S. The colours of satellite galaxies in groups and clusters. *mnras*, 389:1619–1629, October 2008. doi: 10.1111/j.1365-2966.2008.13698.x. 12, 23, 24

Frenk, C. Dark Matter and Structure Formation: Future Prospects. In Spooner, N. J. C. and Kudryavtsev, V., editors, *The Identification of Dark Matter*, page 51, 1999. 11

Frenk, C. S. and White, S. D. M. Dark matter and cosmic structure. *Annalen der Physik*, 524:507–534, October 2012. doi: 10.1002/andp.201200212. 11, 12, 15

Frenk, C. S., White, S. D. M., and Davis, M. Nonlinear evolution of large-scale structure in the universe. , 271:417–430, August 1983. doi: 10.1086/161209. 14

Fryxell, B., Olson, K., Ricker, P., Timmes, F. X., Zingale, M., Lamb, D. Q., MacNeice, P., Rosner, R., Truran, J. W., and Tufo, H. FLASH: An Adaptive Mesh Hydrodynamics Code for Modeling Astrophysical Thermonuclear Flashes. , 131: 273–334, November 2000. doi: 10.1086/317361. 103

Furlong, M., Bower, R. G., Theuns, T., Schaye, J., Crain, R. A., Schaller, M., Dalla Vecchia, C., Frenk, C. S., McCarthy, I. G., Helly, J., Jenkins, A., and Rosas-Guevara, Y. M. Evolution of galaxy stellar masses and star formation rates in the EAGLE simulations. *ArXiv e-prints*, October 2014. 16, 104

Furlong, M., Bower, R. G., Theuns, T., Schaye, J., Crain, R. A., Schaller, M., Dalla Vecchia, C., Frenk, C. S., McCarthy, I. G., Helly, J., Jenkins, A., and Rosas-Guevara, Y. M. Evolution of galaxy stellar masses and star formation rates in the EAGLE simulations. , 450:4486–4504, July 2015. doi: 10.1093/mnras/stv852. 11

Gao, L., Frenk, C. S., Jenkins, A., Springel, V., and White, S. D. M. Where will supersymmetric dark matter first be seen? , 419:1721–1726, January 2012. doi: 10.1111/j.1365-2966.2011.19836.x. 26

Garrison-Kimmel, S., Boylan-Kolchin, M., Bullock, J. S., and Kirby, E. N. Too big to fail in the Local Group. , 444:222–236, October 2014. doi: 10.1093/mnras/stu1477. 110

Gavazzi, R. Projection effects in cluster mass estimates: the case of MS2137-23. , 443:793–804, December 2005. doi: 10.1051/0004-6361:20053166. 25

Gentile, G., Klein, U., Salucci, P., and Vergani, D. Cores vs. Cusps: Dark Matter Density Profiles in Spirals. In Ryder, S., Pisano, D., Walker, M., and Freeman, K., editors, *Dark Matter in Galaxies*, volume 220 of *IAU Symposium*, page 311, July 2004. 108

Gill, S. P. D., Knebe, A., and Gibson, B. K. The dynamics of cluster substructure. In Diaferio, A., editor, *IAU Colloq. 195: Outskirts of Galaxy Clusters: Intense Life in the Suburbs*, pages 280–284, July 2004. doi: 10.1017/S1743921304000596. 31, 35

Giocoli, C., Tormen, G., and van den Bosch, F. C. The population of dark matter subhaloes: mass functions and average mass-loss rates. , 386:2135–2144, June 2008. doi: 10.1111/j.1365-2966.2008.13182.x. 31

Giocoli, C., Tormen, G., Sheth, R. K., and van den Bosch, F. C. The substructure hierarchy in dark matter haloes. , 404:502–517, May 2010. doi: 10.1111/j.1365-2966.2010.16311.x. 31

Gnedin, O. Y. and Ostriker, J. P. Limits on Collisional Dark Matter from Elliptical Galaxies in Clusters. , 561:61–68, November 2001. doi: 10.1086/323211. 109

Gnedin, O. Y., Kravtsov, A. V., Klypin, A. A., and Nagai, D. Response of Dark Matter Halos to Condensation of Baryons: Cosmological Simulations and Improved Adiabatic Contraction Model. , 616:16–26, November 2004. doi: 10.1086/424914. 109

Governato, F., Brook, C., Mayer, L., Brooks, A., Rhee, G., Wadsley, J., Jonsson, P., Willman, B., Stinson, G., Quinn, T., and Madau, P. Bulgeless dwarf galaxies and dark matter cores from supernova-driven outflows. , 463:203–206, January 2010. doi: 10.1038/nature08640. 109

Governato, F., Zolotov, A., Pontzen, A., Christensen, C., Oh, S. H., Brooks, A. M., Quinn, T., Shen, S., and Wadsley, J. Cuspy no more: how outflows affect the central dark matter and baryon distribution in Λ cold dark matter galaxies. , 422: 1231–1240, May 2012. doi: 10.1111/j.1365-2966.2012.20696.x. 109

Guo, Q., White, S., Li, C., and Boylan-Kolchin, M. How do galaxies populate dark matter haloes? , 404:1111–1120, May 2010. doi: 10.1111/j.1365-2966.2010.16341.x. 106

Guo, Q., White, S., Boylan-Kolchin, M., De Lucia, G., Kauffmann, G., Lemson, G., Li, C., Springel, V., and Weinmann, S. From dwarf spheroidals to cD galaxies: simulating the galaxy population in a ΛCDM cosmology. , 413:101–131, May 2011. doi: 10.1111/j.1365-2966.2010.18114.x. 23, 109

Guo, Q., White, S., Boylan-Kolchin, M., De Lucia, G., Kauffmann, G., Lemson, G., Li, C., Springel, V., and Weinmann, S. Erratum: From dwarf spheroidals to cD galaxies: simulating the galaxy population in a ΛCDM cosmology. , 435:897–897, October 2013. doi: 10.1093/mnras/stt1331. 106

Hahn, O., Porciani, C., Carollo, C. M., and Dekel, A. Properties of dark matter haloes in clusters, filaments, sheets and voids. , 375:489–499, February 2007. doi: 10.1111/j.1365-2966.2006.11318.x. 24

Han, J., Jing, Y., Wang, H., and Wang, W. Resolving Subhalos' Lives with the Hierarchical Bound-Tracing Algorithm. *Galaxy Formation*, page 175P, July 2011. 31, 34, 39, 42, 48

Han, J., Jing, Y. P., Wang, H., and Wang, W. Resolving subhaloes' lives with the Hierarchical Bound-Tracing algorithm. , 427:2437–2449, December 2012. doi: 10.1111/j.1365-2966.2012.22111.x. 31

Helmi, A. The stellar halo of the Galaxy. , 15:145–188, June 2008. doi: 10.1007/s00159-008-0009-6. 24

Helmi, A., Cooper, A. P., White, S. D. M., Cole, S., Frenk, C. S., and Navarro, J. F. Substructure in the Stellar Halos of the Aquarius Simulations. , 733:L7, May 2011. doi: 10.1088/2041-8205/733/1/L7. 25

Henriques, B. M. B., Thomas, P. A., Oliver, S., and Roseboom, I. Monte Carlo Markov Chain parameter estimation in semi-analytic models of galaxy formation. , 396:535–547, June 2009. doi: 10.1111/j.1365-2966.2009.14730.x. 12, 105

Hockney, R. W. and Eastwood, J. W. *Computer Simulation Using Particles*. 1981. 19

Hoffman, Y., Metuki, O., Yepes, G., Gottlöber, S., Forero-Romero, J. E., Libeskind, N. I., and Knebe, A. A kinematic classification of the cosmic web. , 425:2049–2057, September 2012. doi: 10.1111/j.1365-2966.2012.21553.x. 24

Hoyle, B., Jimenez, R., and Verde, L. Does stellar mass assembly history vary with environment? , 415:2818–2826, August 2011. doi: 10.1111/j.1365-2966.2011.18899.x. 26

Huchra, J. P. and Geller, M. J. Groups of galaxies. I - Nearby groups. , 257:423–437, June 1982. doi: 10.1086/160000. 27

Jenkins, A., Frenk, C. S., White, S. D. M., Colberg, J. M., Cole, S., Evrard, A. E., Couchman, H. M. P., and Yoshida, N. The mass function of dark matter haloes. , 321:372–384, February 2001. doi: 10.1046/j.1365-8711.2001.04029.x. 12, 27

Jernigan, J. G. and Porter, D. H. A tree code with logarithmic reduction of force terms, hierarchical regularization of all variables, and explicit accuracy controls. , 71:871–893, December 1989. doi: 10.1086/191400. 19

Jing, Y. P. and Suto, Y. Triaxial Modeling of Halo Density Profiles with High-Resolution N-Body Simulations. , 574:538–553, August 2002. doi: 10.1086/341065. 25

Jing, Y. P., Mo, H. J., and Börner, G. Spatial Correlation Function and Pairwise Velocity Dispersion of Galaxies: Cold Dark Matter Models versus the Las Campanas Survey. , 494:1–12, February 1998. doi: 10.1086/305209. 106

Kaiser, N. and Squires, G. Mapping the dark matter with weak gravitational lensing. , 404:441–450, February 1993. doi: 10.1086/172297. 12, 25

Kaplinghat, M., Keeley, R. E., Linden, T., and Yu, H.-B. Tying Dark Matter to Baryons with Self-Interactions. *Physical Review Letters*, 113(2):021302, July 2014. doi: 10.1103/PhysRevLett.113.021302. 108

Klypin, A., Kravtsov, A. V., Valenzuela, O., and Prada, F. Where Are the Missing Galactic Satellites? , 522:82–92, September 1999. doi: 10.1086/307643. 110

Klypin, A., Yepes, G., Gottlober, S., Prada, F., and Hess, S. MultiDark simulations: the story of dark matter halo concentrations and density profiles. *ArXiv e-prints*, November 2014. 12

Klypin, A. A. and Shandarin, S. F. Three-dimensional numerical model of the formation of large-scale structure in the Universe. , 204:891–907, September 1983. 18

Knebe, A. Amiga halo finder documentation @ONLINE, April 2015. URL `http://popia.ft.uam.es/AHF/files/AHF.pdf`. 35

Knebe, A., Knollmann, S. R., Muldrew, S. I., Pearce, F. R., Aragon-Calvo, M. A., Ascasibar, Y., Behroozi, P. S., Ceverino, D., Colombi, S., Diemand, J., Dolag, K., Falck, B. L., Fasel, P., Gardner, J., Gottlöber, S., Hsu, C.-H., Iannuzzi, F., Klypin, A., Lukić, Z., Maciejewski, M., McBride, C., Neyrinck, M. C., Planelles, S., Potter, D., Quilis, V., Rasera, Y., Read, J. I., Ricker, P. M., Roy, F., Springel, V., Stadel, J., Stinson, G., Sutter, P. M., Turchaninov, V., Tweed, D., Yepes, G., and Zemp, M. Haloes gone MAD: The Halo-Finder Comparison Project. , 415:2293–2318, August 2011. doi: 10.1111/j.1365-2966.2011.18858.x. 12, 21

Knebe, A., Libeskind, N. I., Pearce, F., Behroozi, P., Casado, J., Dolag, K., Dominguez-Tenreiro, R., Elahi, P., Lux, H., Muldrew, S. I., and Onions, J. Galaxies going MAD: the Galaxy-Finder Comparison Project. , 428:2039–2052, January 2013. doi: 10.1093/mnras/sts173. 12, 32

Knebe, A., Pearce, F. R., Lux, H., Ascasibar, Y., Behroozi, P., Casado, J., Moran, C. C., Diemand, J., Dolag, K., Dominguez-Tenreiro, R., Elahi, P., Falck, B., Gottlöber, S., Han, J., Klypin, A., Lukić, Z., Maciejewski, M., McBride, C. K., Merchán, M. E., Muldrew, S. I., Neyrinck, M., Onions, J., Planelles, S., Potter, D., Quilis, V., Rasera, Y., Ricker, P. M., Roy, F., Ruiz, A. N., Sgró, M. A., Springel, V., Stadel, J., Sutter, P. M., Tweed, D., and Zemp, M. Structure finding in cosmological simulations: the state of affairs. *mnras*, 435:1618–1658, October 2013. doi: 10.1093/mnras/stt1403. 12, 21, 40

Knebe, A., Pearce, F. R., Thomas, P. A., Benson, A., Blaizot, J., Bower, R., Carretero, J., Castander, F. J., Cattaneo, A., Cora, S. A., Croton, D. J., Cui, W., Cunnama, D., De Lucia, G., Devriendt, J. E., Elahi, P. J., Font, A., Fontanot, F., Garcia-Bellido, J., Gargiulo, I. D., Gonzalez-Perez, V., Helly, J., Henriques, B., Hirschmann, M., Lee, J., Mamon, G. A., Monaco, P., Onions, J., Padilla, N. D., Power, C., Pujol, A., Skibba, R. A., Somerville, R. S., Srisawat, C., Vega-Martínez, C. A., and Yi, S. K. nIFTy cosmology: comparison of galaxy formation models. , 451:4029–4059, August 2015. doi: 10.1093/mnras/stv1149. 29

Knollmann, S. R. and Knebe, A. AHF: Amiga's Halo Finder. February 2011. 30, 31, 34, 35, 42, 48

Kochanek, C. S. and White, M. A Quantitative Study of Interacting Dark Matter in Halos. , 543:514–520, November 2000. doi: 10.1086/317149. 108

Kravtsov, A. V., Berlind, A. A., Wechsler, R. H., Klypin, A. A., Gottlöber, S., Allgood, B., and Primack, J. R. The Dark Side of the Halo Occupation Distribution. , 609:35–49, July 2004. doi: 10.1086/420959. 110

Kuhlen, M., Weiner, N., Diemand, J., Madau, P., Moore, B., Potter, D., Stadel, J., and Zemp, M. Dark matter direct detection with non-Maxwellian velocity structure. , 2:030, February 2010. doi: 10.1088/1475-7516/2010/02/030. 24

Kuhlen, M., Lisanti, M., and Spergel, D. N. Direct detection of dark matter debris flows. , 86(6):063505, September 2012. doi: 10.1103/PhysRevD.86.063505. 24

Lacey, C. and Cole, S. Merger Rates in Hierarchical Models of Galaxy Formation - Part Two - Comparison with N-Body Simulations. , 271:676, December 1994. doi: 10.1093/mnras/271.3.676. 24, 27

Larson, R. B. Effects of supernovae on the early evolution of galaxies. , 169:229–246, November 1974. 108

LH́uillier, B., Park, C., and Kim, J. Effects of the initial conditions on cosmological N-body simulations. , 30:79–88, July 2014. doi: 10.1016/j.newast.2014.01.007. 11

Li, B., Zhao, G.-B., Teyssier, R., and Koyama, K. ECOSMOG: an Efficient COde for Simulating MOdified Gravity. , 1:051, January 2012. doi: 10.1088/1475-7516/2012/01/051. 26

Libeskind, N. I., Hoffman, Y., Knebe, A., Steinmetz, M., Gottlöber, S., Metuki, O., and Yepes, G. The cosmic web and the orientation of angular momenta. , 421:L137–L141, March 2012. doi: 10.1111/j.1745-3933.2012.01222.x. 12, 24

Limousin, M., Ebeling, H., Richard, J., Swinbank, A. M., Smith, G. P., Jauzac, M., Rodionov, S., Ma, C.-J., Smail, I., Edge, A. C., Jullo, E., and Kneib, J.-P. Strong lensing by a node of the cosmic web. The core of MACS J0717.5+3745 at z = 0.55. , 544:A71, August 2012. doi: 10.1051/0004-6361/201117921. 25

Loeb, A. and Weiner, N. Cores in Dwarf Galaxies from Dark Matter with a Yukawa Potential. *Physical Review Letters*, 106(17):171302, April 2011. doi: 10.1103/PhysRevLett.106.171302. 108, 109

Lovell, M. R., Eke, V., Frenk, C. S., Gao, L., Jenkins, A., Theuns, T., Wang, J., White, S. D. M., Boyarsky, A., and Ruchayskiy, O. The haloes of bright satellite galaxies in a warm dark matter universe. , 420:2318–2324, March 2012. doi: 10.1111/j.1365-2966.2011.20200.x. 108

LoVerde, M., Ferraro, S., and Smith, K. M. Testing Inflation with Dark Matter Halos. *ArXiv e-prints*, October 2011. 26

Lukić, Z., Reed, D., Habib, S., and Heitmann, K. The Structure of Halos: Implications for Group and Cluster Cosmology. , 692:217–228, February 2009. doi: 10.1088/0004-637X/692/1/217. 24

Macciò, A. V., Murante, G., and Bonometto, S. P. Mass of Clusters in Simulations. , 588:35–49, May 2003. doi: 10.1086/373944. 32

Macciò, A. V., Paduroiu, S., Anderhalden, D., Schneider, A., and Moore, B. Cores in warm dark matter haloes: a Catch 22 problem. , 424:1105–1112, August 2012a. doi: 10.1111/j.1365-2966.2012.21284.x. 108

Macciò, A. V., Stinson, G., Brook, C. B., Wadsley, J., Couchman, H. M. P., Shen, S., Gibson, B. K., and Quinn, T. Halo Expansion in Cosmological Hydro Simulations: Toward a Baryonic Solution of the Cusp/Core Problem in Massive Spirals. , 744: L9, January 2012b. doi: 10.1088/2041-8205/744/1/L9. 108, 109

Maciejewski, M., Colombi, S., Springel, V., Alard, C., and Bouchet, F. R. Phase-space structures - II. Hierarchical Structure Finder. *mnras*, 396:1329–1348, July 2009. doi: 10.1111/j.1365-2966.2009.14825.x. 30, 34, 37, 42, 48

Maciejewski, M., Vogelsberger, M., White, S. D. M., and Springel, V. Bound and unbound substructures in Galaxy-scale dark matter haloes. , 415:2475–2484, August 2011. doi: 10.1111/j.1365-2966.2011.18871.x. 26

Madau, P., Shen, S., and Governato, F. Dark Matter Heating and Early Core Formation in Dwarf Galaxies. , 789:L17, July 2014. doi: 10.1088/2041-8205/789/1/L17. 109

Magorrian, J., Tremaine, S., Richstone, D., Bender, R., Bower, G., Dressler, A., Faber, S. M., Gebhardt, K., Green, R., Grillmair, C., Kormendy, J., and Lauer, T. The Demography of Massive Dark Objects in Galaxy Centers. , 115:2285–2305, June 1998. doi: 10.1086/300353. 109

Mario Agustín Sgró, M. E. M., Andrés Nicolás Ruiz. Mendieta: A subhalo finder,j instituto de astronomía teórica y experimental@ONLINE, April 2015. URL `http://baldboybakery.com/courses/phys2300/Tutorials/Tutorial4.1.html`. 30, 34, 37, 42, 48

Mashchenko, S., Couchman, H. M. P., and Wadsley, J. The removal of cusps from galaxy centres by stellar feedback in the early Universe. , 442:539–542, August 2006. doi: 10.1038/nature04944. 109

McConnell, N. J., Chen, S.-F. S., Ma, C.-P., Greene, J. E., Lauer, T. R., and Gebhardt, K. The Effect of Spatial Gradients in Stellar Mass-to-light Ratio on Black Hole Mass Measurements. , 768:L21, May 2013. doi: 10.1088/2041-8205/768/1/L21. 109

McNamara, B. R. and Nulsen, P. E. J. Heating Hot Atmospheres with Active Galactic Nuclei. , 45:117–175, September 2007. doi: 10.1146/annurev.astro.45.051806.110625. 109

Mellier, Y. Probing the Universe with Weak Lensing. , 37:127–189, 1999. doi: 10.1146/annurev.astro.37.1.127. 25

Miralda-Escudé, J. A Test of the Collisional Dark Matter Hypothesis from Cluster Lensing. , 564:60–64, January 2002. doi: 10.1086/324138. 108

Mo, H., van den Bosch, F. C., and White, S. *Galaxy Formation and Evolution*. May 2010. 13, 14

Monaco, P., Fontanot, F., and Taffoni, G. The MORGANA model for the rise of galaxies and active nuclei. , 375:1189–1219, March 2007. doi: 10.1111/j.1365-2966.2006.11253.x. 12, 105

Moore, B. Evidence against dissipation-less dark matter from observations of galaxy haloes. , 370:629–631, August 1994. doi: 10.1038/370629a0. 108

Moore, B., Quinn, T., Governato, F., Stadel, J., and Lake, G. Cold collapse and the core catastrophe. , 310:1147–1152, December 1999. doi: 10.1046/j.1365-8711.1999.03039.x. 110

More, S., Kravtsov, A. V., Dalal, N., and Gottlöber, S. The Overdensity and Masses of the Friends-of-friends Halos and Universality of Halo Mass Function. , 195:4, July 2011. doi: 10.1088/0067-0049/195/1/4. 24, 27

Munshi, D., Valageas, P., van Waerbeke, L., and Heavens, A. Cosmology with weak lensing surveys. , 462:67–121, June 2008. doi: 10.1016/j.physrep.2008.02.003. 25

Navarro, J. F., Eke, V. R., and Frenk, C. S. The cores of dwarf galaxy haloes. , 283: L72–L78, December 1996. doi: 10.1093/mnras/283.3.72L. 109

Navarro, J. F., Frenk, C. S., and White, S. D. M. A Universal Density Profile from Hierarchical Clustering. , 490:493–508, December 1997. 108

Neyrinck, M. C., Gnedin, N. Y., and Hamilton, A. J. S. VOBOZ: an almost-parameter-free halo-finding algorithm. *mnras*, 356:1222–1232, February 2005. doi: 10.1111/j.1365-2966.2004.08505.x. 34, 39, 42, 48

Oñorbe, J., Boylan-Kolchin, M., Bullock, J. S., Hopkins, P. F., Kereš, D., Faucher-Giguère, C.-A., Quataert, E., and Murray, N. Forged in FIRE: cusps, cores and baryons in low-mass dwarf galaxies. , 454:2092–2106, December 2015. doi: 10.1093/mnras/stv2072. 109

Oguri, M., Takada, M., Umetsu, K., and Broadhurst, T. Can the Steep Mass Profile of A1689 Be Explained by a Triaxial Dark Halo? , 632:841–846, October 2005. doi: 10.1086/452629. 25

Oh, S.-H., Brook, C., Governato, F., Brinks, E., Mayer, L., de Blok, W. J. G., Brooks, A., and Walter, F. The Central Slope of Dark Matter Cores in Dwarf Galaxies: Simulations versus THINGS. , 142:24, July 2011. doi: 10.1088/0004-6256/142/1/24. 108

Onions, J., Knebe, A., Pearce, F. R., Muldrew, S. I., Lux, H., Knollmann, S. R., Ascasibar, Y., Behroozi, P., Elahi, P., Han, J., Maciejewski, M., Merchán, M. E., Neyrinck, M., Ruiz, A. N., Sgró, M. A., Springel, V., and Tweed, D. Subhaloes going Notts: the subhalo-finder comparison project. *mnras*, 423:1200–1214, June 2012. doi: 10.1111/j.1365-2966.2012.20947.x. 12, 13, 20, 21

Onions, J., Ascasibar, Y., Behroozi, P., Casado, J., Elahi, P., Han, J., Knebe, A., Lux, H., Merchán, M. E., Muldrew, S. I., Neyrinck, M., Old, L., Pearce, F. R., Potter, D., Ruiz, A. N., Sgró, M. A., Tweed, D., and Yue, T. Subhaloes gone

Notts: spin across subhaloes and finders. , 429:2739–2747, March 2013. doi: 10.1093/mnras/sts549. 12, 21, 46, 60, 63, 76

O'Shea, B. W., Bryan, G., Bordner, J., Norman, M. L., Abel, T., Harkness, R., and Kritsuk, A. Introducing Enzo, an AMR Cosmology Application. *ArXiv Astrophysics e-prints*, March 2004. 103

Ostriker, J. P., Peebles, P. J. E., and Yahil, A. The size and mass of galaxies, and the mass of the universe. , 193:L1–L4, October 1974. doi: 10.1086/181617. 14

Papastergis, E. and Shankar, F. An assessment of the "too big to fail" problem for field dwarf galaxies in view of baryonic feedback effects. *ArXiv e-prints*, November 2015. 110

Peñarrubia, J., Pontzen, A., Walker, M. G., and Koposov, S. E. The Coupling between the Core/Cusp and Missing Satellite Problems. , 759:L42, November 2012. doi: 10.1088/2041-8205/759/2/L42. 109

Pearce, F. R., Jenkins, A., Frenk, C. S., White, S. D. M., Thomas, P. A., Couchman, H. M. P., Peacock, J. A., and Efstathiou, G. Simulations of galaxy formation in a cosmological volume. , 326:649–666, September 2001. doi: 10.1046/j.1365-8711.2001.04616.x. 104

Peebles, P. J. E. Masses of galaxies and clusters of galaxies. In Balian, R., Audouze, J., and Schramm, D. N., editors, *Physical Cosmology*, page 213, 1980. 27

Penzias, A. A. and Wilson, R. W. A Measurement of Excess Antenna Temperature at 4080 Mc/s. , 142:419–421, July 1965. doi: 10.1086/148307. 15

Perlmutter, S., Turner, M. S., and White, M. Constraining Dark Energy with Type Ia Supernovae and Large-Scale Structure. *Physical Review Letters*, 83:670–673, July 1999. doi: 10.1103/PhysRevLett.83.670. 14

Peter, A. H. G., Rocha, M., Bullock, J. S., and Kaplinghat, M. Cosmological simulations with self-interacting dark matter - II. Halo shapes versus observations. , 430:105–120, March 2013. doi: 10.1093/mnras/sts535. 108

Pontzen, A. and Governato, F. How supernova feedback turns dark matter cusps into cores. , 421:3464–3471, April 2012. doi: 10.1111/j.1365-2966.2012.20571.x. 109

Pontzen, A. and Governato, F. Cold dark matter heats up. , 506:171–178, February 2014. doi: 10.1038/nature12953. 109

Porter, D. H. and Jernigan, J. G. A Study of Hierarchical Clustering of Galaxies in an Expanding Universe. In *Bulletin of the American Astronomical Society*, volume 18 of *Bulletin of the American Astronomical Society*, page 906, September 1986. 19

Prada, F., Klypin, A. A., Simonneau, E., Betancort-Rijo, J., Patiri, S., Gottlöber, S., and Sanchez-Conde, M. A. How Far Do They Go? The Outer Structure of Galactic Dark Matter Halos. , 645:1001–1011, July 2006. doi: 10.1086/504456. 32

Press, W. H. and Davis, M. How to identify and weigh virialized clusters of galaxies in a complete redshift catalog. , 259:449–473, August 1982. doi: 10.1086/160183. 27

Press, W. H. and Schechter, P. Formation of Galaxies and Clusters of Galaxies by Self-Similar Gravitational Condensation. , 187:425–438, February 1974. doi: 10.1086/152650. 27

Rashkov, V., Madau, P., Kuhlen, M., and Diemand, J. On the Assembly of the Milky Way Dwarf Satellites and Their Common Mass Scale. , 745:142, February 2012. doi: 10.1088/0004-637X/745/2/142. 25

Read, J. I. and Gilmore, G. Mass loss from dwarf spheroidal galaxies: the origins of shallow dark matter cores and exponential surface brightness profiles. , 356: 107–124, January 2005. doi: 10.1111/j.1365-2966.2004.08424.x. 109

Reed, D., Governato, F., Verde, L., Gardner, J., Quinn, T., Stadel, J., Merritt, D., and Lake, G. Evolution of Dark Matter Halo Density Profiles and Substructure from ΛCDM Simulations. In Mellier, Y. and Meylan, G., editors, *Gravitational*

Lensing Impact on Cosmology, volume 225 of *IAU Symposium*, pages 231–236, June 2005. doi: 10.1017/S1743921305002024. 12

Reed, D. S., Bower, R., Frenk, C. S., Jenkins, A., and Theuns, T. The halo mass function from the dark ages through the present day. , 374:2–15, January 2007. doi: 10.1111/j.1365-2966.2006.11204.x. 12

Reed, D. S., Smith, R. E., Potter, D., Schneider, A., Stadel, J., and Moore, B. Towards an accurate mass function for precision cosmology. , 431:1866–1882, May 2013. doi: 10.1093/mnras/stt301. 11

Refregier, A. Weak Gravitational Lensing by Large-Scale Structure. , 41:645–668, 2003. doi: 10.1146/annurev.astro.41.111302.102207. 25

Riess, A. G. An Accelerating Universe and Other Cosmological Implications from SNe IA. In *American Astronomical Society Meeting Abstracts #192*, volume 30 of *Bulletin of the American Astronomical Society*, page 843, May 1998. 14

Rocha, M., Peter, A., Bullock, J., Kaplinghat, M., Garrison-Kimmel, S., Onorbe, J., and Moustakas, L. A. Cosmological simulations with self-interacting dark matter. In *Probes of Dark Matter on Galaxy Scales*, volume 1, July 2013. 108

Romano-Díaz, E., Shlosman, I., Hoffman, Y., and Heller, C. Erasing Dark Matter Cusps in Cosmological Galactic Halos with Baryons. , 685:L105, October 2008. doi: 10.1086/592687. 109

Rubin, V. C. and Ford, W. K., Jr. Rotation of the Andromeda Nebula from a Spectroscopic Survey of Emission Regions. , 159:379, February 1970. doi: 10.1086/150317. 14

Scannapieco, C. Simulations of galaxy formation and evolution. *Astronomische Nachrichten*, 333:470, June 2012. doi: 10.1002/asna.201211681. 11

Scannapieco, C. and Athanassoula, E. Bars in hydrodynamical cosmological simulations. *mnras*, 425:L10–L14, September 2012. doi: 10.1111/j.1745-3933.2012.01291.x. 12, 24

Schaller, M., Frenk, C. S., Bower, R. G., Theuns, T., Jenkins, A., Schaye, J., Crain, R. A., Furlong, M., Dalla Vecchia, C., and McCarthy, I. G. Baryon effects on the internal structure of ΛCDM haloes in the EAGLE simulations. , 451:1247–1267, August 2015. doi: 10.1093/mnras/stv1067. 11

Schaye, J., Crain, R. A., Bower, R. G., Furlong, M., Schaller, M., Theuns, T., Dalla Vecchia, C., Frenk, C. S., McCarthy, I. G., Helly, J. C., Jenkins, A., Rosas-Guevara, Y. M., White, S. D. M., Baes, M., Booth, C. M., Camps, P., Navarro, J. F., Qu, Y., Rahmati, A., Sawala, T., Thomas, P. A., and Trayford, J. The EAGLE project: Simulating the evolution and assembly of galaxies and their environments. *ArXiv e-prints*, July 2014. 11, 16, 104

Schmidt, B. Investigating Type Ia Supernovae and an Accelerating Universe. HST Proposal, July 1999. 14

Schmidt, F. Cosmological simulations of normal-branch braneworld gravity. , 80 (12):123003, December 2009. doi: 10.1103/PhysRevD.80.123003. 26

Schneider, P. Part 3: Weak gravitational lensing. In Meylan, G., Jetzer, P., North, P., Schneider, P., Kochanek, C. S., and Wambsganss, J., editors, *Saas-Fee Advanced Course 33: Gravitational Lensing: Strong, Weak and Micro*, pages 269–451, 2006. 12, 25

Sereno, M. and Zitrin, A. Triaxial strong-lensing analysis of the z 0.5 MACS clusters: the mass-concentration relation. , 419:3280–3291, February 2012. doi: 10.1111/j.1365-2966.2011.19968.x. 25

Sharma, S. and Steinmetz, M. Multidimensional density estimation and phase-space structure of dark matter haloes. , 373:1293–1307, December 2006. doi: 10.1111/j.1365-2966.2006.11043.x. 12, 24

Shen, J., Abel, T., Mo, H. J., and Sheth, R. K. An Excursion Set Model of the Cosmic Web: The Abundance of Sheets, Filaments, and Halos. , 645:783–791, July 2006. doi: 10.1086/504513. 15

Sheth, R. K., Mo, H. J., and Tormen, G. Ellipsoidal collapse and an improved model for the number and spatial distribution of dark matter haloes. \mnras, 323:1–12, May 2001. doi: 10.1046/j.1365-8711.2001.04006.x. 48

Skibba, R. A. and Sheth, R. K. A halo model of galaxy colours and clustering in the Sloan Digital Sky Survey. , 392:1080–1091, January 2009. doi: 10.1111/j.1365-2966.2008.14007.x. 106

Somerville, R. S., Hopkins, P. F., Cox, T. J., Robertson, B. E., and Hernquist, L. A semi-analytic model for the co-evolution of galaxies, black holes and active galactic nuclei. , 391:481–506, December 2008. doi: 10.1111/j.1365-2966.2008.13805.x. 12, 105

Spekkens, K., Giovanelli, R., and Haynes, M. P. The Cusp/Core Problem in Galactic Halos: Long-Slit Spectra for a Large Dwarf Galaxy Sample. , 129:2119–2137, May 2005. doi: 10.1086/429592. 108

Springel, V. Smoothed Particle Hydrodynamics in Astrophysics. , 48:391–430, September 2010. doi: 10.1146/annurev-astro-081309-130914. 11, 103, 104

Springel, V. Larger, faster, better: Current trends in cosmological simulations. *Astronomische Nachrichten*, 333:515–522, June 2012. doi: 10.1002/asna.201211701. 16

Springel, V., White, M., and Hernquist, L. Erratum: Hydrodynamic Simulations of the Sunyaev-Zeldovich Effect(s). \apj, 562:1086, December 2001a. doi: 10.1086/323699. 16, 104

Springel, V., White, S. D. M., Tormen, G., and Kauffmann, G. Populating a cluster of galaxies - I. Results at [formmu2]z=0. \mnras, 328:726–750, December 2001b. doi: 10.1046/j.1365-8711.2001.04912.x. 30, 31, 34, 37, 42, 48

Springel, V., White, S. D. M., Jenkins, A., Frenk, C. S., Yoshida, N., Gao, L., Navarro, J., Thacker, R., Croton, D., Helly, J., Peacock, J. A., Cole, S., Thomas, P., Couchman, H., Evrard, A., Colberg, J., and Pearce, F. Simulations of the formation, evolution and clustering of galaxies and quasars. , 435:629–636, June 2005. doi: 10.1038/nature03597. 11, 15, 19, 104

Springel, V., Wang, J., Vogelsberger, M., Ludlow, A., Jenkins, A., Helmi, A., Navarro, J. F., Frenk, C. S., and White, S. D. M. The Aquarius Project: the subhaloes of galactic haloes. , 391:1685–1711, December 2008. doi: 10.1111/j.1365-2966.2008.14066.x. 20, 110

Stoehr, F., White, S. D. M., Springel, V., Tormen, G., and Yoshida, N. Dark matter annihilation in the halo of the Milky Way. , 345:1313–1322, November 2003. doi: 10.1046/j.1365-2966.2003.07052.x. 25

Swaters, R. A., Madore, B. F., van den Bosch, F. C., and Balcells, M. The Central Mass Distribution in Dwarf and Low Surface Brightness Galaxies. , 583:732–751, February 2003. doi: 10.1086/345426. 108

Tasitsiomi, A., Kravtsov, A. V., Wechsler, R. H., and Primack, J. R. Modeling Galaxy-Mass Correlations in Dissipationless Simulations. , 614:533–546, October 2004. doi: 10.1086/423784. 110

Teyssier, R. Cosmological hydrodynamics with adaptive mesh refinement. A new high resolution code called RAMSES. , 385:337–364, April 2002. doi: 10.1051/0004-6361:20011817. 103

Teyssier, R., Pontzen, A., Dubois, Y., and Read, J. I. Cusp-core transformations in dwarf galaxies: observational predictions. , 429:3068–3078, March 2013. doi: 10.1093/mnras/sts563. 109

Tinker, J., Kravtsov, A. V., Klypin, A., Abazajian, K., Warren, M., Yepes, G., Gottlöber, S., and Holz, D. E. Toward a Halo Mass Function for Precision Cosmology: The Limits of Universality. , 688:709-728, December 2008. doi: 10.1086/591439. 24, 27, 28

Tonini, C. Baryons-DM angular momentum transfer: erasing the cusp. In *Bernard's Cosmic Stories: From Primordial Fluctuations to the Birth of Stars and Galaxies*, page 64.1, 2006. 109

Tormen, G. Hydrodynamic Simulations of Galaxy Formation. In Ansari, R., Giraud-Heraud, Y., and Tran Thanh Van, J., editors, *Dark Matter in Cosmology Quantam Measurements Experimental Gravitation*, page 207, 1996. 16, 103

Tormen, G., Moscardini, L., and Yoshida, N. Properties of cluster satellites in hydrodynamical simulations. , 350:1397–1408, June 2004. doi: 10.1111/j.1365-2966.2004.07736.x. 31

Tremaine, S., Gebhardt, K., Bender, R., Bower, G., Dressler, A., Faber, S. M., Filippenko, A. V., Green, R., Grillmair, C., Ho, L. C., Kormendy, J., Lauer, T. R., Magorrian, J., Pinkney, J., and Richstone, D. The Slope of the Black Hole Mass versus Velocity Dispersion Correlation. , 574:740–753, August 2002. doi: 10.1086/341002. 109

Vale, A. and Ostriker, J. P. Linking halo mass to galaxy luminosity. , 353:189–200, September 2004. doi: 10.1111/j.1365-2966.2004.08059.x. 106

Vogelsberger, M., Zavala, J., and Loeb, A. Subhaloes in self-interacting galactic dark matter haloes. , 423:3740–3752, July 2012. doi: 10.1111/j.1365-2966.2012.21182.x. 109

Vogelsberger, M., Genel, S., Springel, V., Torrey, P., Sijacki, D., Xu, D., Snyder, G., Nelson, D., and Hernquist, L. Introducing the Illustris Project: simulating the coevolution of dark and visible matter in the Universe. *mnras*, 444:1518–1547, October 2014. doi: 10.1093/mnras/stu1536. 16, 104

Wadsley, J. W., Stadel, J., and Quinn, T. Gasoline: a flexible, parallel implementation of TreeSPH. , 9:137–158, February 2004. doi: 10.1016/j.newast.2003.08.004. 104

Warnick, K., Knebe, A., and Power, C. The tidal streams of disrupting subhaloes in cosmological dark matter haloes. , 385:1859–1883, April 2008. doi: 10.1111/j.1365-2966.2008.12992.x. 25

Watson, W. A., Iliev, I. T., D'Aloisio, A., Knebe, A., Shapiro, P. R., and Yepes, G. The halo mass function through the cosmic ages. , 433:1230–1245, August 2013. doi: 10.1093/mnras/stt791. 24

White, S. D. M. and Frenk, C. S. Galaxy formation through hierarchical clustering. , 379:52–79, September 1991. doi: 10.1086/170483. 108

White, S. D. M. and Rees, M. J. Core condensation in heavy halos - A two-stage theory for galaxy formation and clustering. , 183:341–358, May 1978. 15, 23, 108

Wilson, G., Cole, S., and Frenk, C. S. Constraining {OMEGA}_0_ using weak gravitational lensing by clusters. , 282:501, September 1996. doi: 10.1093/mnras/282.2.501. 25

Wu, H.-Y., Zentner, A. R., and Wechsler, R. H. The Impact of Theoretical Uncertainties in the Halo Mass Function and Halo Bias on Precision Cosmology. , 713: 856–864, April 2010. doi: 10.1088/0004-637X/713/2/856. 24

Xu, G. A New Parallel N-Body Gravity Solver: TPM. , 98:355, May 1995. doi: 10.1086/192166. 19

Yoshida, N., Springel, V., White, S. D. M., and Tormen, G. Weakly Self-interacting Dark Matter and the Structure of Dark Halos. , 544:L87–L90, December 2000. doi: 10.1086/317306. 108

Zehavi, I., Zheng, Z., Weinberg, D. H., Frieman, J. A., Berlind, A. A., Blanton, M. R., Scoccimarro, R., Sheth, R. K., Strauss, M. A., Kayo, I., Suto, Y., Fukugita, M., Nakamura, O., Bahcall, N. A., Brinkmann, J., Gunn, J. E., Hennessy, G. S., Ivezić, Ž., Knapp, G. R., Loveday, J., Meiksin, A., Schlegel, D. J., Schneider, D. P., Szapudi, I., Tegmark, M., Vogeley, M. S., York, D. G., and SDSS Collaboration. The Luminosity and Color Dependence of the Galaxy Correlation Function. , 630: 1–27, September 2005. doi: 10.1086/431891. 106

Zemp, M., Diemand, J., Kuhlen, M., Madau, P., Moore, B., Potter, D., Stadel, J., and Widrow, L. The graininess of dark matter haloes. , 394:641–659, April 2009. doi: 10.1111/j.1365-2966.2008.14361.x. 24

Zhao, G.-B., Li, B., and Koyama, K. N-body simulations for f(R) gravity using a self-adaptive particle-mesh code. , 83(4):044007, February 2011. doi: 10.1103/PhysRevD.83.044007. 26

The chapter A briefly describes gas simulations. chapter C describes the outstanding issues with the model and observations. The chapter B describes the different ways of populating galaxies to haloes. Lastly, the chapter C.4 describes calculate mass using vmax instead of virial mass.

Appendix A

Gas Simulations

N-body simulations are extended to incorporate gas particles which eventually forms stars and galaxies. As gas can be treated as a fluid, one can use fluid equations on the gas particles and evolve them. This is referred to as hydrodynamical simulation or simply hydro simulation (Tormen, 1996). Hydro simulations are of two types: Grid based or grid-free. In a grid-based simulation reference frame is fixed with respect to the fluid (Eulerian) and Grid-free (or mesh-free) simulation is one where the reference frame moves with the fluid (Lagrangian).

With a grid-based (Eulerian) simulation, the volume can be imagined as a grid composed of cells, and quantities are measured at each cell of the grid. Adaptive Mesh Refinement (AMR) can be used to further break each cell into more refined cells This increases the resolution and also the speed of the code. SPH (Smooth Particle Hydrodynamics) codes with Eulerian include RAMSES (Teyssier, 2002), ENZO (O'Shea et al., 2004) and FLASH (Fryxell et al., 2000). The Arepo (Springel, 2010) code takes advantage of both the Lagrangian and the Eulerian techniques by using a moving mesh. A moving mesh instead of SPH also facilitates the treatment of shocks. Further subsections describe different methods to populate galaxies into haloes.

A grid free simulation is often implemented using an SPH code which considers fluid as a discrete set of fluid elements or discrete sample points. Each sample point has basic quantities mass, position, velocity, etc and physical field quantities e.g. mass-density, temperature, pressure, etc. SPH uses a method of interpolation, as the quantities at these sampling points are smoothed or averaged values determined using derivatives of the quantities. Any quantity such as density, temperature, etc of any sampling point is calculated using a 'kernel' function, an integration function that averages out the property using surrounding particles within a distance range of $2h$ called the 'smoothing length'. The kernel function, usually represented by symbol 'W' is either 'Gaussian', 'cubic spline' or many others. SPH codes include Gadget (Springel et al., 2005), Hydra (Couchman et al., 1995; Pearce et al., 2001) and Gasoline (Wadsley et al., 2004). For a more detailed description of SPH see the review by Springel (2010) or the code paper for Gadget (Springel et al., 2005),

Some of the major gas simulations run recently are briefly highlighted as follows. The latest simulation is the Illustris simulation, a suite of hydrodynamical simulations that produces better constrained distribution of ellipticals, spirals and black holes. Recent progress with increasing processing power, more efficient numerical algorithms and with more physical processes, small scale processes such as star formation and accretion are coupled to large scales. The Illustris output predict the statistics on both large scales such as estimating distribution of galaxies in massive galaxy clusters or the distribution of neutral hydrogen, and small scales such as star and gas content of galaxies, morphology of galaxies. With a box size of 106Mpc and 12 billion particles, the Illustris simulation is run from a very high redshift equivalent to 12 million years from Big Bang. More details can be found in Vogelsberger et al. (2014).

The EAGLE (Evolution and Assembly of Galaxies and their environments) is a simulation project executed at Durham University in 2014. It is a hydrodynamical simulation with a box size of 100Mpc and 7 billion particles (Springel et al., 2001a). This simulation is a modified Gadget 2 code run on 4000 cores, and contains around 10,000 Milky Way sized galaxies. It implements many astrophysical processes including metal-dependent cooling, star formation, metal enrichment from supernovae explosions and stars, accretion, supernova feedback, black holes, AGN feedback (Schaye et al., 2014; Furlong et al., 2014). In order to model stars and gas, baryons are introduced in the simulation. As baryonic physics is complex, models have to take into account a lot of astrophysical process such as shocks and radiative processes. The EAGLE simulation produces better constrained distribution of elliptical and spiral galaxies at all scales.

Appendix B

Populating galaxies into haloes

B.1 Semi-analytic Model

Galaxies can be populated into dark matter haloes using Semi-Analytical Models (SAM) (Croton, 2006; Somerville et al., 2008; Monaco et al., 2007; Henriques et al., 2009; Benson, 2012). SAMs require halo merger trees as input, which are constructed using the halo catalogues. Using an N-body simulation, a tree is constructed with a merger history of the haloes at $z = 0$. This tree forms the basis for the semi-analytics. The branches of the tree represent progenitors that merge to form the final haloes. The evolution of baryons within the haloes is determined by a set of equations which are connected using free parameters. The free parameters are then fine tuned to fit the model to match properties at various redshifts such as the galaxy luminosity function (Bower et al., 2010). The model generates a galaxy catalogs at various redshifts. Understanding of the parameters requires further investigation into the physical processes.

B.2 Halo Occupation Distribution

Another method of embedding galaxies into haloes is the Halo Occupation Distribution (HOD). The model reads data for a single redshift and employs a statistical method and constrains the parameters to reproduce the observed luminosity function and clustering. A statistical method determines the mass limit for haloes. Haloes above this mass limit shall be listed and galaxies are embedded into these halo.

Though HOD models (Jing et al., 1998; Benson et al., 2000; Berlind and Weinberg, 2002; Zehavi et al., 2005; Skibba and Sheth, 2009) prove to produce better observables than the semi-analytics, they suffer in that they do not provide the history of formation of galaxies or their properties as they use information from a single redshift.

B.3 Subhalo Abundance Matching

With simulations achieving higher resolution, subhalo finding is more accurate. A new method Subhalo Abundance Matching (SHAM) (Vale and Ostriker, 2004; Conroy et al., 2006; Guo et al., 2010, 2013) has emerged which uses the subhaloes in haloes to populate the galaxies into the haloes. SHAM uses a relation between the stellar mass of galaxies and subhalo peak mass in order to determine the number of subhaloes. Galaxies are then placed into subhaloes using the galaxy luminosity function. Subhalo detection is cut off at the minimum galaxy luminosity. Similar to HOD, SHAM suffers in that it does not provide the history of formation of galaxies or their properties, as it uses information from a single redshift.

Appendix C

Problems with the model

This chapter elaborates on the open issues existing between model and observations, namely the "cooling catastrophe", "cusp-core" problem and TBTF (Too Big To Fail) problem. Following that, the significance of maximum circular velocity (V_{max}) " is also discussed.

C.1 The "cooling catastrophe"

N-body simulations are excellent for simulating dark matter. However, in order to simulate galaxies and stars, gas has to be incorporated. One way of doing that is to simply add a new species of particle as gas at the start of the simulation and allow it to evolve with defined parameters like temperature and density for star formation. Gas in the dark matter haloes collapses faster than the sound speed creating shocks which heats up the gas. The gas has to cool to form stars. The cooling function is defined as below, where n is the density, k_B the Boltzmann constant, T the temperature and Λ(n, T,Z, z) is the cooling function. The cooling function is dependent on density, n, temperature, T, metallicity, Z, and redshift, z.

$$t_{cool} = \frac{3/2nk_BT}{\Lambda(n,T,Z,z)} \tag{C.1}$$

The cooling time of the cloud determines whether galaxies and stars are formed or not. If the cooling time $t_{cool} > t_H$ ($t_H = 1/H$ Hubble time) the gas takes longer than a Hubble time to cool and hence a galaxy is not formed. The cloud forms a galaxy if $t_{cool} < t_H$. If the cooling time $t_{cool} > t_{dyn}$(where $t_{dyn} = 1/\sqrt{G\rho}$ the dynamical time), the gas will be in hydrostatic equilibrium. If $t_{cool} < t_{dyn}$ the gas cloud forms stars.

With temperatures above $10^6 K$, cooling is due to free-free radiation via thermal Bremsstrahlung (free electrons escaping the atomic nuclei). Between temperatures of $T > 10^4 K$ and $T < 10^6 K$, the dominant cooling process is by recombination lines. At temperatures $T < 10^4 K$, cooling drops as gas is neutral. In simulations, gas cools quickly producing massive galaxies with many stars. This is referred to as the cooling catastrophe. This problem is solved by introducing feedback mechanisms from supernovae (Larson, 1974; White and Rees, 1978; White and Frenk, 1991) and AGN (Bower et al., 2006; Croton, 2006). The energy released from these phenomenon heats the gas which prevents the formation of stars.

C.2 "Cusp-core" problem

ΛCDM is the best cosmological model that has good agreement with observations on large scales. However, tensions still persist on small scales. On small scales, the dark matter simulation shows more objects when compared to observations. Also, the simulations indicate the halos as cuspy which is defined by the slope of the central density profile $\alpha = -1$. However, the observations show $\alpha = 0$ (Swaters et al., 2003; Gentile et al., 2004; Spekkens et al., 2005; de Blok et al., 2008; Oh et al., 2011; Flores and Primack, 1994; Moore, 1994; Navarro et al., 1997). Several alternatives such as Warm Dark Matter (WDM) and Self-Interacting Dark Matter (SIDM) have been proposed. Though WDM can wipe out the small scale structures (Dunstan et al., 2011; Lovell et al., 2012) and can produce cored profiles, it can also prevent the formation of dwarf galaxies (Macciò et al., 2012b). SIDM is self interacting and these interactions lead to cored density profile (Yoshida et al., 2000; Burkert, 2000; Kochanek and White, 2000; Davé et al., 2001; Elbert et al., 2015). SIDM incorporates baryonic effects and is in good agreement with observations (Rocha et al., 2013; Peter et al., 2013; Kaplinghat et al., 2014; Elbert et al., 2015) Simple models of SIDMs did not produce cores in galaxy clusters (Miralda-Escudé, 2002; Yoshida et al., 2000). Complex models of SIDMs with velocity dependence were successful in producing cores (Yoshida et al., 2000; Loeb and Weiner, 2011; Macciò et al., 2012b,a). However, they do not produce long lived dwarf galaxies over a considerable redshift range. Other models with a more complex 'Yukawa' potential have produced long lived dwarf galaxies with cored profiles (Gnedin and Ostriker, 2001; Loeb and Weiner, 2011). Simulation of a Milky Way sized halo produced subhaloes which could host cored dwarf galaxies (Vogelsberger et al., 2012). But the halo mass function is still not in good agreement with observations. There is also lot of evidence to show baryons affect the host halo dark matter profile (Blumenthal et al., 1986; Navarro et al., 1996; El-Zant et al., 2001; Gnedin et al., 2004; Read and Gilmore, 2005; Governato et al., 2010; Peñarrubia et al., 2012; Governato et al., 2012; Pontzen and Governato, 2012; Macciò et al., 2012b; Teyssier et al., 2013; Di Cintio et al., 2014; Pontzen and Governato, 2014). In dwarf galaxies, using n-body simulations it has been proved that removing baryonic material from initially cuspy haloes leads to cored haloes (Navarro et al., 1996; Read and Gilmore, 2005). There is an alternative suggestion that the central dark matter density could decrease due to the redistribution of dark matter because of bulk motion of the gas in the galaxies (Mashchenko et al., 2006). Other mechanisms such as dynamical effects are also thought to disrupt the density profiles of dark matter (El-Zant et al., 2001; Tonini, 2006; Romano-Díaz et al., 2008; Del Popolo, 2009). The recent zoom-in simulations incorporate feedback mechanisms such as supernova-driven wind outflows, and show that the density profile changes from cusp to core (Pontzen and Governato, 2012; Madau et al., 2014; Brooks and Zolotov, 2014; Oñorbe et al., 2015). Furthermore, feedback mechanisms such as feedback from black hole accretion can affect structure formation generally on all scales (McNamara and Nulsen, 2007). It has been observed that there is correlation between black hole mass and velocity dispersion (Ferrarese and Merritt, 2000; Tremaine et al., 2002), luminosity and stellar mass (Magorrian et al., 1998; Bennert et al., 2011; McConnell et al., 2013). This is theoretically supported by semi-analytic models (Benson et al., 2003; Bower et al., 2006; Croton, 2006; Guo et al., 2011) which are discussed in the next subsection.

C.3 TBTF problem

"Too Big To Fail"(TBTF) is an open problem that exists in CDM (Boylan-Kolchin et al., 2011). On galactic scales, there is a mismatch in the number of observed

Milky Way satellite galaxies and the expected satellite galaxies from simulations (Klypin et al., 1999; Moore et al., 1999; Bullock, 2010). The TBTF issue is strongly connected to the cusp-core problem as the central density is related to the internal velocity of the satellite galaxies as shown by many dark matter only simulations such as "Via Lactea"(Milky Way) (Diemand et al., 2007) and Aquarius (Springel et al., 2008). The subhaloes from these simulations are more dense at the core than the observed satellites in the Milky Way galaxy, or the dwarfs in the local group (Garrison-Kimmel et al., 2014; Papastergis and Shankar, 2015). The Aquarius simulation produced a minimum of 10 subhaloes with V_{max} greater than 25km/s. However, the V_{max} for observed dwarf spheroidal(dSph) satellites is less than 25km/s.

C.4 Measuring mass using V_{max}

In order to measure the mass of a halo, the initial edge or boundary of a halo is taken as the virial radius. The most common definition of virial radius uses the density-contrast of 200, which provides a spherical radius at which the average density of the halo is 200 times the critical density or background density. However, the density contrast evolves with redshift. This implies mass definitions have to be correspondingly changed for higher redshifts. A better alternative to using density contrast is the maximum circular velocity V_{max}, which is expressed as $\sqrt{GM(<r)/r}$. This is because V_{max} is reached at a distance very close to the centre of the halo where stars and gas can be used to trace the velocity of a halo. For early-type galaxies, the velocity measured is the line-of-sight velocity dispersion, and for late-type it is the rotational velocity. According to Faber-Jackson and Tully-Fisher relations, the observed velocity of a galaxy (late or early type) has a direct correlation with the luminosity. When a larger halo accretes material from a subhalo, the subhalo might lose mass in the outskirts due to tidal stripping. However V_{max} is less affected. This is because the subhalo stellar mass is determined before it was accreted using the V_{max}. As there is a good correlation with the observed internal velocity and the observed brightness of galaxy, V_{max} is considered an important parameter in mapping the galaxies luminosities to V_{max} of haloes (Kravtsov et al., 2004; Tasitsiomi et al., 2004; Conroy et al., 2006). In summary, the current model could be better

constrained with the mass estimates using V_{max} instead of density contrast.